NASA-CR-202658

ROSAT PSPC OBSERVATIONS OF CL0016+16

NASA Grant NAG5-2156

Annual Report No. 4

for the Period 15 December 1995 though 14 December 1996

Principal Investigator
Dr. John P. Hughes

November 1996

Prepared for

National Aeronautics and Space Administration
Goddard Space Flight Center
Greenbelt, Maryland 20771

Smithsonian Institution
Astrophysical Observatory
Cambridge, Massachusetts 02138

Director: Dr. Irwin I. Shapiro

The Smithsonian Astrophysical Observatory
is a member of the
Harvard-Smithsonian Center for Astrophysics

The NASA Technical Officer for this contract Dr. Robert Petre, Code 666, Laboratory for High Energy Astrophysics, Space Science Directorate, Goddard Space Flight Center Greenbelt, Maryland 20771

Annual Status Report - Grant NAG5-2156
PI: John P. Hughes
October 23, 1996

This report is an update of progress on NASA grant NAG5-2156 since the last report (an Informal Status Report) of April 1996. The following papers, which were published or submitted since April, were supported by this grant. Preprints of each article are attached.

1.) "*HST* Observations of Oxygen-rich Supernova Remnants in the Magellanic Clouds. I. Narrow-band Imaging of N132D in the LMC," J. A. Morse, W. P. Blair, M. A. Dopita, J. P. Hughes, R. P. Kirshner, K. S. Long, J. C. Raymond, R. S. Sutherland, and P. F. Winkler, *Astronomical Journal*, **112**, 509.

2.) "Supernova Remnants Associated with Molecular Clouds in the Large Magellanic Cloud, " K. R. Banas, J. P. Hughes, L. Bronfman, and L.-Å. Nyman, *Astrophysical Journal*, submitted

Center for
Astrophysical
Sciences

HUBBLE SPACE TELESCOPE OBSERVATIONS OF OXYGEN-RICH SUPERNOVA REMNANTS IN THE MAGELLANIC CLOUDS.

I. NARROW-BAND IMAGING OF N132D IN THE LMC

J.A. Morse,[1,2] W.P. Blair,[3] M.A. Dopita,[4] J.P. Hughes,[5]
R.P. Kirshner,[5] K.S. Long,[1] J.C. Raymond,[5]
R.S. Sutherland,[4,6] and P.F. Winkler[7]

June 1996

Preprint Number 253

Preprint Series

The Johns Hopkins University
Bloomberg Center for Physics & Astronomy
Baltimore, Maryland 21218

HUBBLE SPACE TELESCOPE OBSERVATIONS OF OXYGEN-RICH SUPERNOVA REMNANTS IN THE MAGELLANIC CLOUDS.
I. NARROW-BAND IMAGING OF N132D IN THE LMC

J.A. Morse,[1,2] W.P. Blair,[3] M.A. Dopita,[4] J.P. Hughes,[5]
R.P. Kirshner,[5] K.S. Long,[1] J.C. Raymond,[5]
R.S. Sutherland,[4,6] and P.F. Winkler[7]

June 1996

Preprint Number 253

To appear in

The Astrophysical Journal

[1] Space Telescope Science Institute, 3700 San Martin Drive, Baltimore, Maryland 21218.
[2] Center for Astrophysics and Space Astronomy, Department of Astrophysical, Planetary and Atmospheric Sciences, University of Colorado, Campus Box 389, Boulder, Colorado 80309.
[3] Department of Physics and Astronomy, Johns Hopkins University, Charles and 34th Streets, Baltimore, Maryland, 21218.
[4] Mt. Stromlo and Siding Spring Observatoryies, Australian National University, Private Bag, Weston Creek Post Office, ACT 2611, *Australia*.
[5] Harvard-Smithsonian Center for Astrophysics, 60 Garden Street, Cambridge, Massachusetts 02138
[6] JILA, University of Colorado and National Institute of Standards and Technology, Campus Box 440, Boulder, Colorado 80309.
[7] Department of Physics, Middlebury College, Middlebury, Vermont 05753.

Hubble Space Telescope Observations of Oxygen-rich Supernova Remnants in the Magellanic Clouds. I. Narrow-band Imaging of N132D in the LMC[1]

JON A. MORSE[2,3], WILLIAM P. BLAIR[4], MICHAEL A. DOPITA[5], JOHN P. HUGHES[6], ROBERT P. KIRSHNER[6], KNOX S. LONG[2], JOHN C. RAYMOND[6], RALPH S. SUTHERLAND[5,7], P. FRANK WINKLER[8]

ABSTRACT

We present *Hubble Space Telescope* (*HST*) WFPC2 images of the young, oxygen-rich supernova remnant N132D in the Large Magellanic Cloud in the [O III]λ5007, [O II]$\lambda\lambda$3727 and [S II]$\lambda\lambda$6724 emission lines, plus a visible continuum band. The $\sim$0$''$.1 resolution of *HST* allows us to analyze structure within N132D at scales comparable to ground-based images of nearby remnants such as Cas A. The oxygen-rich filaments (seen in [O III] and [O II] emission) are easily distinguished from shocked circumstellar clouds (seen in all three emission lines). Characteristic knots sizes and filament widths are $\sim$ 0$''$.2 - 0$''$.5 ($\sim 1.5 - 4 \times 10^{17}$ cm), at least partially resolved in our images. For the first time, we discern ionization structure within the shocked interstellar clouds and filaments, reminiscent of filaments in galactic SNRs that are thought to arise from recent shock/interstellar cloud encounters where the full cooling and recombination zone has not yet formed throughout the structure. Conversely, there appears to be fairly uniform ionization in the O-rich filaments. We also observe highly ionized, diffuse emission extending all the way around the outer edges of the remnant, as previously seen in ground-based studies. We compare our *HST* optical emission-line images of N132D to the *ROSAT* HRI soft X-ray image and find that the X-ray emission is closely

---

[1] Based on observations with the NASA/ESA *Hubble Space Telescope*, obtained at the Space Telescope Science Institute, which is operated by the Association of Universities for Research in Astronomy, Inc., under NASA contract NAS5-26555.

[2] Space Telescope Science Institute, 3700 San Martin Dr., Baltimore, MD 21218

[3] Center for Astrophysics and Space Astronomy, Department of Astrophysical, Planetary and Atmospheric Sciences, University of Colorado, Campus Box 389, Boulder, CO 80309

[4] Department of Physics and Astronomy, Johns Hopkins University, Charles and 34th Streets, Baltimore, MD 21218

[5] Mt. Stromlo and Siding Spring Observatories, Australian National University, Private Bag, Weston Creek Post Office, ACT 2611, Australia

[6] Harvard-Smithsonian Center for Astrophysics, 60 Garden St., Cambridge, MA 02138

[7] JILA, University of Colorado and National Institute of Standards and Technology, Campus Box 440, Boulder, CO 80309

[8] Department of Physics, Middlebury College, Middlebury, VT 05753

traced optically by shocked circumstellar clouds; the O-rich filaments do not appear to be emitting X-rays. The limb-brightened X-ray shell aligns remarkably precisely along the inner edge of the diffuse outer rim. The diffuse emission probably represents ambient molecular gas that is being dissociated and photoionized by high-energy photons originating in the fast SNR shocks.

We have used the MAPPINGS II code to model the X-ray producing main blast wave as an ~ 800 km s^{-1} shock moving into a circumstellar medium of density $N_0 \approx 3$ cm^{-3}. The preshock ISM density of $N_0 \approx 3$ cm^{-3} inferred from our shock model agrees with the preshock density estimated from the [O III]λ5007 surface brightness in the diffuse outer rim. We also model the [O III]/[S II] emission-line ratios in the photoionized outer rim as a function of distance ahead of the main blast wave using the radiation field produced by fast shocks in the remnant as the ionizing source. According to our models, the ionizing radiation from the ~ 800 km s^{-1} main blast wave is not sufficient to generate the observed optical emission from the outer rim precursor. An extra source of EUV photons appears necessary to achieve the observed ionization of the preshock gas. We estimate that EUV photons produced in slower shocks moving into QSF-type clouds around the outer rim can probably contribute enough ionizing photons to achieve the observed ionization. Radiative shocks moving through the O-rich filaments may also be an important source of EUV photons.

1. INTRODUCTION

Elemental abundance determinations in supernova ejecta are fundamental for testing theories of nucleosynthesis occurring in massive stars, and, ultimately, models for the chemical enrichment of the interstellar medium (ISM) in galaxies. There is a class of young supernova remnants (SNRs), known as "oxygen-rich" (or "O-rich") SNRs, in which stellar interior fragments are exposed to direct investigation, providing us with an opportunity to make these crucial abundance measurements. There are only eight known oxygen-rich SNRs, Cas A being the most famous (e.g., Chevalier & Kirshner 1979). The O-rich SNRs are all thought to have evolved from Type II supernova explosions of Population I stars. Besides Cas A, there are two additional objects in the Galaxy, two in the Large Magellanic Cloud (LMC), one in the Small Magellanic Cloud (SMC), and two unresolved sources in the more distant galaxies M83 and NGC 4449. Obtaining reliable abundance measurements in these objects has been difficult owing to the high extinction toward the Galactic remnants (precluding UV observations of the line-emitting knots and filaments), and poor spatial resolution of the extragalactic sources.

Observations with the *Hubble Space Telescope* (*HST*) allow us to overcome the latter of these two impediments by providing 0″.1 angular resolution, sufficient to isolate individual knots in the Magellanic Cloud SNRs, as well as full UV/optical wavelength coverage. The O-rich SNRs in the Magellanic Clouds are excellent objects to study because their distances are well-determined and the line-of-sight extinction is low enough to allow UV spectroscopy (Blair et al. 1989; Blair, Raymond, & Long 1994). The UV provides access to additional ionization stages of elements such as O and Ne, as well as abundance information for C, Mg and Si that cannot be obtained from optical spectra.

The young, oxygen-rich SNR N132D is located in the bar of the LMC and was first identified as a supernova remnant by Westerlund & Mathewson (1966). Discovery of its O-rich nature was made by Lasker (1978) and Danziger & Dennefeld (1976). Spectroscopic studies (Danziger & Dennefeld 1976; Lasker 1980; Dopita & Tuohy 1984) revealed high-velocity filaments showing optical emission from O and Ne only, spanning a total velocity range of ~ 4400 km s^{-1}. The O-rich filaments are located toward the middle of the remnant. Outside the distribution of fast-moving material is a bright X-ray shell (Long, Helfand, & Grabelsky 1981; Mathewson et al. 1983) that is associated with a faint optical emission-line rim (Hughes 1994; Blair et al. 1994) of radius $\lesssim 1'$ (~ 13 pc). Dickel & Milne (1994,1995) found that the 6 cm radio emission from N132D, arising presumably from synchrotron emission behind the main blast wave, largely coincides with the X-ray shell and has a radially aligned magnetic field, characteristic of young SNRs that are in a pre-Sedov expansion phase.

Two recent ground-based optical studies, by Sutherland & Dopita (1995a; hereafter referred to as SD95a) and by Morse, Winkler, & Kirshner (1995; hereafter referred to as MWK), have provided new details about the morphology and dynamics of N132D. These authors used modern CCD imaging and Fabry-Perot and longslit spectroscopic techniques to characterize more accurately the spatial distribution and kinematics of the O-rich filaments than was previously possible. The O-rich filaments extend to a radius of ~ 6 pc from the remnant center, roughly twice the radius estimated by Lasker (1980). This led to a factor of two increase in the estimated age of the remnant, from ~ 1300 years to $\sim 2500 - 3000$ years, assuming that the uncontaminated ejecta have suffered little if any deceleration. In addition, SD95a and MWK each concluded that the ejecta probably are not distributed in an annulus as described by Lasker (1980), but seem to follow a (possibly asymmetrical) shell-like expansion. The mean velocity of the O-rich filaments is blueshifted several hundred km s^{-1} from the velocity of the local interstellar gas (Danziger & Dennefeld 1976; MWK), which may indicate a somewhat asymmetric explosion.

In this work we expand on these previous investigations of the structure of N132D by examining high spatial resolution images of this intriguing and important SNR obtained with the Wide Field and Planetary Camera 2 (WFPC2) aboard *HST*. In a companion paper (Blair et al. 1996) we will present UV/optical *HST* spectroscopy of the supernova ejecta in N132D obtained with the Faint Object Spectrograph (FOS). During our analysis, we adopt a distance to the LMC and N132D of 50 kpc (e.g., Panagia et al. 1991; Bertelli et al. 1993), corresponding to a spatial scale of $1'' = 10$ Wide Field Camera pixels $\approx 7.5 \times 10^{17}$ cm.

2. WFPC2 IMAGING AND DATA REDUCTION

The data presented here were obtained with the WFPC2 aboard *HST* on 9–10 August 1994. N132D was imaged through narrow- and broad-band filters to isolate several emission lines and a line-free continuum band to distinguish stars from stellar-appearing emission knots. We have used the images to study the small-scale structure of the line-emitting filaments in N132D, and also to select targets for UV/optical spectroscopy with the FOS (Blair et al. 1996). Figure 1 displays a ground-based [O III]λ5007 image from MWK showing the placement of N132D within the WFPC2 field of view. The remnant was positioned so that most of the bright emission was imaged onto the WF3 CCD chip, which allowed us to measure accurate relative positions for the spectroscopic targets. However, some emission from the northern and eastern outer rim fell outside the field of view. Our observing log is contained in Table 1, where we have listed the filter name, mean wavelength and effective width, total integration time, and the major spectral contributor in each bandpass.

The images were reduced with the IRAF/STSDAS[9] software package. Standard STSDAS/WFPC2 pipeline files and procedures were used for the first three reduction steps — bad pixel masking, A/D correction, and bias subtraction. We then performed the remaining reduction steps outside the WFPC2 pipeline (cf. Heathcote et al. 1996), following the recommendations of the WFPC2 instrument team (Holtzman et al. 1995a). As part of the WFPC2 internal monitor program, bias and dark frames are frequently obtained on-orbit. Holtzman et al. (1995a) describe how high signal-to-noise "superbias" and "superdark" frames are constructed at quasi-regular intervals from these datasets in order to monitor long-term variations in the bias structure and dark current for each chip. The closest in time on-orbit superbias frame was scaled and subtracted from our images to correct for the remaining low-level bias structure. Next, a superdark frame was scaled and subtracted to correct pixels that have roughly constant dark rate. Pixels with significantly different or rapidly varying dark rate ("hot pixels") were adjusted by subtracting a so-called "delta dark" image — the difference between the superdark and the dark frame nearest in time to our observations. To correct for the pixel-to-pixel response and variations in the illumination, we applied the latest available on-orbit flat fields for each filter and CCD chip.

We measured no significant shifts between the images taken through each filter, and so combined the individual frames into respective emission-line and continuum images. We used the STSDAS task **crrej** to remove cosmic rays during the averaging process, with 5σ and 4σ rejection iterations and 3σ rejection for neighbors. This technique removed $\sim$ 80% of the cosmic rays; the remaining cosmic rays and hot pixels not corrected by the dark correction were removed individually using the IRAF task **imedit**. After the cosmic rays were removed, the images representing the total for each bandpass were registered to within a fraction of a pixel using the positions of $\sim$ 15 stars in each chip as tie points.

---

[9] The Image Reduction and Analysis Facility (IRAF) is distributed by the National Optical Astronomy Observatories, which is operated by the Association of Universities for Research in Astronomy, Inc., under contract to the National Science Foundation. The Space Telescope Science Data Analysis System (STSDAS) is distributed by the Space Telescope Science Institute.

The F547M continuum image was scaled and subtracted from each of the on-band frames to form "pure" emission-line maps. This step was important due to the high density of the star field in the LMC bar region and our desire to measure characteristic sizes of the knotty, nearly stellar-appearing SNR knots and filaments. The aligned continuum image was first scaled in intensity by the ratios of the exposure times and filter efficiencies, plus a color term to account for the differences in wavelength. Then, the result was subtracted from the emission-line images. This method was effective for removing the vast majority of faint stars. However, variations in spectral type among the brighter stars resulted in noticeable residuals in the continuum-subtracted [O II] and [S II] images which were far away in wavelength from the continuum band. These residuals were corrected individually using the task **imedit**. Residual errors in the subtraction of some bright stars that overlapped with the emission-line filaments were not corrected, though there were only a few such cases.

Finally, the emission-line maps were flux calibrated by multiplying the pixel values by the system throughput (Holtzman et al. 1995b) at the appropriate wavelength (following the methods described in Heathcote et al. 1996). Unfortunately, the throughput of the F375N filter has not yet been re-measured on-orbit by the WFPC2 instrument team. We found better agreement with ground-based spectroscopic measurements of the [O II]$\lambda\lambda$3727/[O III]λ5007 line ratio in selected filaments (e.g., SD95a; MWK) if we used a system throughput for F375N closer to $\sim$1%, rather than 0.8% listed by Holtzman et al. (1995b). However, we regard this estimate as very tentative. The WFPC2 [O III]λ5007 and [S II]$\lambda\lambda$6724 emission-line flux calibrations are estimated to be accurate to $\sim$5% (Holtzman et al. 1995b; Tsvetanov et al. 1996) for those filaments with relatively small Doppler shifts, where the emission was transmitted close to the peak of the filter curves. Some high-velocity O-rich filaments fall on the steep wings of the F375N and F502N filter bandpasses (or are shifted out of the bandpasses completely!) so the emission-line fluxes in these filaments are not accurate. We discuss these special situations below.

We have labeled several structures, to which we later refer, in the ground-based [O III] image of N132D shown in Fig. 1. Important features include the oxygen-rich filaments (color-coded according to their kinematics) and several shocked interstellar clouds. In Fig. 2a–c, we present the final continuum-subtracted WFPC2 emission-line maps of N132D, where we have scaled the intensities logarithmically and adjusted the contrast to emphasize faint emission. The F547M continuum image is shown in Fig. 2d. We also show, for later comparison, the *ROSAT* High Resolution Imager (HRI) soft X-ray map in Fig. 2e, adjusted to the same spatial scale and orientation as the *HST* images. The *ROSAT* HRI image was registered to the *HST* images using the nominal aspects from both spacecrafts, respectively, as recorded in the image headers. We corrected the nominal astrometry of the *ROSAT* HRI image by $\sim 1''\!.5$ (3 HRI pixels) to the south using the position of an X-ray emitting star (HD 36436) located $\sim 4'$ NE of N132D as a reference point. To improve the spatial resolution of the X-ray map, we deconvolved the HRI image for 20 iterations with the Lucy-Richardson algorithm using an axisymmetric model (David et al. 1992) to represent the HRI point spread function. The final *ROSAT* HRI image has an effective resolution of $\sim 3''$ FWHM.

3. RESULTS

3.1. Large-scale Morphology of the Line-emitting Gas

Morphological differences between the WFPC2 emission-line images of N132D result from both resolved ionization structure and chemical fractionation. These differences are highlighted in Fig. 3, which shows a "true-color" image of the bright inner regions of N132D, with [O II]$\lambda\lambda$3727 in blue, [O III]λ5007 in green, and [S II]$\lambda\lambda$6724 in red. The cross in Fig. 3 marks the approximate position of the geometrical remnant center.

Oxygen-rich filaments. The O-rich ejecta, which do not emit in [S II] (e.g., Lasker & Golimowski 1991), are clearly distinguished in Fig. 3 as the blue-green filaments. Referring to Fig. 1 and the labeling scheme of MWK, we identify the following O-rich filaments: B1, the vertical filament in the SW quadrant of the image (lower right; see Fig. 7); R2, the vertical filament near the center of the image aligned roughly parallel to B1; and R1, stretching horizontally below the bright pinkish filament, left-center in the image. The bright O-rich clump that abuts the pinkish filament at the eastern edge of the image is the complicated region analyzed by SD95a and MWK which contains multi-peaked line profiles due to overlapping emission from filaments R1 and B4. The rest of the B4 filament lies off the edge of the field of view (see Fig. 1). The high-velocity filaments B2 and B3, which would be located in the lower left quadrant of Fig. 3, are blueshifted out of the filter bandpasses and do not appear in the image. B1 is the only O-rich filament that we are confident is contained wholely within the filter bandpasses. The R1 and R2 filaments are both redshifted into the wings of the F502N and F375N filters. These filaments appear bluer than the B1 filament because relatively more [O II]$\lambda\lambda$3727 emission is admitted due to the higher redshift of the F375N central wavelength; the blueness is probably *not* caused by different ionization structure as compared to B1.

Shocked interstellar clouds. Strong [S II] emission indicates where gas that surrounded the progenitor star (either ISM clouds in the vicinity of the progenitor or in some cases perhaps circumstellar material ejected in a pre-supernova outflow phase) has been shocked by the main blast wave, and is radiatively cooling. These filaments generally appear pinkish in Fig. 3 though the color variations indicate that we have, for the first time, resolved some of the ionization structure. The spatial distributions of the [O II] and [S II] emission are largely correlated in these normal-abundance filaments (see also Fig. 2), yielding a pinkish hue rather than deep red. The filaments appear gray/white where [O III] emission is also strong; these regions have relatively higher temperatures and the cooling is not as advanced. The kinematic data of MWK indicate that these filaments have radial velocities generally in the range ±200 km s^{-1}, and are analogous to the quasistationary flocculi (QSF) seen in Cas A (e.g., Chevalier & Kirshner 1979). These velocities are low enough such that all of the emission from the QSF-like regions is safely contained within the filter bandpasses.

Photoionized precursor. Also visible in Fig. 3 are areas of diffuse emission, brightest in [O III]. The region near top-center of Fig. 3 that appears green is a good example. MWK suggested that this diffuse emission represents ISM material lying ahead of the main shock wave that has been photoionized by high energy photons produced in the fast SNR shocks (see §4.1 and §4.2). This faint, diffuse component extends all the way around the outer edges of the remnant (see Fig. 2a).

3.2. Fine-scale Morphology

The color image in Fig. 3 easily differentiates the O-rich ejecta from the more normal abundance shock-heated material, but only hints at the level of structure visible in the images. The $\sim 0''.1$ resolution of the *HST* images allows us to study the filamentary structures in this LMC remnant with approximately the same detail as a ground-based image of Cas A (distance $\sim$ 3 kpc; Reed et al. 1995) obtained in $1''.6$ seeing. In this section we describe the appearance of these data on fine scales by selecting various subsections of the images for detailed comparison. The regions discussed below are identified with boxes in Fig. 2a. Figures 4, 5, 6, and 8 show the [O III] and [S II] images in panels a) and b), with the intensity scaling set to show the brightest features. Panels c) and d) of each figure duplicate panels a) and b) but with scaling set to show the faintest emission. Figure 7 is the same except that it shows the [O II] data in place of [S II].

Figure 4 shows a $10'' \times 20''$ region that corresponds roughly with IUE position 1 (IUE-P1) of Blair et al. (1994). (The edge of the WFPC2 field does not allow an exact positioning.) Even at ground-based resolution, Blair et al. (1994) could tell that both normal-abundance material and O-rich ejecta were contained within the IUE aperture, and this is seen dramatically in the figure. The eastern edge of the bright, curved normal-abundance filament from Fig. 3 (which we shall call "Lasker's bowl" [Lasker 1978]; see Fig. 1) dominates the [S II] emission. This normal-abundance material can be seen also in the [O III] image, although with considerably different structure and relative intensity at places (cf. Fig. 3). Most of the [O III] emission comes from a collection of O-rich knots, some of the brightest in the remnant. (Some O-rich emission may be lost from the F502N filter bandpass because of the large spread of velocities in this region; cf. MWK.) The figure shows a nearly complete mutual exclusivity between the bright [O III] knots and [S II] knots; only a few southern-most [S II] knots are seen within the O-rich ejecta region, and there is no direct correspondence, indicating they are probably seen in projection and may not be directly interacting. This comparison highlights a difference between N132D and Cas A, where many individual ejecta knots are both O and S enriched (Chevalier & Kirshner 1979).

Figure 5 enlarges a $15'' \times 20''$ region that corresponds with IUE-P2 of Blair et al. (1994). The IUE aperture was tipped at a PA of 36.4°, roughly upper left to lower right in this figure. The area shown corresponds to the central and western regions of Lasker's bowl. This region is completely dominated by ISM (or circumstellar) material, showing no evidence of O-rich knots (cf. Fig. 3). As such, most of the differences in appearance are driven by varying ionization in the shocked material being encountered by the blast wave. This ionization structure is evident on many scales. The filaments extending northward from Lasker's bowl appear as a "tree" in Fig. 3, where the "trunk" appears white (bright in all three emission line images) and the "branches" appear pink ([S II] and [O II]). This dichotomy is clearly evident in Fig. 5.

However, ionization changes also occur along individual filaments (cf. the westernmost filament extending to the upper right in Fig. 5) and across some filaments in Lasker's bowl (cf. Fig. 3), at or near our ability to resolve with WFPC2. These structures are very reminiscent of filaments in the Cygnus Loop and other Galactic SNRs that are thought to arise from very recent shock/interstellar cloud encounters where the full cooling and recombination zone has not yet formed throughout the structure. Many of the most "knotty" structures appear mainly in the [S II] image, where the the gas is the coolest, the most compressed and may be subject to fragmentation caused by dynamical instabilities (e.g., Klein, McKee, & Colella 1994).

Figure 6 highlights a complex of bright knots on the western limb of N132D, seen at the right edge of Fig. 3. The region shown is $15'' \times 20''$. Again, no evidence for O-rich ejecta is present, and we expect (both from the position on the X-ray rim and from the observed line intensities) that this material represents shocked interstellar gas and clouds. As in Fig. 5, ionization structure is visible on large and small scales: [O III] emission is seen systematically on the leading edge of the region (toward the upper right in the figure), and several examples of resolved knots with [O III] leading edges are visible (note green and/or white edges in Fig. 3). Again, the knottiest structure is evident in the [S II] image.

Figure 7 shows a $12'' \times 25''$ region encompassing the O-rich filament B1, seen in projection $\sim 5 - 6$ pc from the center of N132D. Unlike the others, this figure shows a comparison of [O III] and [O II] since there is no [S II] emission visible at this location. This region contains material of relatively low blueshift that should be mainly passed by the filters used. Comparing the separate panels in Fig. 7, as well as the uniform coloring of the region in Fig. 3, suggests that little variation in the relative line intensities is present in these filaments, indicating fairly uniform ionization levels.

One potentially interesting aspect of Fig. 7 is that the faint filamentary structures generally appear to be elongated horizontally. This pattern may result from Rayleigh-Taylor instabilities (present either early in the SN explosion, or developing over time as the ejecta expand into space) that are swept back along the flow direction. The B1 filament has a low radial velocity but is seen at large radius, so its motion is largely transverse to our line of sight, consistent with the direction of elongation in the filaments. Similarly, the R1 filament, with moderate redshift and located just below Lasker's bowl (see Figs. 1 and 2a), is projected at the top of the O-rich distribution and its fine-scale features appear to align mostly vertically. In contrast, the small-scale structures in the R2 filament lack this apparent organization. The R2 filament has the largest redshift among the

O-rich filaments, and any swept back structures may be hidden by its motion being directed away from us.

Figure 8 selects a $25''$ square region on the southern rim that shows a loose collection of emission knots and the diffuse rim. This region shows many similarities to the west complex (Fig. 6). Many more knots appear in the [S II] image and, although this region is not included in Fig. 3, some of the [O III]-emitting knots show the same apparent ionization structure as described for Fig. 6. A number of knots in this region are elongated in a roughly radial direction, although superposition of multiple unresolved knots cannot be entirely ruled out. The knots brightest in [O III] emission generally are found toward the outer edges compared to [S II] knots in the vicinity. As in other regions, we are apparently witnessing the evolution of the postshock cooling as the main shock wave encounters the ISM; the [O III] emitting regions form closer to the shock front, and [S II] becomes relatively stronger as the gas continues to radiatively cool.

Although the intensity levels are low in Fig. 8, the diffuse emission in the [O III] image is evident. The sharp inner edge of the diffuse emission in the [O III] image may indicate the location of the shock front (see §4.1). Consistent with this picture are the bright (postshock) knots having a tendency to be associated with the *inner* edge in this region. Some bright clumps appear to lie within the diffuse emission, but this could easily be due to projection effects. Diffuse emission is also visible in the [S II] image, but even farther outside the knots (toward the bottom of the figure). In the higher contrast panels, considerable structure is evident in the diffuse [O III] and [S II] emission.

3.3. Characteristic Knot Sizes in the Shocked Interstellar Clouds and O-rich Ejecta

We measured the sizes of individual knots in the various sub-regions described in the preceding section. Several relatively bright and isolated knots from each region were selected and classified as either "interstellar" or "ejecta." Gaussian fits to the radial brightness profiles of the knots (using the IRAF task **imexamine**) yielded full-width at half maximum (FWHM) sizes ranging from $0''\!.2$ - $0''\!.5$, or $\sim 1.5 - 4 \times 10^{17}$ cm for both interstellar and ejecta knots, with no obvious difference between the ISM and ejecta subsets.

To characterize the more global knot and filament properties in N132D, we performed autocorrelations on each of the sub-images shown in the boxes in Fig. 2a (see also Figs. 4–8) using the STSDAS task **autocorr**. An autocorrelation is produced by comparing an image against itself, assuming various relative offsets. The result of the **autocorr** task is an image file the same size as the original containing the autocorrelation of the image. Any characteristic spot size in the original image shows up as a central peak in the autocorrelation image with a FWHM approximately 1.5–2 times larger than the original spot size, assuming the point spread function is roughly gaussian. This central peak may be surrounded by a plateau with various symmetry properties, depending on whether there is diffuse or filamentary structure in the original image and on the size of the region being autocorrelated.

A subset of the autocorrelations is shown in Fig. 9. The upper left image is the autocorrelation of a section of our F547M continuum exposure containing numerous stars, showing a strong, symmetrical central peak and very little background structure. The central peak in this image has a gaussian FWHM of ~ 2.5 pixels in both X and Y dimensions, about 1.7 times the FWHM of a typical stellar radial brightness profile from the original (WF3) image.

The [O II], [O III] and [S II] autocorrelations of all five sub-fields outlined in Fig. 2a contain a wide variety of structures, but all show a central peak resting on a plateau of varying extent and symmetry. The additional autocorrelation images shown in Fig. 9 — the [O III] autocorrelation of the O-rich ejecta filament B1 from the central region of the remnant, and the [O III] and [S II] autocorrelations of the IUE-P2 sub-field — illustrate several general features of the emission structures observed: (1) The central spots in the emission-line autocorrelations are somewhat broader than the central peak in the continuum autocorrelation, indicating that typical knots are at least partially resolved. The characteristic knot sizes indicated by the measured central spot FWHMs (divided by ~ 1.7) are mostly in the 2–4 pixel range, or $0''.2$–$0''.4$. (2) The [O III] and [S II] autocorrelations differ in the QSF-like regions such as IUE-P2. The contrast between the central peak and extended plateau in the [O III] correlations is generally lower compared to the [S II] correlations. The [O III] emission appears to be more filamentary while the [S II] emission emanates from knotty structures. In IUE-P2, there is a strong linear plateau in the [O III] correlation indicating considerable power in filamentary structures. The [S II] autocorrelation, on the other hand, has a stronger central peak with only some elongation in the extended plateau; the [S II] emission comes from a more random distribution of compact structures. This difference might indicate that the compressed gas undergoes cooling instabilities and fragments as the temperature falls from $\sim 30,000$ K in the [O III] emitting zone to $\lesssim 10^4$ K in the [S II] emitting zone in the radiative shocks. Alternatively, by the time the gas has cooled to 10^4 K, the magnetic pressure may dominate the thermal pressure. The magnetic field may be chaotic enough to cause large variations in the density (hence, emissivity) in the [S II]-emitting zone (e.g., Raymond & Curiel 1995). (3) The [O III] autocorrelation of the O-rich filament B1 has a relatively strong central peak. Most of the power is contained in emission from compact knots, in contrast to the [O III] structure in IUE-P2 and other QSF-like regions. If photoionization dominates the ionization in the ejecta, then the ejecta must have fragmented earlier in their evolution, possibly due to Rayleigh-Taylor and Kelvin-Helmholtz instabilities that formed during the supernova explosion (Burrows, Hayes, & Fryxell 1995). Alternatively, Sutherland & Dopita (1995b) have shown that the extremely strong cooling rate in the high-Z ejecta plasma leads to very compressed emitting structures when the gas is shocked. (In Blair et al. 1996, we discuss the ionization mechanism acting in the ejecta.) The plateau of the B1 autocorrelation has most of its power in three elongated structures extending in the E-W direction. Because this filament is moving roughly transverse to our line of sight, the elongation shows that in general the filamentary structures are stretched along the direction of motion. The ringing which produces the three horizontal bands indicates a somewhat periodic spacing of filaments in the N-S direction.

4. DISCUSSION

4.1. Comparison to the Soft X-ray Emission

Blair et al. (1994) were the first to recognize that the soft X-ray emission observed with the *Einstein* HRI is associated with optical features that have normal abundances, and generally does not spatially align with the oxygen-rich filaments. In addition, these authors noted that the outer X-ray shell, especially in the southern half of the remnant, is displaced several arcseconds inside the diffuse optical emission along the outer rim. MWK confirmed both of these findings by comparing the deeper *ROSAT* HRI image of Hughes (1994) with high signal-to-noise Fabry-Perot images in [O III]λ5007. MWK also showed from longslit spectra that the diffuse optically emitting gas along the outer rim is highly ionized but has apparently normal (LMC) abundances. This diffuse emitting gas has narrow line widths and lies at the same radial velocity as the molecular gas in the region (Hughes, Bronfman, & Nyman 1989). These characteristics led MWK to conclude that the diffuse emission emanates from gas that lies ahead of the main blast wave and is being photoionized by high-energy photons created in the fast SNR shocks.

Figure 10 shows a color composite image of the WFPC2 field displayed in Fig. 2 with the *ROSAT* HRI soft X-ray map in blue, the *HST* [O III]λ5007 map in green, and the *HST* [S II]$\lambda\lambda$6724 map in red. This image illustrates the points made in the preceding paragraph: (1) The brightest X-ray ridges spatially align with the narrow filaments and compact knots seen primarily in [S II]. X-ray emission does not appear to emanate from the O-rich filaments. There is an X-ray ridge which extends from the southwest rim and overlaps the O-rich filament R2 near the middle of the remnant. However, comparing Figs. 2b and 2e reveals that the X-ray emission through the remnant center is closely traced by [S II]-emitting knots. The overlap with R2 is probably a projection effect. For instance, the O-rich filament B1, to the lower right of R2, has no associated X-ray emission. (2) The soft X-ray shell aligns remarkably precisely along the sharp inner edge of the diffuse optical outer rim where the blast wave interacts with the ISM. The inset of Fig. 10 highlights a region in the southwest quadrant of the remnant which shows this interaction. The limb-brightened X-ray rim marks the position of the shock front (moving tranverse to the line of sight), where the shock heats and accelerates the gas it enounters. Compact knots along the inside of the X-ray rim radiate optical line emission where the compressed gas has cooled to $\sim 10^4$ K.[10] Out in front of the X-ray rim is the diffuse photoionized precursor that extends up to

---

[10] Similar [S II]-emitting clumps associated with X-ray ridges near the middle of the remnant have radial velocities up to several hundred km s^{-1} relative to the local medium, showing that, as expected, this material has been accelerated along the line of sight.

$10''$ from the shock front. The precursor gas is highly ionized close to the shock front (bright in [O III]) and becomes relatively less ionized (brighter in [S II]) with distance from the X-ray rim.

The top panel of Fig. 11 shows one-dimensional flux tracings of the optical and X-ray emission along the direction perpendicular to the shock front shown in the inset of Fig. 10. The flux from the optical images was summed along columns of 30 pixels ($3''$) directly above the white brackets in the inset. The X-ray flux was summed in a similar manner and then scaled down by a factor of ~ 50 for plotting purposes. The horizontal spatial scale is given in arcseconds relative to our estimated position of the shock front, shown by the vertical line in the plot. This line was drawn at the position of the sharp inner edge of the diffuse [O III] emission, though there is an uncertainty of $\sim \pm\ 0\overset{\prime\prime}{.}3$ in this position due to small-scale inhomogeneities and slight curvature along the $3''$ length of the optical rim. The X-ray emission peaks a couple of arcseconds inside the vertical line, which is expected if the true limb-brightened X-ray emission at the edge of the shell resembles a saw-toothed distribution that is convolved with the (symmetric) $\sim 4''$ FWHM point spread function of the *ROSAT* HRI.

We can estimate the density of the precursor gas into which the blast wave is propagating from the observed surface brightness of the diffuse forbidden-line emission. The luminosity per unit volume $L_{4959,5007}$ of the [O III]$\lambda\lambda4959, 5007$ lines is related to the number density of doubly ionized oxygen atoms in the excited state N_2 and in the ground state N_1 within the [O III]-emitting region of the precursor by the equation (e.g., Osterbrock 1989)

$$L_{4959,5007} = N_2 A_{21} h\nu_{21} = N_1 N_e q_{12} h\nu_{21} \quad \text{ergs cm}^{-3}\ \text{s}^{-1} \tag{1}$$

where

$$q_{12} = \frac{8.63 \times 10^{-6}\, \Upsilon_{12}\, e^{-\left(\frac{h\nu_{12}}{kT_e}\right)}}{g_1\, T_e^{1/2}} \quad \text{cm}^3\ \text{s}^{-1} \tag{2}$$

is the collisional excitation rate coefficient, A_{21} is the total Einstein A-value for the transition, Υ_{12} is the collision strength, g_1 is the ground state statistical weight, and N_e and T_e are the electron density and temperature, respectively. Equation (1) assumes that the electron density is much lower than the critical density ($N_C \approx 8.1 \times 10^5$ cm^{-3}) for this transition. The total number N_1 of doubly ionized oxygen atoms in the ground state can be expressed in terms of the total number of particles by

$$N_1 = \left[\frac{N_1}{N(\mathrm{O}^{++})}\right] \left[\frac{N(\mathrm{O}^{++})}{N(\mathrm{O})}\right] \left[\frac{N(\mathrm{O})}{N(\mathrm{H})}\right] \left[\frac{N(\mathrm{H})}{N_{\mathrm{TOT}}}\right] N_{\mathrm{TOT}} \tag{3}$$

where $N(\mathrm{O}^{++})$, $N(\mathrm{O})$, $N(\mathrm{H})$ and N_{TOT} are the total number of doubly ionized oxygen atoms, total number of oxygen atoms, total number of hydrogen atoms, and total number of atoms in the region of interest, respectively. To a good approximation $[N_1/N(\mathrm{O}^{++})] \approx 1$. We assume an electron temperature $T_e \sim 15,000$ K in the [O III]-emitting region, and that oxygen is doubly ionized ($[N(\mathrm{O}^{++})/N(\mathrm{O})] \sim 1$; the weakness of He II$\lambda4686$ in the outer rim spectra of MWK suggests that He is mostly singly ionized, and therefore that oxygen is mostly O III rather than

O IV. From the LMC abundances of Russell & Dopita (1990), $[N(\mathrm{O})/N(\mathrm{H})] \approx 2.24 \times 10^{-4}$. We also approximate $[N(\mathrm{H})/N_{\mathrm{TOT}}] \sim 0.9$ and $N_{\mathrm{TOT}} \sim N_e$. Equation (1) can then be written

$$L_{4959,5007} \approx \left[\frac{N_1}{N(\mathrm{O}^{++})}\right]\left[\frac{N(\mathrm{O}^{++})}{N(\mathrm{O})}\right]\left[\frac{N(\mathrm{O})}{N(\mathrm{H})}\right]\left[\frac{N(\mathrm{H})}{N_{\mathrm{TOT}}}\right] N_e^2 \times \left[\frac{8.63 \times 10^{-6}\, \Upsilon_{12}\, e^{-\left(\frac{h\nu_{12}}{kT_e}\right)}}{g_1\, T_e^{1/2}}\right] h\nu_{21} \;\; \mathrm{ergs\ cm^{-3}\ s^{-1}} \qquad (4)$$

which reduces to $L_{4959,5007} \approx 2.12 \times 10^{-24} N_e^2$ ergs cm^{-3} s^{-1} using $T_e = 15{,}000$ K, ground state statistical weight $g_1 = 9$, collision strength $\Upsilon_{12} = 2.30$ (Mendoza 1983), and $h\nu_{21} = 3.97 \times 10^{-12}$ ergs. The Einstein A-values for the $^1\mathrm{D}_2 \rightarrow {}^3\mathrm{P}_1$ (λ4959) and $^1\mathrm{D}_2 \rightarrow {}^3\mathrm{P}_2$ (λ5007) transitions are 6.74×10^{-3} s^{-1} and 1.96×10^{-2} s^{-1}, respectively, so the λ5007 luminosity per unit volume L_{5007} can be related to $L_{4959,5007}$ by

$$L_{5007} = \frac{19.6}{(19.6 + 6.74)} L_{4959,5007} = 0.74\, L_{4959,5007}. \qquad (5)$$

Hence,

$$L_{5007} \approx 1.58 \times 10^{-24} N_e^2 \;\; \mathrm{ergs\ cm^{-3}\ s^{-1}}. \qquad (6)$$

The observed λ5007 luminosity per unit volume (i.e., volume emissivity)

$$L_{5007} = \frac{4\pi F_{5007}}{\Omega\, l} \;\; \mathrm{ergs\ cm^{-3}\ s^{-1}}, \qquad (7)$$

where, from Fig. 11, the observed λ5007 flux $F_{5007} \sim 2.5 \times 10^{-16}$ ergs cm^{-2} s^{-1} in a $3'' \times 0''.1$ aperture (solid angle $\Omega = 7.05 \times 10^{-12}$ sr). The (average) line-of-sight path length through the [O III]-emitting region — for an [O III] shell thickness of 1 pc (see Fig. 11) and outer shell radius of 13 pc — is $l \sim 2.3 \times 10^{19}$ cm. Combining the previous two equations for L_{5007} and solving for N_e gives

$$N_e \approx 7.96 \times 10^{11} \left(\frac{4\pi F_{5007}}{\Omega\, l}\right)^{1/2} \;\; \mathrm{cm^{-3}}. \qquad (8)$$

Plugging in the above values for F_{5007}, Ω and l yields a precursor electron density $N_e \approx 3.5$ cm^{-3}. If the gas has a clumpy distribution on scales smaller than the aperture, the local density will be somewhat higher. We show in the next subsection, however, that this density estimate is consistent with the preshock density derived from the (postshock) X-ray luminosity along the outer rim.

4.2. A Model for the Photoionized Outer Rim

We now discuss a model for producing the emission from the diffuse gas ahead of the X-ray shell. The general picture is that ionizing photons created in the fast SNR shocks propagate upstream and photoionize the ambient preshock medium. Preshock ionization caused by energetic photons created in fast shocks has been discussed by Shull & McKee (1979), Raymond (1979) and Dopita, Binette, & Tuohy (1984). A discussion of the formation and structure of extended, highly ionized H II regions in front of fast shocks in the context of active galaxies appears in Sutherland, Bicknell, & Dopita (1993) and Dopita & Sutherland (1996). In fact, the ground-based optical spectra of the outer rim in N132D (MWK) appear very similar to spectra of LINER and Seyfert 2 galaxies (Morse, Raymond, & Wilson 1996). The observed [O III] and [S II] precursor emission distributions shown in the tracings of Fig. 11 appear qualitatively very similar to the predictions of the photoionizing shock models of Dopita & Sutherland (1996; see their Fig. 4). A photoionized precursor has also been observed in the LMC remnant N49 (Shull 1983; Vancura et al. 1992).

In the bottom panel of Fig. 11 we plot the logarithm of the [O III]λ5007/[S II]$\lambda\lambda$6724 flux ratio, in $1''$ bins, as a function of distance from the shock front into the precursor. The error bars in the upper right corner show the typical uncertainty in the flux ratio measurements ($\sim$ 10%) in the vertical direction, and the bin size in the horizontal direction. The dereddened flux ratios were calculated using a standard extinction law (Cardelli, Clayton, & Mathis 1989) with E(B−V) $\approx$ 0.20 (see MWK). As previously mentioned, the tracings and measured flux ratios show the precursor gas to be highly ionized ([O III]/[S II] > 10) near the shock front and then gradually less ionized as one proceeds farther from the X-ray rim into the ISM until [O III]/[S II] becomes less than unity $\sim 7'' - 8''$ ($\sim 6 \times 10^{18}$ cm) out. Ground-based optical spectra of the southern optical rim (MWK) show that the flux ratio [O III]λ5007/H$\beta \approx 5 - 10$ in the precursor near the shock front, though it is difficult to distinguish the diffuse precursor emission from the compact knots along the X-ray border with the poor spatial resolution of the ground-based data.

In order to model the precursor emission, we need to determine the origin of the ionizing photons and the shape of the ionizing spectrum. Figure 10 strongly suggests that the X-ray rim may be an important source of ionizing photons. However, the photoabsorption cross-section to soft X-rays is relatively low (hence, we are able to detect the escaping X-rays). So it is necessary to extract information about the EUV ionizing photon field between $\sim 10 - 200$ eV seen by the precursor gas based on models of the X-ray rim and other shocks in the remnant. Below, we develop a model for the ionizing spectrum produced by the X-ray rim, elaborating on the work of Hwang et al. (1993; hereafter HHCM), and then discuss the possible contributions to this ionizing spectrum by other (slower) shocks in the remnant.

HHCM determined a temperature $T_e = 8.4 \times 10^6$ K and an ionization age $N_e t = 6.1 \times 10^3$ cm^{-3} yr, where N_e is the postshock electron density and t is the time since the gas was shocked, for the X-ray emitting gas in N132D based on a non-equilibrium ionization (NEI) analysis of high spectral resolution data from the Focal Plane Crystal Spectrometer and the Solid State Spectrometer, and lower spectral resolution data from the Imaging Proportional Counter and the Monitor Proportional Counter aboard the *Einstein Observatory*. From these X-ray spectral data, HHCM derived a set of abundances which were compared to models for the composition of Type II ejecta including a contribution from swept-up interstellar material. In fact, Fig. 10 suggests that the soft X-ray emission comes largely (if not exclusively) from shocked ISM or circumstellar material (see also Hughes 1987).

The X-ray emission in the *ROSAT* HRI image can be approximated by a spherical shell model with radius $\sim 46''$ (11 pc) and shell thickness $\sim 6''.6$ (1.6 pc, or $\sim 5 \times 10^{18}$ cm) centered at (J2000) $\alpha = 5^h25^m02^s$, $\delta = -69°38'36''$, within a couple of arcseconds of the remnant center determined by MWK from the distribution of O-rich ejecta. The actual shell thickness at a particular location along the X-ray rim is probably smaller than the above estimate because it is clear from Fig. 2e that the outer X-ray rim exhibits several wiggles and protrusions that would inflate the azimuthally averaged estimate. Nevertheless, adopting these mean geometric parameters for the X-ray emitting gas, we can estimate the emission measure, using the spectral model from HHCM to convert the HRI count rate to 0.1–2 keV flux, and find a mean (postshock) electron density in the X-ray shell to be $N_e \sim 9$ cm^{-3}.

In the region shown in the inset of Fig. 10, the X-ray shell is roughly 2.5 times narrower than the shell thickness assumed above, based on a *post facto* examination of the scale-length of the X-ray emitting zone in the shock models discussed below, and the measured width of the X-ray rim in the tracing of Fig. 11. The electron density found from the emission measure then scales as the square-root of the shell thickness, yielding $N_e \approx 15$ cm^{-3} for a shell thickness $dr \sim 2 \times 10^{18}$ cm.

Because of the non-equilibrium conditions in the postshock region, it is not sufficient simply to use the jump conditions to determine the shock velocity by assuming the X-ray temperature determined by HHCM represents the peak postshock temperature. Even if the shock is very young, some cooling takes place over short timescales and the bulk of the X-ray flux is emitted by gas with a somewhat lower temperature than the peak postshock temperature achieved immediately behind the shock. As a result, we determined the (mean) shock velocity of the X-ray shell by matching the single-temperature NEI spectral model of HHCM with the output flux spectrum from a truncated shock model computed with the MAPPINGS II shock code (Sutherland & Dopita 1993; Dopita & Sutherland 1996). The two models were compared in the 0.2–4 keV X-ray band and the criteria for assessing the quality of the match were general agreement in (1) X-ray flux, (2) the shape, principally the slope, of the underlying thermal bremsstrahlung continuum, and (3) the predicted line emission. The slope of the underlying thermal bremsstrahlung continuum depends on the temperature, determined primarily by the shock velocity. The relative emission-line strengths will vary if different abundances are assumed in the models. It should be noted that the HHCM spectral model was determined for the integrated spectrum of N132D and that significant X-ray spectral variations from position to position are likely to be present. Consequently, a more sophisticated comparison with the results of HHCM is not warranted.

Figure 12 shows our shock model and the model fit to the *Einstein* spectral data for comparison. Both spectra contain a thermal bremsstrahulung continuum and a wide variety of line emission. The HHCM X-ray flux spectrum is normalized to an electron density $N_e \approx 14.6$

cm^{-3} and a shell thickness $dr = 1.9 \times 10^{18}$ cm. The parameters of the MAPPINGS II shock model needed to match this spectrum are a shock velocity $V_{sh} \approx 790$ km s^{-1} and a preshock density $N_0 = 3\ \text{cm}^{-3}$. A transverse magnetic field $B_0 = 1.7\mu$G (magnetic parameter $B/\sqrt{N} = 1\ \mu\text{G cm}^{3/2}$; see Dopita & Sutherland 1995), which had a negligible effect on the computed spectrum, and the LMC abundances of Russell & Dopita (1990) were assumed in the shock model. We truncated the shock model by limiting the postshock cooling time τ to $\sim$ 2500 yr, the maximum time allowed based on estimates of the remnant age (SD95a; MWK). The preshock ionization was set iteratively by using the output radiation field from one model run as the ionizing spectrum for the next run (see the description of this technique in Hartigan, Morse, & Raymond 1994). Aside from matching the slopes of the underlying thermal bremsstrahlung continua, the models share many similarities in the predicted line emission. The truncated shock model contains many more emission lines than the single-temperature model of HHCM, due to the variable ionization states that arise during the rapid heating and non-equilibrium cooling, producing prominent emission from hydrogen- and helium-like ions of the lighter elements such as oxygen. The MAPPINGS II code also calculates the H and He two-photon emission which results in the elevated continuum in the shock model at low energies.

The results of our shock modeling, simply stated, are that the mean shock velocity of the X-ray emitting main blast wave is $\sim$ 800 km s^{-1} and the mean preshock density is $\sim 3\ \text{cm}^{-3}$. It is possible that the "effective" age of the outer rim shock is less than the 2500 years we assumed. In this case the preshock density would need to be increased in order to match the observed soft X-ray flux. However, the value for the preshock density we obtain from the shock model is in excellent agreement with the estimate made in §4.1 based on the [O III]λ5007 surface brightness in the precursor. In our shock model, the peak postshock temperature achieved immediately behind the shock is 1.5×10^7 K, but after a cooling time of only a few years and a cooling distance of $\sim 1 \times 10^{15}$ cm, the temperature falls to 8.4×10^6 K and remains near that temperature for the duration of the run. High resolution imaging with AXAF may be able to detect this predicted high-temperature skin at the leading edge of the X-ray rim.

A shock velocity of 800 km s^{-1} is low compared to the $\gtrsim 10^4$ km s^{-1} shock speeds inferred from line-width measurements observed in Type II supernovae (e.g., Blanco et al. 1987). It is also low compared to the estimated mean velocity of $\sim$ 3700 km s^{-1} that the outer blast wave would need in order to expand to the observed radius of $\sim$ 11 pc during the lifetime of the remnant (MWK). We conclude, to no big surprise, that the outer blast wave must have been traveling faster in the past. The size and luminosity of the outer shell implies a total swept-up mass of $\sim 300 - 500\ M_\odot$ in the X-ray emitting material alone (Hughes 1987); the outer blast wave almost certainly is in the adiabatic expansion phase. The Sedov (1959) solution for the evolution of such a blast wave in a homogeneous medium predicts that the radius R of the X-ray shell proceeds as

$$R = 13(E_{51}/N_0)^{1/5}\, t_4^{2/5}\ \text{pc}, \tag{9}$$

where the explosion energy is given as $E_{51} = E/10^{51}$ ergs, the time since the explosion as $t_4 = t/10^4$ yr, and N_0 is the density of the circumstellar medium. Using $t_4 = 0.3$ (e.g., MWK), $R = 11$ pc and

$N_0 = 3$ cm^{-3} yields an explosion energy of $E = 1.4 \times 10^{52}$ ergs, probably unrealistically large. If instead we assume the explosion energy was 10^{51} ergs, and solve for the time since the explosion, we calculate $t \approx 11,400$ yr. This age estimate predicted by the Sedov solution is a factor of 3 – 4 times greater than is estimated from dynamical studies (SD95a; MWK).

In order to reconcile these results without positing an unusually large explosion energy, we adopt the scenario described by Hughes (1987) in which the density of the circumstellar medium, $N_0(R)$, is not uniform but varies as a function of radius. The supernova explosion may have occured in a very low-density cavity evacuated by a mass-loss phase of the progenitor star. The blast wave started out with a nominal expansion rate of $\sim 10^4$ km s^{-1}, and grew quickly in radius in the low-density medium. We can estimate an upper limit to the cavity density by solving Eq. (9) for N_0, assuming an explosion energy of 10^{51} ergs and using the observationally determined values of $R = 11$ pc and $t_4 = 0.3$. In this case, $N_0 \approx 0.2$ cm^{-3}. Since the present preshock density is an order of magnitude larger, it is probable that the cavity density was $\lesssim 0.1$ cm^{-3}. Estimating a functional form for $N_0(R)$ would be fairly arbitrary. The increase in the preshock density may have occured rapidly as the blast wave reached the edge of the evacuated cavity and now encounters the molecular cloud mapped by Hughes et al. (1989). A recent and rapid increase in the preshock density helps to explain why (1) the radius of the X-ray shell is so large for such a young remnant, (2) for its size, N132D is unusually bright in the X-rays, (3) the outer shock wave velocity of 800 km s^{-1} is so low compared to the mean velocity the blast wave would need to expand to the observed radius, and (4) the radio synchrotron emission observed by Dickel & Milne (1994,1995) indicates a radially aligned magnetic field, inferred to indicate pre-Sedov expansion.

Armed with our ~ 800 km s^{-1} truncated shock model spectrum shown by the solid line in Fig. 12, we used the MAPPINGS II code to compute the structure of a photoionized slab (Dopita & Sutherland 1996) of thickness $\sim 7 \times 10^{18}$ cm and density $N_0 = 3$ cm^{-3}, irradiated by high-energy photons produced by the X-ray emitting shock. The precursor photoionized slab was assumed to have an ionization structure like that of an equilibrium H II region. Our goal was to match the observed trend in the [O III]λ5007/[S II]$\lambda\lambda$6724 line ratio as a function of distance in front of the shock (Fig. 11). The ionizing shock spectrum must generate a relatively high precursor ionization state near the shock front. The observed ratios [O III]/[S II] $\gtrsim 10$ and [O III]/H$\beta \approx 5 - 10$ imply an ionization parameter, U, of at least 7×10^{-4} in the [O III]-emitting region.[11] The dimensionless ionization parameter, U, is defined as

$$U = \frac{4\pi N_{\rm phot}}{c N_0}, \tag{10}$$

where $N_{\rm phot}$ is the flux per sterradian of ionizing photons produced by the shock, c is the velocity of light, and N_0 is the precursor density. The ionization parameter changes with distance into the precursor because N_{phot} decreases with increasing optical depth, and the precursor density N_0 may be rising. The frequency dependence of the optical depth also changes the shape of the ionizing spectrum. As discussed below, additional ionizing photons from shocks elsewhere in the remnant may add to the local ionizing radiation field.

---

[11] The ionization parameter, U, near the shock front may be substantially higher than this value if there are significant ion fractions of O IV, O V and O VI (see Dopita & Sutherland 1996). However, we have no information on these higher ionization stages at this time.

According to our models, the (truncated) ~ 800 km s^{-1} shock does not have a high enough ionization parameter to generate the observed precursor emission-line ratios. The ionization parameter is a factor of ~ 2 too low and using this model spectrum alone to photoionize the precursor fails to achieve a high enough precursor ionization state; [O III]/[S II] $\lesssim 6$ and [O III]/Hβ ~ 3.5 over the first 10^{18} cm and the ratios fall from there. *We conclude that the X-ray emitting shocks in the outer rim are not solely responsible for generating the photoionized precursor emission.* Additional EUV photons that couple with the photons created in the X-ray rim appear to be required to produce the observed precursor ionization. Possible sources of additional ionizing photons include slower (non–X-ray emitting) shocks with shorter cooling times that are associated with the X-ray outer rim, or radiative shocks moving through the oxygen-rich ejecta (Sutherland & Dopita 1995b). We discuss the former possibility below and treat the latter in Blair et al. (1996).

Our models predict that the cooling time for the 800 km s^{-1} outer rim shock with a preshock density $N_0 = 3$ cm^{-3} is much longer than the age of the remnant. And yet we clearly see compressed knots and filaments radiating low-excitation optical emission lines characteristic of shocks that have cooled to below 10^4 K (Fig. 10; MWK). These regions must have lower shock velocities and/or higher densities, which result in relatively short cooling times. We therefore ran a short sequence of radiative shock models with higher densities and lower shock velocities in order to estimate which shocks become fully radiative within the lifetime of the remnant. If we assume that the blast wave has spherical symmetry and constant ram pressure per unit area, we can scale the mean shock velocity and density of the X-ray emitting (non-radiative) shell via the relation $V_2 \approx V_1\sqrt{N_1/N_2}$ to estimate the shock velocity in regions of higher density (McKee & Cowie 1975; Klein et al. 1994). Taking $V_1 \approx 800$ km s^{-1} and $N_1 \approx 3$ cm^{-3} to represent the parameters of the fastest shocks that produce most of the X-ray emission, clouds with densities $N_2 = 5$, 8, 16, and 25 cm^{-3} will have corresponding shock velocities $V_2 \approx 620$, 490, 350, and 280 km s^{-1}. We find that the $V_2 = 280$ km s^{-1} shock model (with magnetic parameter $B/\sqrt{N} \approx 1\mu$G cm$^{3/2}$) cools to below $T_e = 10^4$ K in ~ 1400 yr, well within the lifetime of the remnant, and reaches $T_e = 5000$ K by 2500 yr. On the other hand, the lower density $V_2 = 350$ km s^{-1} shock model cools to only a few hundred thousand degrees in 3000 yr. From this we infer that the fully radiative postshock clouds we observe ought to have shock velocities of ~ 300 km s^{-1}, or lower if the local interstellar cloud densities are higher than 25 cm^{-3}. These low shock velocities are consistent with the kinematics observed for the QSF-like clumps (MWK). It is also gratifying that in the 280 km s^{-1} shock model, the cooling distance to where the gas reaches $T_e \approx 10^4$ K is approximately 2×10^{17} cm, in agreement with the measured [S II] knot sizes. The cooling length in the model could be lengthened by using a higher magnetic parameter.

The general conclusion that slower shocks are abundant in the remnant is supported by the observation that in bright radiative knots and filaments, such as Lasker's bowl or the west complex, the X-rays are relatively fainter and the X-ray spectrum may be softer (Hughes 1994), both features consistent with slower shocks. The outer X-ray shell in the south and west quadrants in Fig. 2e exhibits several wiggles and protrusions that may indicate the shell is somewhat unstable and that the preshock medium into which it is advancing is non-uniform. It is probable that the X-ray emission is clumpy on scales smaller than the resolution of the *ROSAT* HRI. The sizes of the radiatively cooling postshock knots (see §3.3) suggest the interstellar cloud densities vary over small ($\sim 10^{17-18}$ cm) scales.

For our final model of the precursor emission, we used the "effective ionizing spectrum" shown by the thick gray line in Fig. 12. This spectrum sums the radiation field produced by the ~ 800 km s^{-1} X-ray emitting shock with the fields generated by the three lowest velocity high-density shock models discussed above. The ionizing flux contributed by slower shocks depends on the total surface area subtended by these shocks. Along the outer rim, the compact sizes of the fully radiative clumps suggest that this covering factor, f, is small. The surface area of the section of the X-ray shell shown in the inset of Fig. 10 is $\sim 2.3 \times 10^{39}$ cm^2. There are approximately 30 small radiative knots of typical radius $0''\!.2$, or 1.5×10^{17} cm, distributed along that section of the X-ray shell. Thus, the covering factor of the radiative clumps $f \sim 0.2\%$. Assuming a range of cloud densities, we therefore added in 0.2% of the flux emitted by the 490, 350 and 280 km s^{-1} shock models to arrive at the effective ionizing spectrum shown in Fig. 12. Due to their much lower temperatures, the low-velocity shocks contribute little or no thermal bremsstrahlung nor soft X-ray line emission above ~ 200 eV. However, they do contribute significant flux in the 20 – 80 eV range in the form of emission lines. Most of the extra emission lines in fact come from the 280 km s^{-1} model because it has cooled the furthest and has the highest density.

When this effective ionizing spectrum was used as the input spectrum for photoionizing the thick slab, we obtained the line ratios [O III]/[S II] ~ 12 and [O III]/H$\beta \sim 7$ near the shock front, as observed. However, the [O III]/[S II] ratios did not decrease with distance from the shock front as fast as is observed. We, therefore, gradually ramped up the precursor density (decreased the ionization parameter) by a factor of ~ 2 in order to match the [O III]/[S II] ratios observed $\gtrsim 6''$ from the shock front. Our computed line ratios using this model are compared to the observed line ratios in the bottom plot of Fig. 11. The overall behavior of our computed [O III]/[S II] line ratios is similar to the observed trend, though there is slightly too much [O III] emission near the shock front and too little several arcseconds out.

Our need to ramp up the precursor density in order to match the low [O III]/[S II] ratios far from the shock front is not surprising if in fact the blast wave is encountering the edge of a molecular cloud (Hughes et al. 1989). But there are additional reasons why our computed line ratios might not match the observed emission distribution in detail. The most important reason is that the photoionized precursor region is probably not an equilibrium H II region. Some of the preshock ionizations may not show up as precursor emission because the ions are overrun by the shock before they can recombine. In addition, the shock speed, and therefore the shape of the ionizing spectrum, may change on a faster timescale than the recombination time (Cox 1972). The radiation field emitted by the blast wave propagating through the low-density cavity was presumably much harder, if fainter, in the past. Hard photons can penetrate into the precursor to create an extended, partially ionized zone that may be seen in low-excitation emission such as [S II] (e.g., Maloney, Hollenbach, & Tielens 1996). It is also not known to what extent shocks in the O-rich filaments contribute to the precursor ionizing radiation field. The UV radiation field from the O-rich filaments could dominate over other sources (Sutherland & Dopita 1995b). Furthermore, the short cooling times in the high-Z plasma may result in rapid changes in the ionizing radiation from the O-rich filaments. Finally, there may have been a UV flash from the SN explosion which photoionized an extended region of the surrounding ISM. However, there are regions around the outer rim which strongly suggest the precursor ionization is closely tied to the radiation field produced by the shock waves in the immediate vicinity.

5. Conclusions

We have presented *HST* WFPC2 narrow-band [O II]$\lambda\lambda$3727, [O III]λ5007 and [S II]$\lambda\lambda$6716, 6731 images of the young, oxygen-rich SNR N132D in the LMC that show detailed structure in the line-emitting filaments comparable to ground-based images of nearby remnants such as Cas A. Our principal results follow:

1. We verify and elaborate on the results of previous morphological studies of N132D, such as Morse et al. (1995) and Sutherland & Dopita (1995a). In particular, our images distinguish oxygen-rich filaments, seen in [O II] and [O III] emission, from normal-abundance QSF-like shocked clouds and diffuse photoionized emission, which emit in all three emission lines. The O-rich filaments show complicated internal structure, ranging from compact knots at the limit of our resolution to finger-like protrusions that appear to be "swept back" along the direction of motion in some filaments. In the shocked QSF-like clouds, the typical knot sizes are $0''.2 - 0''.5$ ($\sim 1.5 - 4 \times 10^{17}$ cm), generally at least partially resolved in our images. By combining our three emission-line images into a "true-color" composite image, we are able to resolve, for the first time, ionization structure within the shocked interstellar clouds and filaments. Our analysis of the fine-scale structure of the QSF-like filaments shows that the [O III] emission is often filamentary, while the [S II] emission arises from compact knots. These characteristics may indicate that the gas fragments as it cools and compresses, either due to dynamical instabilities, as seen in some hydrodynamical simulations of shock/cloud interactions, or due to a chaotic magnetic field that inhibits the compression and reduces the emissivity in some regions of the postshock flow.

2. We compare our *HST* optical emission-line images of N132D to the *ROSAT* HRI soft X-ray image from Hughes (1994). We find that the X-ray emission distribution is closely traced

by compact knots and filaments that emit brightly in [S II]. In other words, the X-rays appear to emanate from shocked circumstellar material and do not appear to come from the O-rich ejecta. The limb-brightened outer rim of the X-ray shell aligns remarkably precisely along the inner edge of the diffuse optical rim seen primarily in [O III] emission. As previously suggested by Morse et al. (1995), we interpret this diffuse emission as arising from photoionized gas ahead of the main blast wave.

3. We used the MAPPINGS II code to model the emission from the X-ray producing main blast wave as an ~ 800 km s^{-1} shock moving into a circumstellar medium of density $N_0 \approx 3$ cm^{-3}. The cooling time of the shock was limited to $\tau \sim 2500$ yr, the maximum shock age based on dynamical estimates of the SNR lifetime. We were able to obtain a precise match to the slope of the thermal bremsstrahlung and many of the emission lines in the single-temperature NEI model spectrum of Hwang et al. (1993) which was fit to the *Einstein* spectral data. The preshock ISM density of $N_0 \approx 3$ cm^{-3} inferred from our shock model agrees with the preshock density estimated from the [O III]λ5007 surface brightness in the diffuse outer rim.

4. Using ram pressure balance to scale the preshock density and shock velocity, we used shock models to deduce that the fully radiative shocked clumps and filaments observed in the remnant probably have shock velocities $\lesssim 300$ km s^{-1}, consistent with the kinematics of the QSF-like clouds observed in ground-based observations.

5. We used MAPPINGS II to model the [O III]/[S II] emission-line ratios in the photoionized outer rim as a function of distance ahead of the main blast wave. The radiation field produced by fast shocks in the remnant was used as the ionizing source. According to our models, the flux of ionizing radiation from the ~ 800 km s^{-1} main blast wave is not sufficient to generate the observed optical emission from the outer rim precursor. In particular, the ionization parameter in the truncated 800 km s^{-1} shock model spectrum is a factor of ~ 2 too low to produce the observed high ionization of the precursor near the shock front. An extra source of EUV photons appears necessary to achieve the observed ionization of the preshock gas. We estimate that EUV photons produced in slower shocks moving into QSF-type clouds around the outer rim can probably contribute enough ionizing photons to achieve the observed ionization. Radiative shocks moving through the O-rich filaments may also be an important source of EUV photons. Summing together the ionizing radiation produced by the main blast wave with the radiation produced by slower shocks associated with the cool, [S II]-emitting clouds along the outer rim achieves approximately the right ionization in the precursor near the shock front. However, in order to generate the observed trend in the [O III]/[S II] line ratio, the density must increase as a function of distance from the shock front. A gradually increasing precursor density may be consistent with the blast wave encountering the molecular cloud mapped by Hughes et al. (1989). Alternatively, the rapidly decreasing ionization of the precursor may indicate that the precursor does not represent an equilibrium H II region, as assumed in our models.

In our next paper (Blair et al. 1996) we will present UV/optical spectroscopy of one QSF-type cloud along the outer rim and two positions in the O-rich ejecta obtained with the FOS aboard *HST*. We hope to determine the ionization mechanism acting in the O-rich filaments based on the observed emission-line ratios and estimate reliable abundances in the supernova ejecta for comparison with models for nucleosynthesis in massive stars. We have also obtained WFPC2 images of the [O III]λ5007 emission from the oxygen-rich SNR E0102.2–7219 in the SMC, and should shortly observe the ejecta in this remnant with FOS. In a later paper we will compare the E0102.2–7219 observations to the results we have obtained for N132D.

Support for this work was provided by NASA grants GO-5365.01-93A to the Johns Hopkins University, GO-5365.02-93A to the Space Telescope Science Institute, and GO-06052.03-94A to the University of Colorado. JPH acknowledges the support of NASA through grant NAG5-2156 to the CfA. We thank the staff of the STScI photolab for their assistance in producing the color prints for this paper. We are grateful to Rob Fesen and Dick McCray for fruitful discussions, and to the referee for providing helpful comments.

Table 1. N132D Observing Log

Filter	Mean λ (Å)	Effective width (Å)	$t_{\rm exp}$ (s)	Spectral coverage
F375N	3737	27	2×2000	[O II]$\lambda\lambda$3727
F502N	5013	27	2×1800	[O III]λ5007
F547M	5476	483	2×400	continuum
F673N	6732	47	2×1800	[S II]$\lambda\lambda$6724

REFERENCES

Bertelli, G., Bressan, A., Chiosi, C., Mateo, M., & Wood, P. R. 1993, ApJ, 412, 160

Blair, W. P., et al., 1996, in preparation

Blair, W. P., Raymond, J. C., Danziger, J., & Matteucci, F. 1989, ApJ, 338, 812

Blair, W. P., Raymond, J. C., & Long, K. S. 1994, ApJ, 423, 334

Blanco, V. M., et al. 1987, ApJ, 320, 589

Burrows, A., Hayes, J., & Fryxell, B. A. 1995, ApJ, 450, 830

Cardelli, J. A., Clayton, G. C., & Mathis, J. S. 1989, ApJ, 345, 245

Chevalier, R. A., & Kirshner, R. P. 1979, ApJ, 233, 154

Cox, D. P. 1972, ApJ, 178, 143

Danziger, I. J., & Dennefeld, M. 1976, ApJ, 207, 394

David, L. P., Harnden, F. R., Jr., Kearns, K. E., & Zombeck, M. V. 1992, The *ROSAT* High Resolution Imager (HRI) (Technical Rep., US *ROSAT* Science Data Center/SAO)

Dickel, J. R., & Milne, D. K. 1994, Proc. Astron. Soc. Australia, 11, 99

Dickel, J. R., & Milne, D. K. 1995, AJ, 109, 200

Dopita, M. A., Binette, L., & Tuohy, I. R. 1984, ApJ, 282, 142

Dopita, M. A., & Sutherland, R. S. 1995, ApJ, 455, 468

Dopita, M. A., & Sutherland, R. S. 1996, ApJS, 102, 161

Dopita, M. A., & Tuohy, I. R. 1984, ApJ, 282, 135

Hartigan, P., Morse, J. A., & Raymond, J. C. 1994, ApJ, 436, 125

Heathcote, S., Morse, J. A., Hartigan, P., Reipurth, B., Schwartz, R. D., Bally, J., & Stone, J. M. 1996, AJ, submitted

Holtzman, J. A., et al. 1995a, PASP, 107, 156

Holtzman, J. A., et al. 1995b, PASP, 107, 1065

Hughes, J. P. 1987, ApJ, 314, 103

Hughes, J. P. 1994, in The Soft X-ray Cosmos, AIP Conf. Proc. 313, edited by E. M. Schlegel & R. Petre (AIP, New York), p. 144

Hughes, J. P., Bronfman, L., & Nyman, L. 1989, in Supernovae, edited by S. E. Woosley (Springer, New York), p. 679

Hwang, U., Hughes, J. P., Canizares, C. R., & Markert, T. H. 1993, ApJ, 414, 219 (HHCM)

Klein, R. I., McKee, C. F., & Colella, P. 1994, ApJ, 420, 213

Lasker, B. M. 1978, ApJ, 223, 109

Lasker, B. M. 1980, ApJ, 237, 765

Lasker, B. M., & Golimowski, D. A. 1991, ApJ, 371, 568

Long, K. S., Helfand, D. J., & Grabelsky, D. A. 1981, ApJ, 248, 925

Maloney, P., Hollenbach, D. J., & Tielens, A. G. G. M. 1996, ApJ, in press

Mathewson, D. S., Ford, V. L., Dopita, M. A., Tuohy, I. R., Long, K. S., & Helfand, D. J. 1983, ApJS, 51, 345

McKee, C. F., & Cowie, L. 1975, ApJ, 195, 715

Mendoza, C. 1983, in IAU Symp. 103, Planetary Nebulae, ed. D. R. Flower (Dordrecht: Reidel), 143

Morse, J. A., Raymond, J. C., & Wilson, A. S. 1996, PASP, in press

Morse, J. A., Winkler, P. F., & Kirshner, R. P. 1995, AJ, 109, 2104 (MWK)

Osterbrock, D. E. 1989, Astrophysics of Gaseous Nebulae and Active Galactic Nuclei (Mill Valley, University Science Books)

Panagia, N., Gilmozzi, R., Machetto, F., Adorf, H. M., & Kirshner, R. P. 1991, ApJ, 380, L23

Reed, J. E., Hester, J. J., Fabian, A. C., & Winkler, P. F. 1995, ApJ, 440, 706

Raymond, J. C. 1979, ApJS, 39, 1

Raymond, J. C., & Curiel, S. 1995, RevMexAASC, vol. 3, p. 199

Russell, S. C., & Dopita, M. A. 1990, ApJS, 74, 93

Sedov, L. I. 1959, *Similarity and Dimensional Methods in Mechanics* (New York: Academic Press)

Shull, J. M., & McKee, C. F. 1979, ApJ, 227, 131

Shull, P. 1983, ApJ, 275, 611

Sutherland, R. S., Bicknell, G. V., & Dopita, M. A. 1993, ApJ, 414, 510

Sutherland, R. S., & Dopita, M. A. 1993, ApJS, 88, 253

Sutherland, R. S., & Dopita, M. A. 1995a, ApJ, 439, 365 (SD95a)

Sutherland, R. S., & Dopita, M. A. 1995b, ApJ, 439, 381

Tsvetanov, Z. I., Morse, J. A., Wilson, A. S., & Cecil, G. 1996, ApJ, 458, 172

Vancura, O., Raymond, J. C., Dwek, E., Blair, W. P., Long, K. S., & Foster, S. 1994, ApJ, 431, 188

Westerlund, B. E., & Mathewson, D. S. 1966, MNRAS, 131, 371

Figure Captions

This preprint was prepared with the AAS LaTeX macros v3.0.

Fig. 1: Ground-based continuum-subtracted [O III]λ5007 image of N132D, taken from the data presented by MWK. North is to the top and east is to the left. The oxygen-rich filaments are color-coded to show their relative Doppler shifts and are labeled R1, R2, and B1 - B4 (see MWK for additional details). The underlying gray-scale shows the distribution of low-velocity [O III] emission emanating from shocked interstellar clouds (such as "Lasker's Bowl" and the west complex) and the photoionized outer rim. Superposed on the image is the orientation of the WFPC2 field of view.

Fig. 2: Final WFPC2 image mosaics of N132D after full reduction and continuum subtraction. The *HST* data show all of the WF3 chip and portions of WF2, WF4, and PC1. These images are displayed with logarithmic scaling to show both bright and faint structures. (a) The F502N ([O III] λ5007) image; (b) the F673N ([S II] $\lambda\lambda$6724) image; (c) the F375N ([O II] $\lambda\lambda$3727) image; (d) the F547M (continuum) image, which was scaled and subtracted from the emission-line frames (some of the brightest normal-abundance, QSF-type filaments are faintly visible in the continuum image because weak emission from the lines [Fe II]λ5159, [N I]$\lambda\lambda$5200, and [Fe II]$\lambda\lambda$5262, 5272 were included in the filter bandpass); and, for later comparison, (e) the aligned *ROSAT* HRI image (see Hughes 1994) in gray-scale format (see text for details). The boxes in Fig. 2a correspond to the regions enlarged in later figures. The scale is indicated by the vertical bar at upper right, and north is tipped counterclockwise by ~12° as shown. East is to the left.

Fig. 3: A color composite image of the WFPC2 data from a portion of WF3. F502N data ([O III]) are shown in green, F375N ([O II]) data are shown in blue, and F673N ([S II]) data are shown in red. Regions of O-rich material appear as mainly turquoise or blue (combination of [O II] and [O III]). Regions dominated by shocked normal-abundance circumstellar material are pinkish (combination of [O II] and [S II]) or white (bright in all three emission lines). Portions of the diffuse outer halo, dominated by [O III] emission, are visible as a faint green glow in the top-central part of the image. Although some regions are affected by bandpass effects, the large-scale chemical fractionation is quite evident.

Fig. 4: Enlargement of the HST/WFPC2 data near the region called IUE-P1 by Blair et al. (1994). In this and following figures, the [O III] and [S II] data are produced in panels a) and b) with contrast set to show the brightest features (except Fig. 7, which shows [O III] and [O II]). These panels are duplicated in panels c) and d) with the contrast set to show the fainter structures. Linear intensity scaling is used in Figs. 4 - 8. The region shown here is $10'' \times 20''$, which is roughly the size of the IUE aperture, although the alignment is not intended to be exact. The dramatic change in appearance from the [O III] image to the [S II] image is mainly due to abundance differences.

Fig. 5: Enlargement of the [O III] and [S II] HST/WFPC2 data near the region called IUE-P2 by Blair et al. (1994). The region shown is $15'' \times 20''$, and is dominated by normal-abundance material, although large ionization changes between filaments are evident.

Fig. 6: Enlargement of the [O III] and [S II] HST/WFPC2 data on the western limb on N132D. The region shown is 15″ square and shows some of the brightest knots in the region associated with the primary shock front. As in Fig. 5, these regions, dominated by shocked interstellar material, also show large differences in relative intensity from filament to filament, presumably due to variations in ionization.

Fig. 7: Enlargement of the [O III] and [O II] HST/WFPC2 data encompassing the O-rich filament B1 in the SW quadrant of N132D whose velocities should be mainly within the filter bandpasses. No [S II] emission is seen at this position. (The brighter region of O-rich filaments slightly northeast of this filament is actually more affected by bandpass effects.) The region shown is 12″ × 25″. Except for the obviously lower signal-to-noise ratios in the [O II] image, very few differences are seen, indicating relatively uniform ionization conditions throughout these ejecta.

Fig. 8: Enlargement of the [O III] and [S II] HST/WFPC2 data on the southern rim of the remnant, including some bright knots and part of the diffuse outer rim (seen mainly in [O III] at this position). The region shown is 25″ square. Note the very sharp inner edge of the diffuse [O III] emission, which may indicate the position where ambient material is encountered by the main blast wave.

Fig. 9: The central 100 × 100 pixel regions of several autocorrelation images produced by the STSDAS task **autocorr** (see text for details). Each image shows an autocorrelation for offsets up to ±5″ in each direction, with the central pixel corresponding to zero spatial offset. The upper right image shows the [O III] autocorrelation of the O-rich filament B1 sub-field (see Fig. 7). The upper left image shows the strongly peaked autocorrelation of a section of the F547M continuum image corresponding to the B1 filament location. The bottom two images show the [S II] and [O III] autocorrelations of the IUE-P2 sub-field (see Fig. 5). Each image has been normalized to a peak intensity of 1.

Fig. 10: A color montage comparing the [O III] (green), [S II] (red), and *ROSAT* HRI X-ray (blue) emission distributions. Regions bright in both optical lines show as yellow; the O-rich ejecta appear green. The X-rays are confined to the outer rim and some bright filaments which have normal abundances. X-rays do not appear to be emitted by the O-rich ejecta. Note the extremely close relationship between the X-ray shell and the inner edge of diffuse optical emission. The inset enlarges a region on the southwest edge of the outer shell that vividly illustrates the offsets among the various emitting regions discussed in the text. (The seam cutting vertically through the precursor emission is the border between the WF3 and WF2 chips.)

Fig. 11: (*top*) One-dimensional flux tracings of the [O III]λ5007, [S II]$\lambda\lambda$6724, and soft X-ray emission summed over a 3″ swath running perpendicular to the X-ray rim shown in the inset of Fig. 10. (The X-ray flux has been scaled down a factor of $\sim$ 50 for plotting purposes.) The vertical line along 0 arcseconds on the horizontal axis marks the position of the shock front, determined primarily by the position of the sharp inner edge of the [O III] emission. The photoionized precursor and the postshock cooling cloud regions are marked. (*bottom*) The logarithm of the

[O III]λ5007/[S II]$\lambda\lambda$6724 flux ratio as a function of distance from the shock front into the precursor gas. The open squares show the observed ratios of the fluxes from the top plot summed in 1″ bins. The filled squares plot the ratios dereddened according to a standard extinction law with E(B–V)=0.20. The error bars in the upper right corner show the typical uncertainty in the flux ratio measurements ($\sim$ 10%) in the vertical direction, and the bin size in the horizontal direction. The degree of ionization in the precursor gas decreases with distance from the shock front. The five-pointed stars show the predicted ratios of the photoionization model discussed in the text.

Fig. 12: The dotted line traces the single-temperature model fit of Hwang et al. (1993) to the *Einstein* X-ray spectral data. The X-ray flux of the model fit is normalized to an X-ray shell thickness of 1.9×10^{18} cm and a postshock electron density of $N_e \sim 15$ cm^{-3}. The solid line is the MAPPINGS II shock model match to the Hwang et al. X-ray model spectrum, using a shock velocity $V_{\rm sh} = 790$ km s^{-1} and preshock density $N_0 = 3$ cm^{-3}, limited to a cooling time $\tau \sim 2500$ yr. The gray line shows the effective ionizing spectrum used for the precursor photoionization model discussed in the text. This spectrum sums together the emission from the solid line shock model shown, plus a contribution from the radiation field produced by slower shocks at the location of the X-ray rim. The slower shocks do not possess a strong thermal bremsstrahlung component, adding mostly emission lines in the 10–200 eV range.

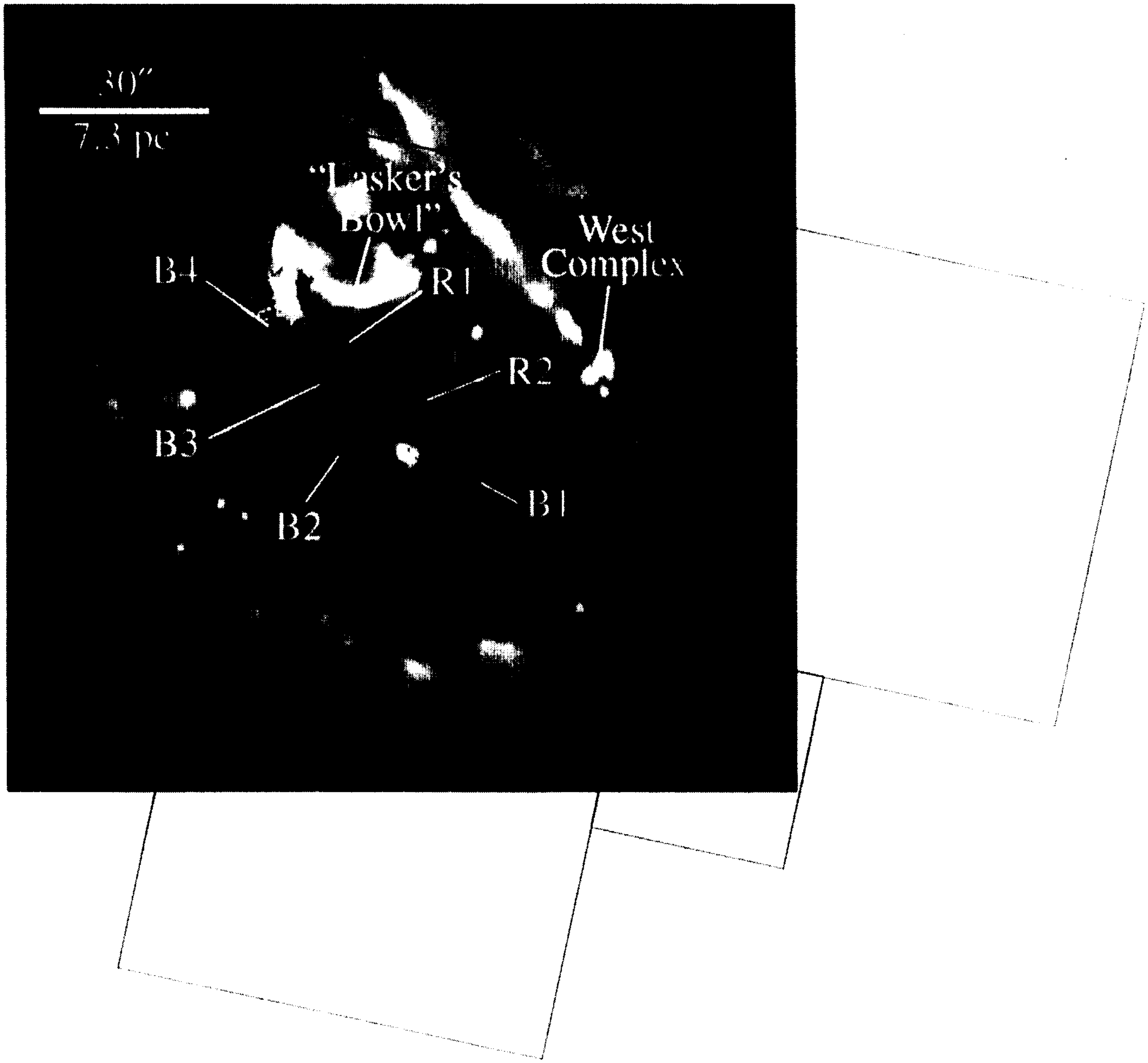
30″
7.3 pc
"Lasker's Bowl"
West Complex
B4
R1
R2
B3
B2
B1

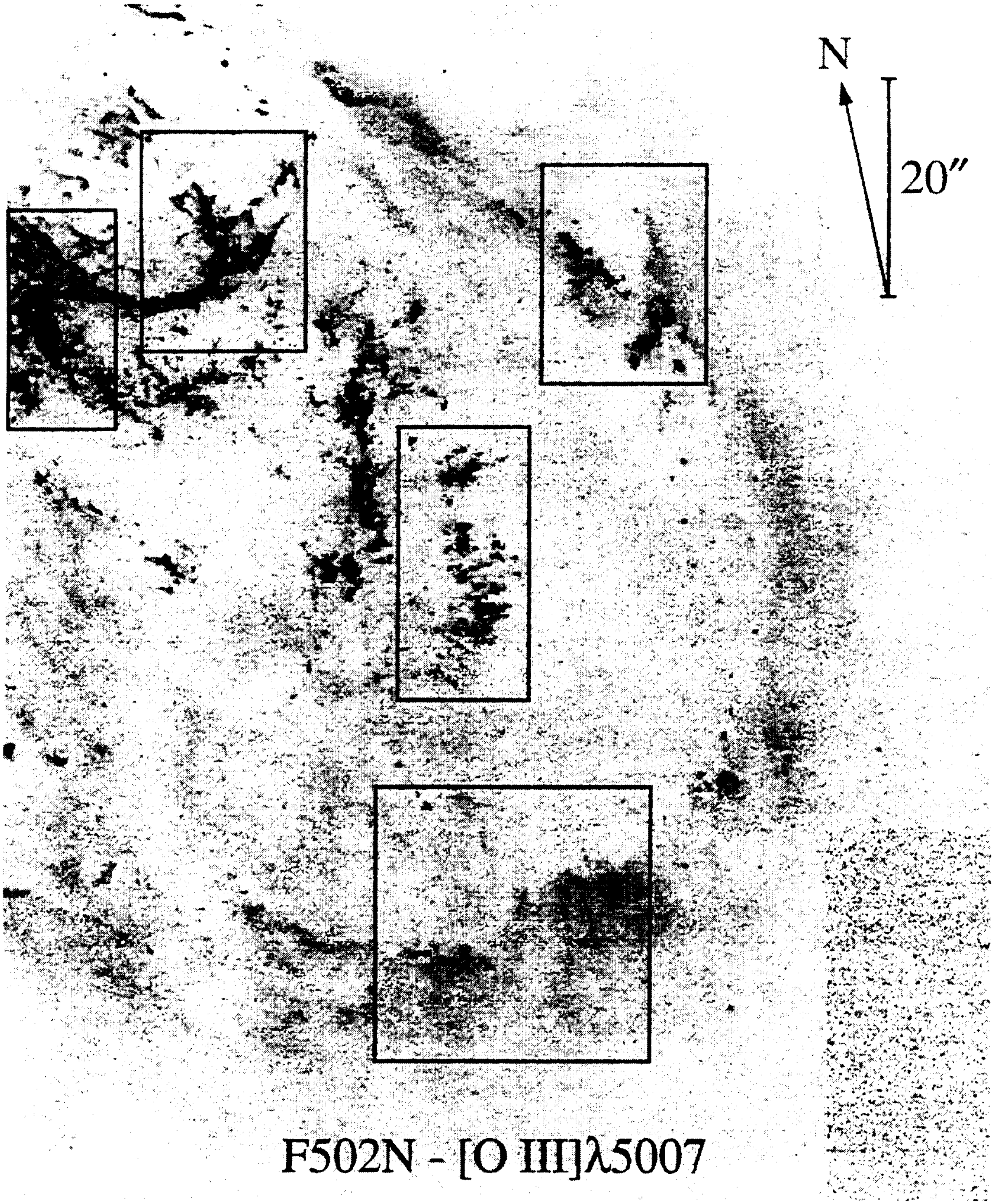
N
20″
F502N - [O III]λ5007

Figure 2a

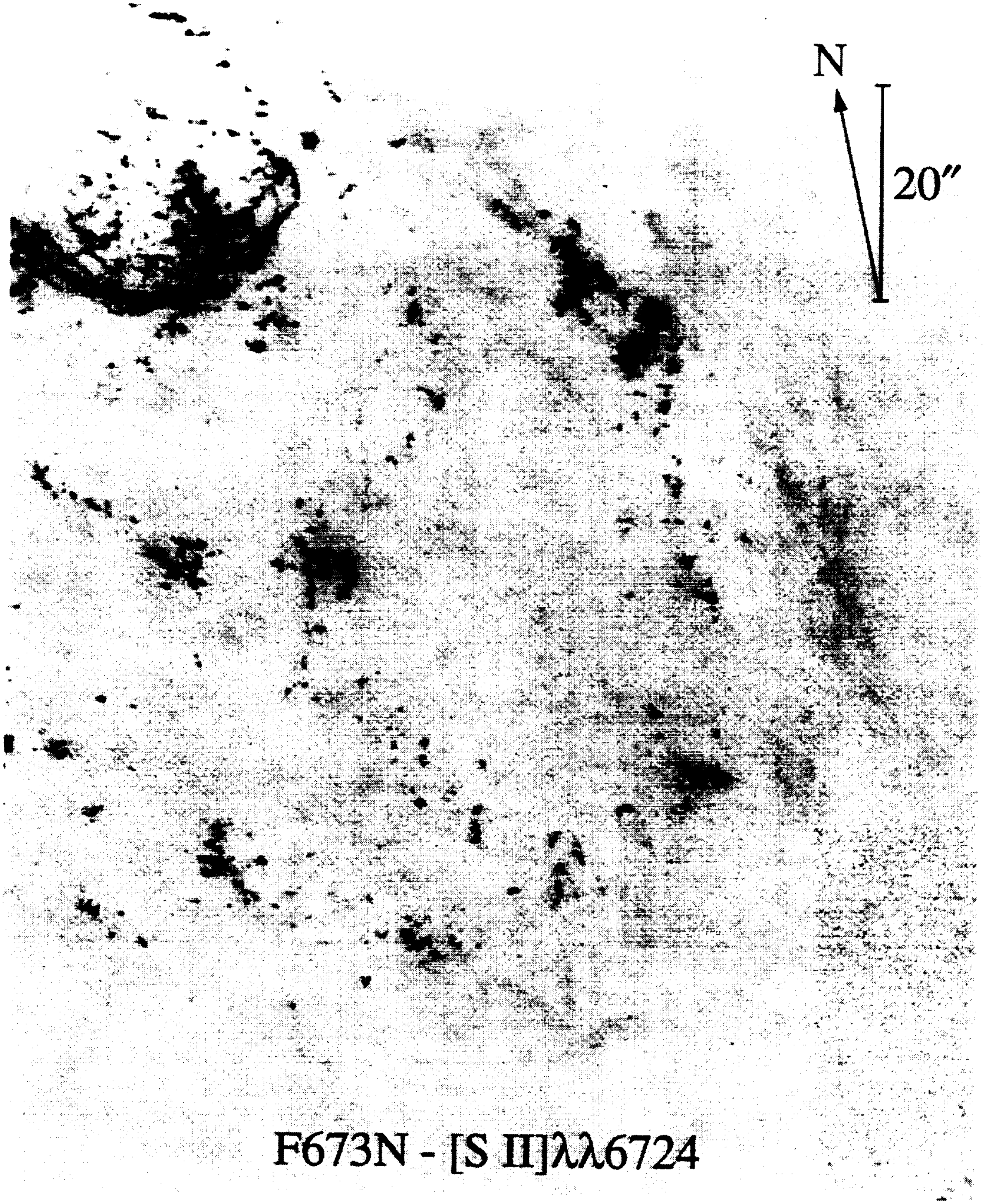
N
20″
F673N - [S II]λλ6724

Figure 2b

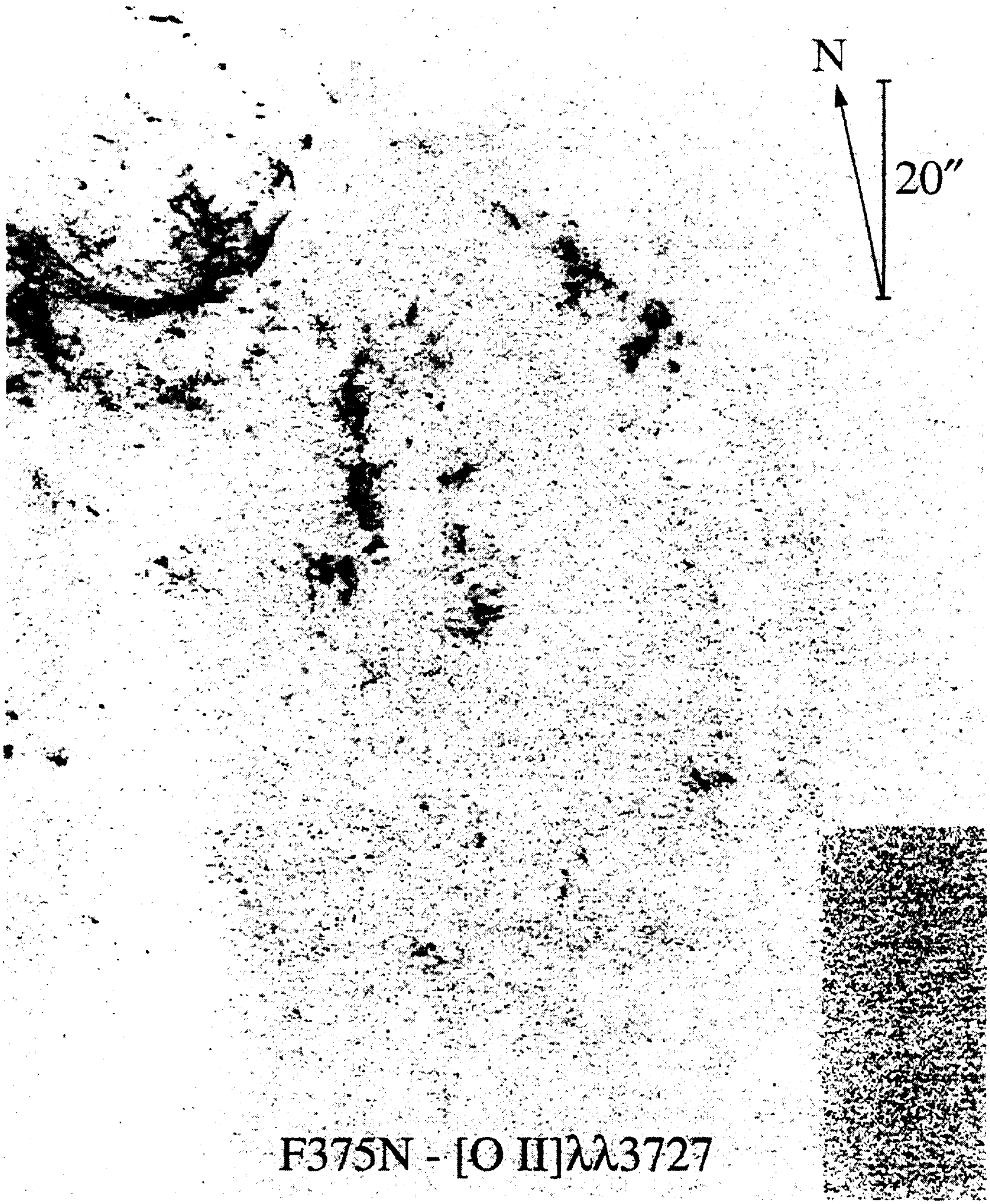
N
20″
F375N - [O II]λλ3727

Figure 2c

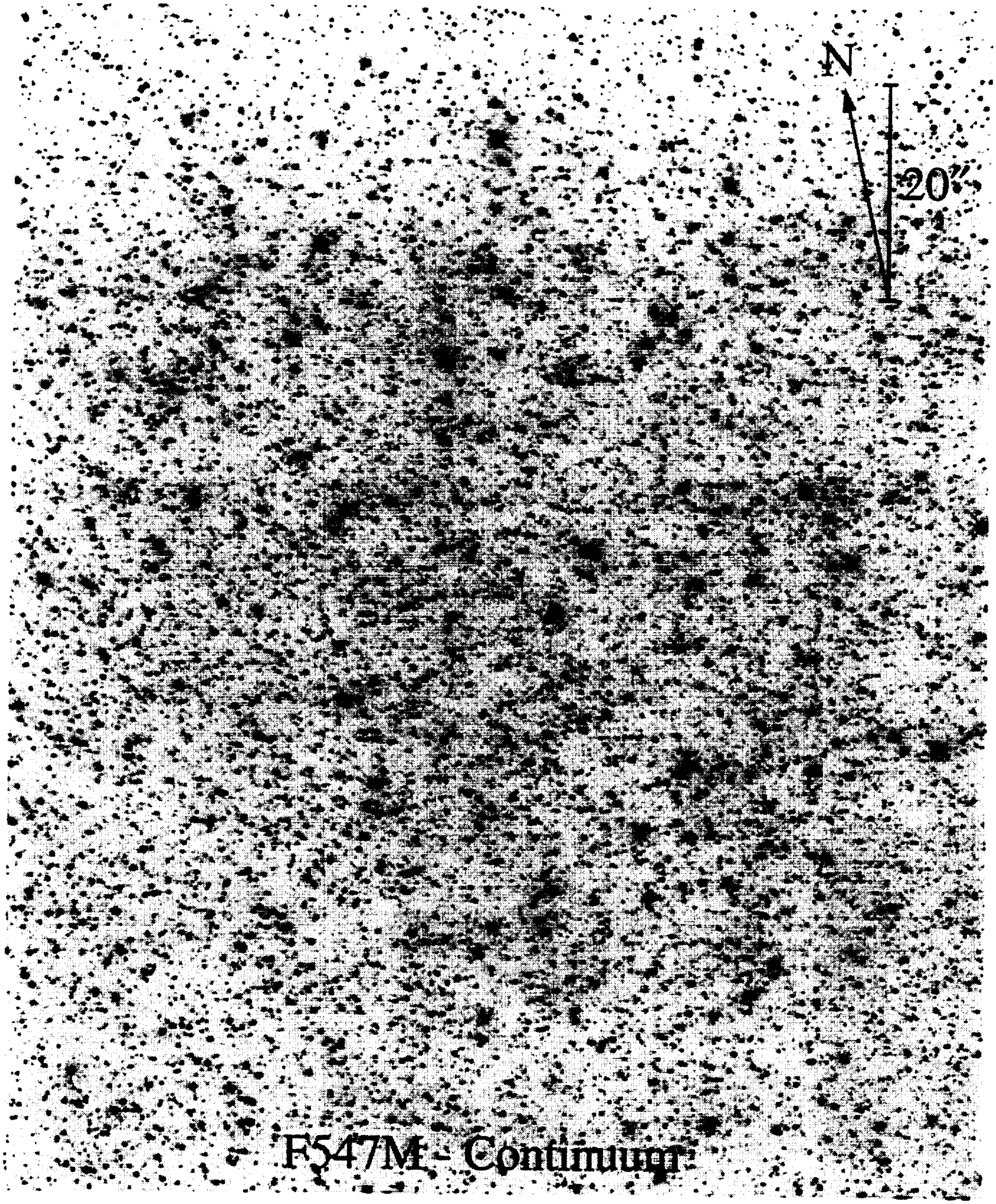
N
20″
F547M - Continuum

Figure 2d

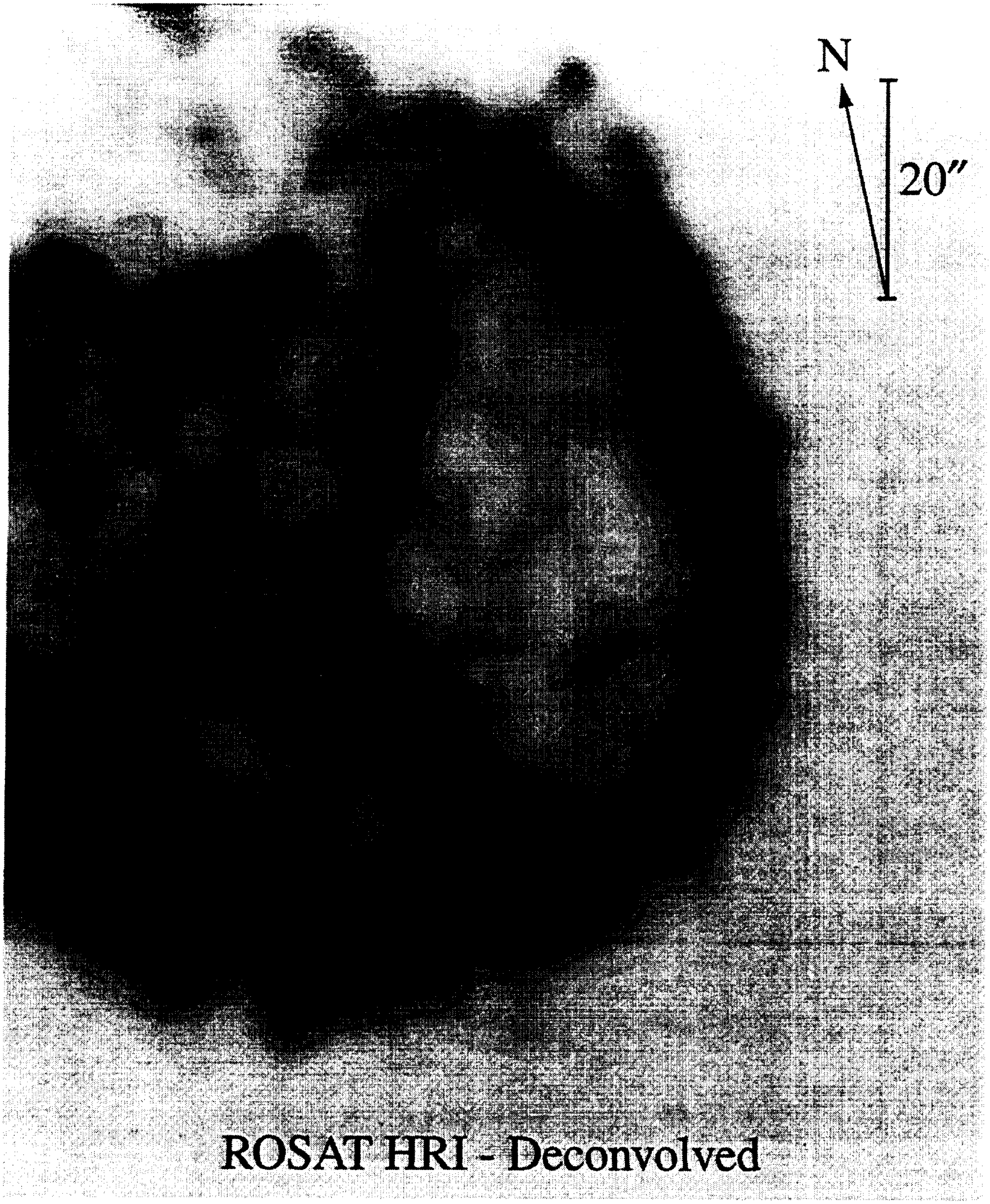
N
20″
ROSAT HRI - Deconvolved

Figure 2e

N132D

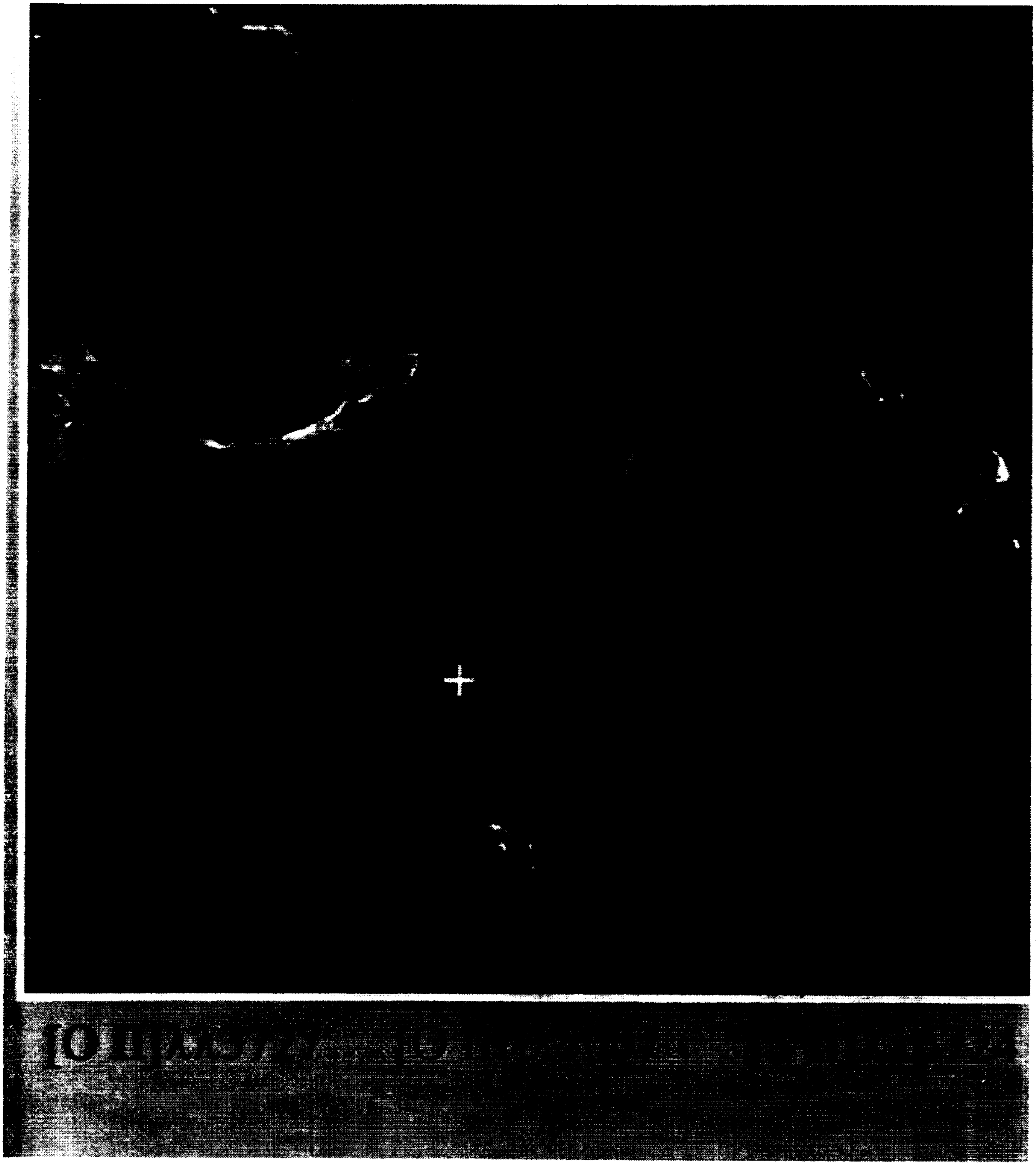

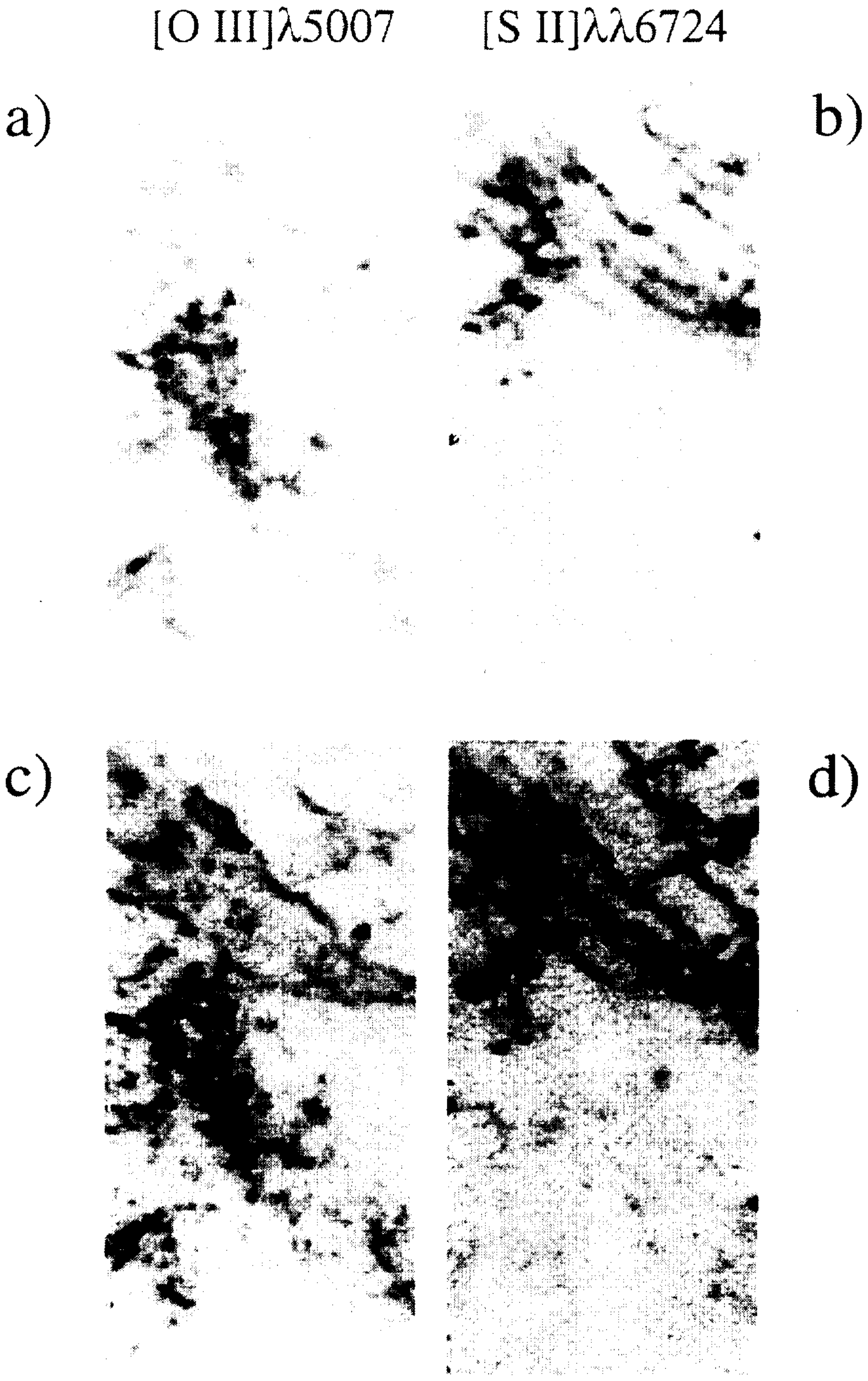
[O III]λ5007
[S II]λλ6724
a)
b)
c)
d)

Figure4

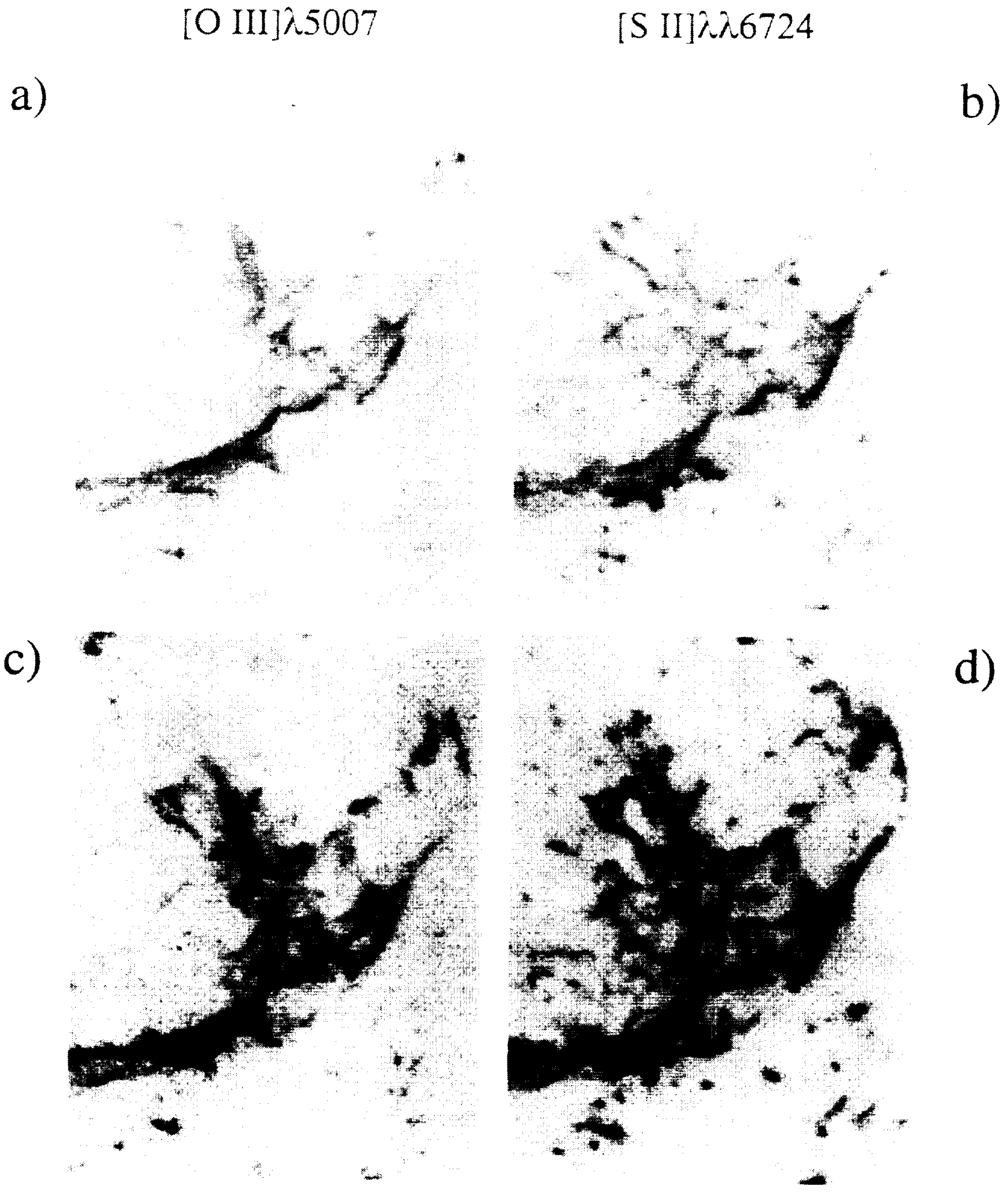
[O III]λ5007
[S II]λλ6724
a)
b)
c)
d)

Figure 5

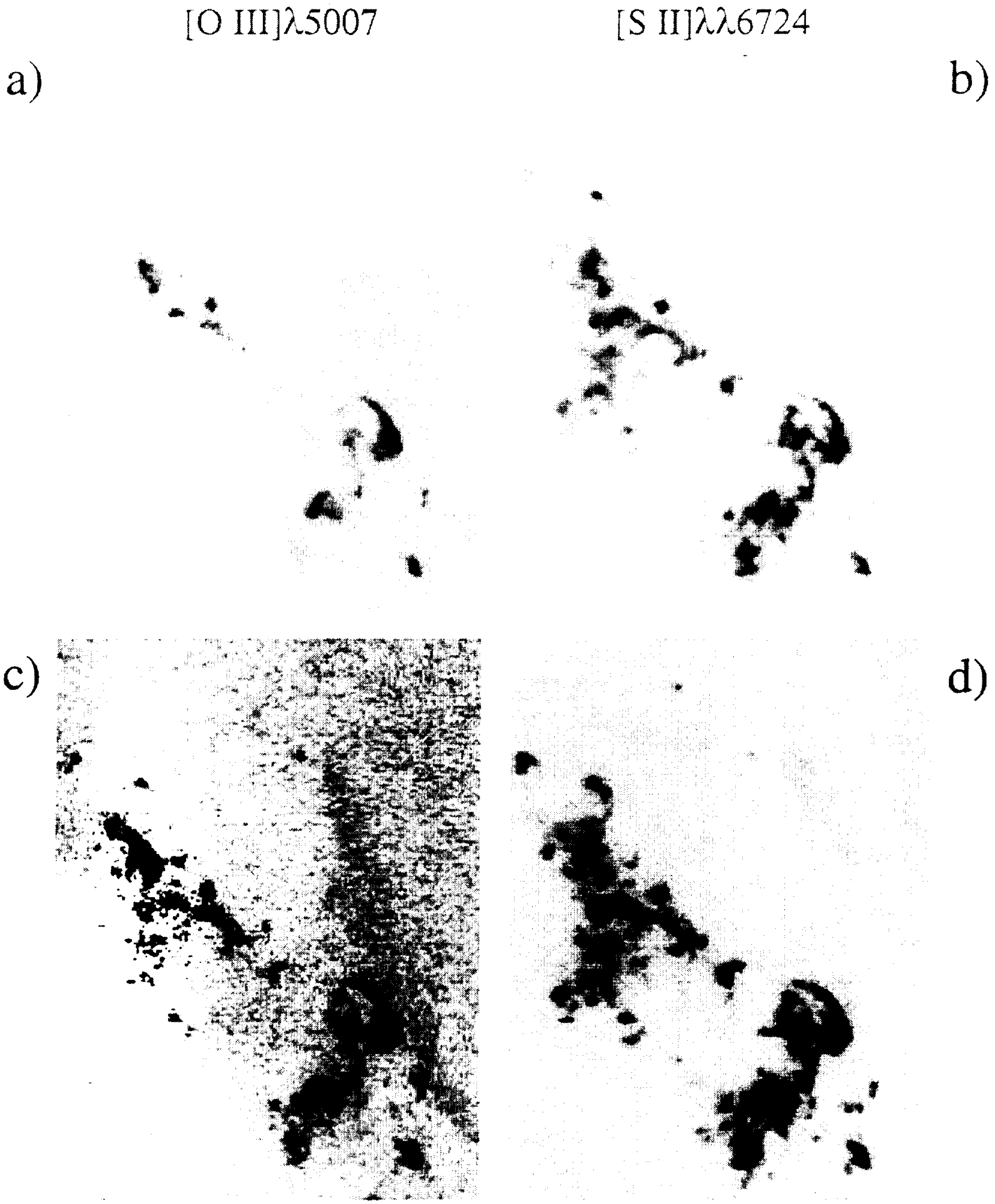
[O III]λ5007
[S II]λλ6724
a)
b)
c)
d)

Figure 6

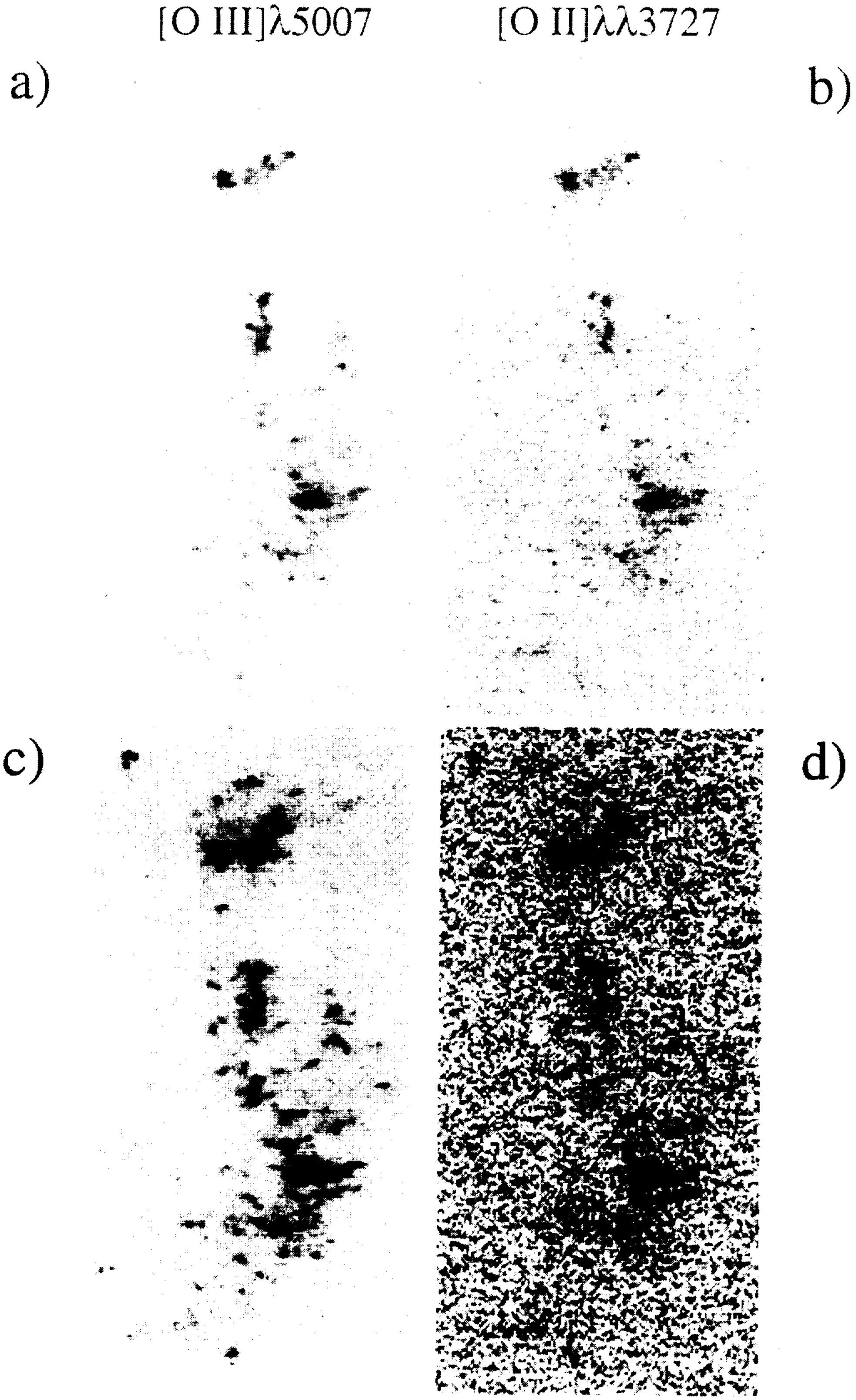
[O III]λ5007
[O II]λλ3727
a)
b)
c)
d)

Figure 7

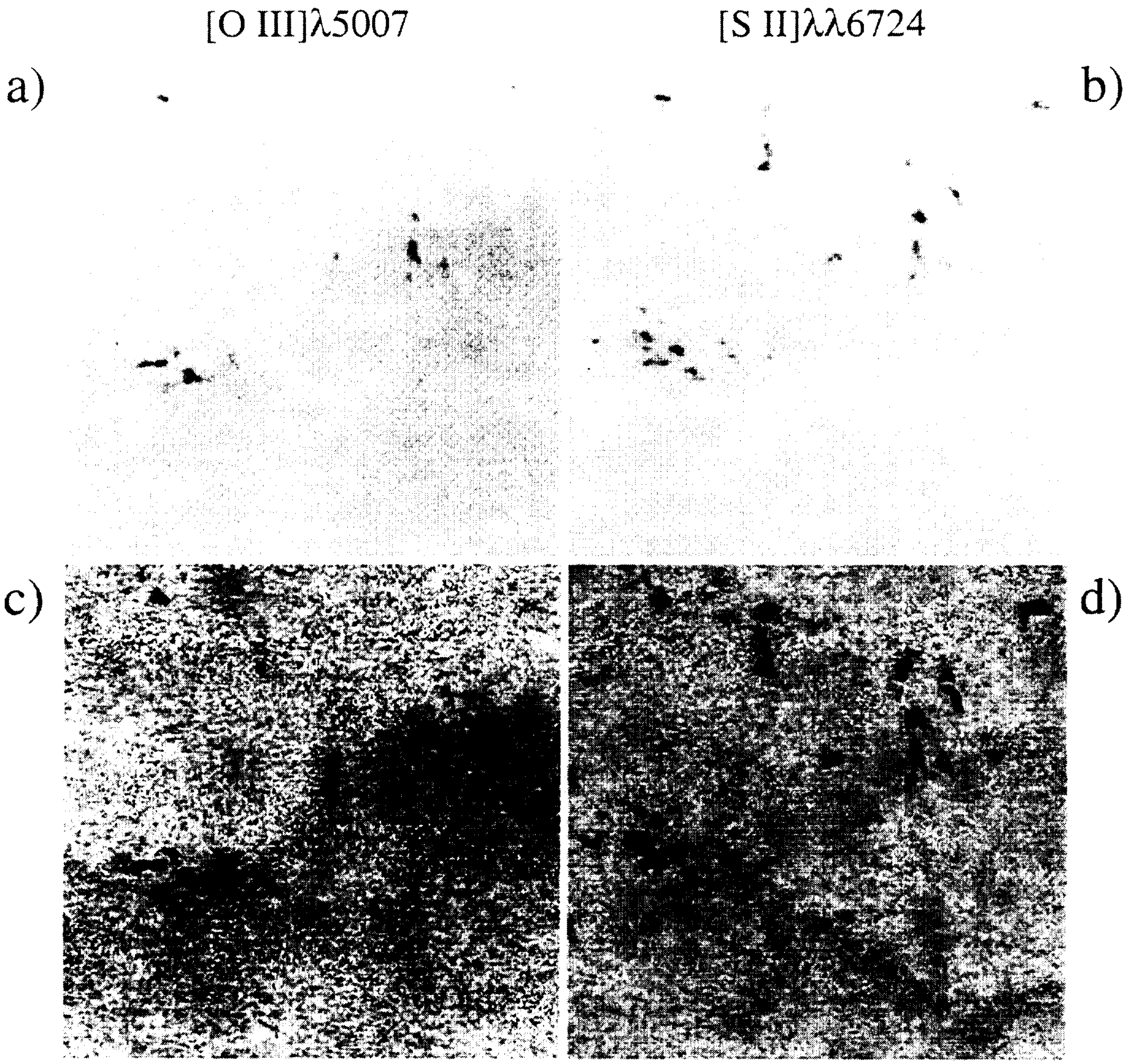
[O III]λ5007
[S II]λλ6724
a)
b)
c)
d)

Figure 8

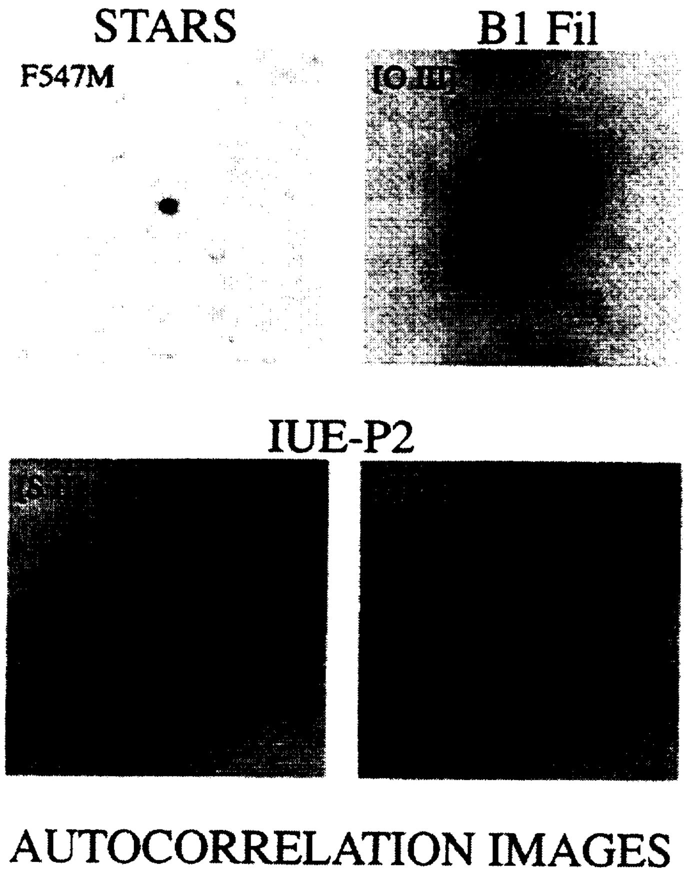
STARS
F547M
B1 Fil
[O III]
IUE-P2
[S II]
AUTOCORRELATION IMAGES

Figure 9

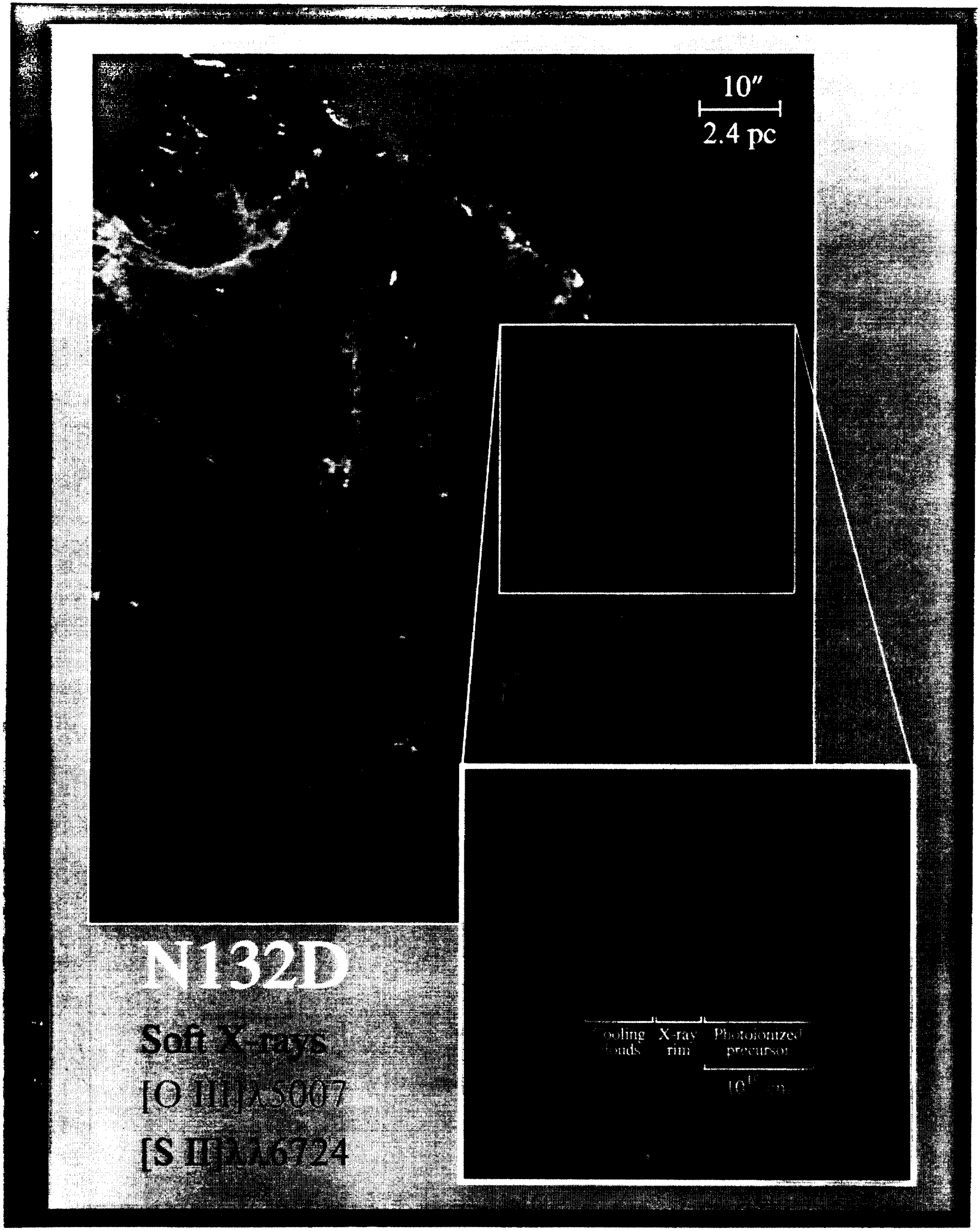
10″
2.4 pc
N132D
Soft X-rays
[O III]λ5007
[S II]λλ6724
Cooling clouds
X-ray rim
Photoionized precursor
10^{17} cm

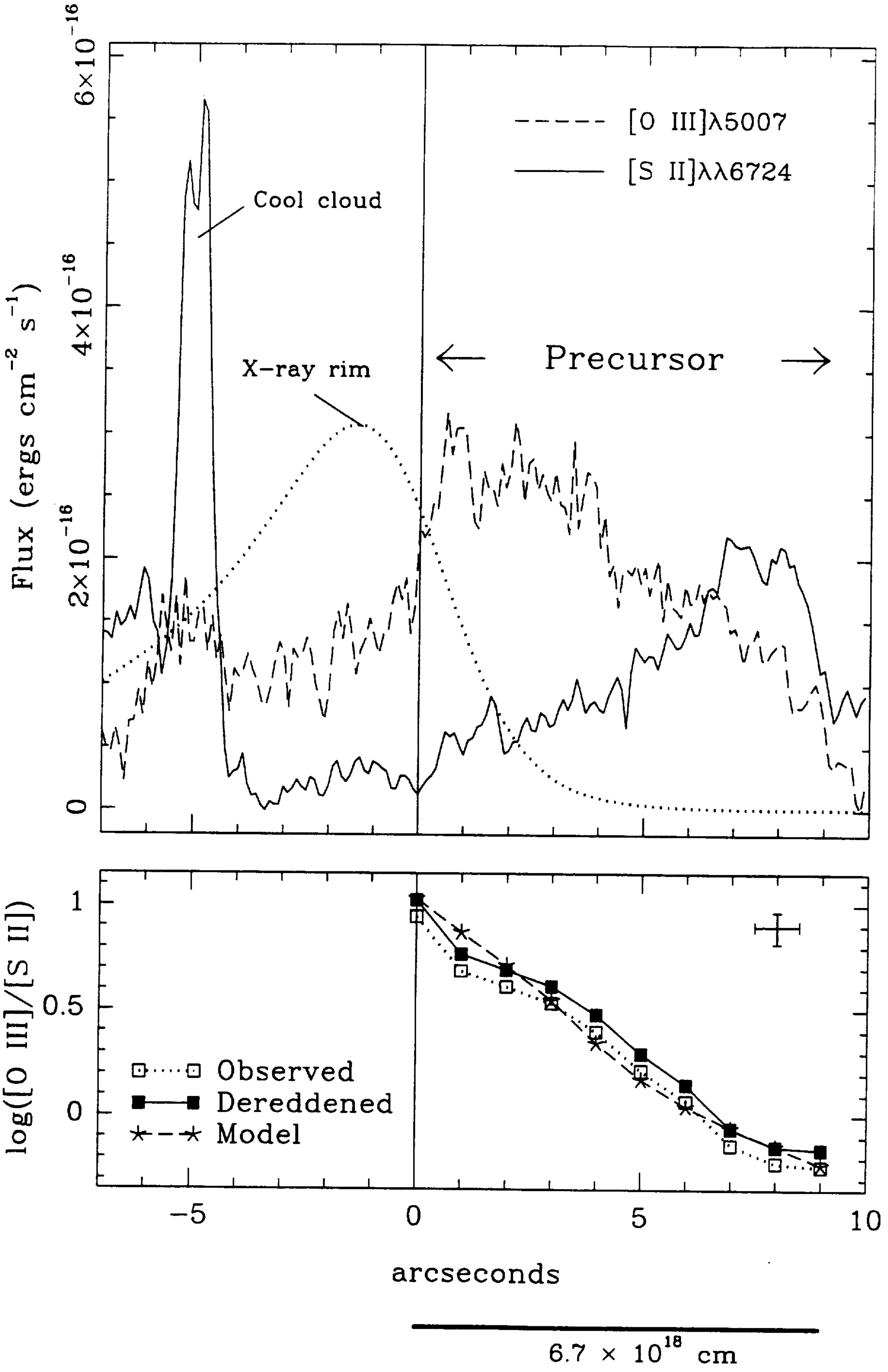
6×10⁻¹⁶
4×10⁻¹⁶
2×10⁻¹⁶
0
Flux (ergs cm⁻² s⁻¹)
[O III]λ5007
[S II]λλ6724
Cool cloud
X-ray rim
Precursor
log([O III]/[S II])
1
0.5
0
Observed
Dereddened
Model
−5
0
5
10
arcseconds
6.7 × 10¹⁸ cm

Figure 11

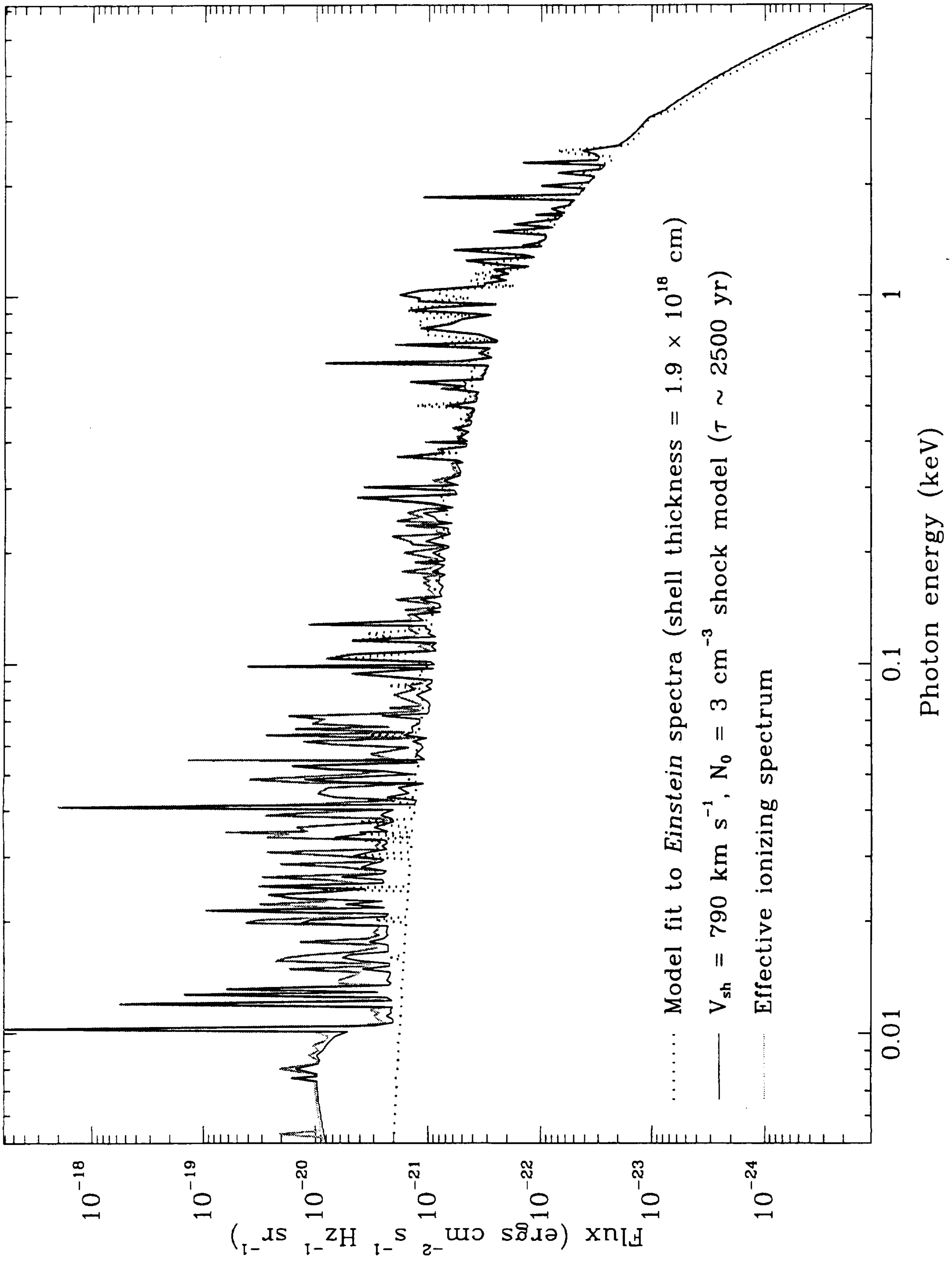
Flux (ergs cm^{-2} s^{-1} Hz^{-1} sr^{-1})
10^{-18}
10^{-19}
10^{-20}
10^{-21}
10^{-22}
10^{-23}
10^{-24}
Photon energy (keV)
0.01
0.1
1
Model fit to *Einstein* spectra (shell thickness = 1.9 × 10^{18} cm)
V_{sh} = 790 km s^{-1}, N_0 = 3 cm^{-3} shock model (τ ~ 2500 yr)
Effective ionizing spectrum

Figure 12

Supernova Remnants Associated with Molecular Clouds in the Large Magellanic Cloud

Kenneth R. Banas[1,2], John P. Hughes[1,3], L. Bronfman[4], and L.-Å. Nyman[5,6]

Subject headings: ISM: individual (N23, N49, N132D) — ISM: molecules — Magellanic Clouds — supernova remnants

Received 13 August 1996; accepted ____________________

---

[1] Harvard-Smithsonian Center for Astrophysics, 60 Garden Street, Cambridge, MA 02138

[2] krb@astro.caltech.edu, California Institute of Technology, Department of Astronomy, 105-24, Pasadena, CA 91125

[3] jph@physics.rutgers.edu, Department of Physics and Astronomy, Rutgers University, P.O. Box 849, Piscataway, NJ 08855-0849

[4] Departamento de Astronomía, Universidad de Chile, Casilla 36-D, Santiago, Chile

[5] Onsala Space Observatory, S-439 92 Onsala, Sweden

[6] SEST, ESO, Casilla 19001, Santiago 19, Chile

ABSTRACT

We used the Swedish-ESO Submillimeter Telescope (SEST) to search for CO emission associated with three supernova remnants (SNRs) in the Large Magellanic Cloud: N49, N132D, and N23. Observations were carried out in the $J = 2 \rightarrow 1$ rotational transition of CO (230.5 GHz) where the half power beamwidth of the SEST is $23''$. Molecular clouds were discovered near N49 and N132D; no CO emission was discovered in the region we mapped near N23. The N49 cloud has a peak line temperature of 0.75 K, spatial scale of ~7 pc and virial mass of $5.5 \times 10^4\, M_\odot$. The N132D cloud is brighter with a peak temperature of 5 K; it is also larger ~22 pc and considerably more massive $3.5 \times 10^5\, M_\odot$. The velocities derived for the clouds near N49 and N132D, +286.0 and +264.0 km s^{-1}, agree well with the previously known velocities of the associated SNRs: +286 km s^{-1} and +268 km s^{-1}, respectively. *ROSAT* X-ray images show that the ambient density into which the remnants are expanding appears to be significantly increased in the direction of the clouds. Taken together these observations indicate a physical association between the remnants and their respective, presumably natal, molecular clouds. The association of N49 and N132D with dense regions of molecular material means that both were likely products of short-lived progenitors that exploded as core-collapse supernovae.

1. Introduction

Stellar evolutionary models predict massive stars will die in supernova explosions near where they were born. It follows that supernova remnants (SNRs) associated with the molecular clouds from which their progenitors were born must have arisen from massive star, core-collapse supernovae. It is further believed that blast waves from supernova acting on dense atomic and molecular gas can initiate star formation as one part in a clearly cyclic process. Therefore the identification and study of SNRs/molecular clouds associations is important to our understanding of the structure and dynamics of the interstellar medium (ISM), the ratio of thermonuclear to core-collapse supernova, the life cycle of stars, the destruction of molecular clouds, and so on.

The Large Magellanic Cloud (LMC) is well suited to the identification and study of SNR and molecular cloud associations. The Cloud is nearby, relatively unobscured, and has been extensively observed at nearly all wavebands. A sizeable number (>30) of supernova remnants have been identified in the LMC from X-ray, optical, and radio measurements (Mathewson et al. 1983, 1984, 1985). Cohen et al. (1988) systematically surveyed the LMC for CO line emission and found a general correspondence between the CO emission and such Population I objects as SNRs and H II regions. However, because of the limited spatial resolution of the survey (12′), a detailed association between individual objects and molecular clouds was not possible. Guided by the results of this survey, we selected three probable SNR/molecular cloud associations for study at considerably higher angular resolution using the Swedish-ESO Submillimeter Telescope (SEST) at La Silla, Chile. The angular resolution of the SEST at 230 GHz, $\sim 20''$, corresponds to a linear size of 4.85 pc for a distance to the LMC of 50 kpc, which we adopt throughout.

The remnants we selected, in addition to being positionally coincident with CO emission from the LMC survey, were required to show evidence for enhanced X-ray and optical emission along part of the rim, which might be indicative of a density gradient in the ambient medium. The best candidates were the SNRs 0525−66.1, 0525−69.6, and 0506−68.0 (Mathewson et al. 1983), which we will refer to henceforth using their Henize (1956) catalog names: N49, N132D, and N23, respectively.

N49 shows the highest optical surface brightness of all LMC SNRs. Its X-ray (and optical) morphology shows a sharp increase in emission along the southeast edge of the remnant (Vancura et al. 1992a). It appears to be embedded within one of the brighter and more massive CO clouds in the LMC (among clouds, that is, that are not in the 30 Doradus region). N132D is the brightest soft X-ray emitting SNR in the LMC (Mathewson et al. 1983) and optically it displays high velocity oxygen-rich material. Consequently it is one of the most frequently studied of LMC remnants. Toward the south, N132D has a nearly circular, very bright limb, which is about three-quarters complete, while the remaining quarter of the remnant appears as a "blow-out" toward the northeast. Hughes (1987) interpreted this structure as a result of the ionizing radiation and stellar wind of the progenitor acting on a medium with a strong gradient in ambient ISM density. The LMC CO survey showed N132D sitting on the northern edge of a relatively modest cloud. N23 has the weakest X-ray emission of the three chosen SNRs. Its morphology is similar to that of N49 and N132D in that it shows an increase in emission along one limb, in this case the eastern one. The remnant sits on the southern boundary of a modest CO cloud.

In the following, we describe our SEST observations, data reduction, and error analysis (§2); give the results on the molecular clouds found near N49 and N132D (§3); discuss these results in the context of what else is known about these remnants (§4); estimate the masses of the newly discovered molecular cloud (§5); and in §6 we summarize. A preliminary report on a subset of the SEST data was given in Hughes, Bronfman, & Nyman (1991).

2. Observations and Analysis Techniques

2.1. Observations

High resolution imaging of three candidate SNR/molecular cloud associations was undertaken with the SEST on La Silla, Chile, on June 18-21, 1989 and again on October 16-19, 1990. The CO $J = 2 \rightarrow 1$ (at 230.5 GHz) observations were done with a linearly polarized Schottky receiver giving a typical system temperature above the atmosphere of 800–1600 K, depending on elevation and weather conditions. At this frequency the beamwidth of the telescope is 23″ (FWHM), considerably better than the 12′ resolution of Cohen et al. (1988), thereby allowing us to resolve finer structure within the molecular clouds near the SNRs. The main beam efficiency of the telescope, η_{mb}, was 0.54 during the 1989 observations, and due to an improvement in the surface accuracy in 1990, the beam efficiency during the October 1990 observations was about 0.70. We quote results in terms of the antenna temperature corrected for beam efficiency, $T_{mb} = T_A^*/\eta$. Spectra were taken with an acousto-optical spectrometer with a bandwidth of 86 MHz, a channel separation of 43 kHz, and a resolution of 80 kHz, which at the observed frequency corresponds to a velocity resolution of 0.1 km s^{-1}. Calibration was done with a standard chopper wheel method, and the intensities are expected to have a precision better than ~10%.

The line emission was mapped on grids spaced uniformly by 20″ starting at the center of each remnant. The extents of the mapped regions were chosen as appropriate to encompass the regions of bright CO emission discovered near the SNRs. For most of the observations the telescope was operated in frequency-switched mode with a throw of 21 MHz (corresponding to a velocity shift of about 27 km s^{-1}), although a subset of positions were observed in position-switched mode as a consistency check and to search for broad velocity wings to the CO emission. We chose the appropriate cloud velocity at which to observe from the data reported by Cohen et al. (1988). The total integration time at each grid position was usually 1800 s, although some shorter exposures were taken near N132D and N23. The system temperature outside the atmosphere was between 800 K and 1000 K during the two days N49 was observed, 1000 K and 1100 K for the two days N23 was observed, and varied from 1000 K to 1600 K for N132D.

2.2. Reduction

The spectrum at each scan position consists of 2000 channels which oversample the velocity resolution of the receiver by about a factor of 2. The frequency-switched data were reduced in the following manner. The spectrum was copied, shifted in velocity by the 21 MHz throw, inverted to correct for the amplitude inversion between the two phases, and then averaged with the original spectrum. The baselines of the frequency-switched data include temporal variations in the sky and instrument, and the folding procedure removes most of these effects. Only the central 45 km s^{-1} is used during the rest of the reduction.

The continuum fitting task in IRAF, noao.onedspec.continuum, was used to fit baselines. Of the several fit parameters available, our analysis showed that the most important were (1) the type of function to fit to the data, (2) its order (generally low to avoid fitting noise), (3) the number of discrepant points to reject, and (4) the velocity range of the data over which to fit.

Several combinations of parameters produced final spectra with very similar quality baseline fits. Nevertheless we were concerned that the baseline fits could introduce a bias in the derived value of the velocity integrated CO brightness temperature, $W_{\rm CO} = \Delta v \sum T_i$, where the summation is over the line profile, T_i is the observed temperature in channel i, and Δv is the velocity width of each channel (which is a constant for our SEST data). The set of parameters that we ultimately used for baseline subtraction were those that gave a zero mean value for $W_{\rm CO}$ in spectra which appeared to have no signal. These line-free scans were at the outer regions of each cloud, where, if there was any signal present, it was too weak to be distinguished from the noise. Since the baselines of all the lines were similar, we are confident that the functions that behaved well in the line region of scans with no signal were also well-behaved in scans with prominent CO line emission.

Line centroids and widths were computed directly from the individual spectra weighting by the observed brightness temperature in each spectral channel. All velocities are given in the local standard of rest (LSR) frame. The $W_{\rm CO}$ velocity integration range was kept the same for all scans of each target. This interval was determined by examining the location and width of the line in the summed ensemble spectrum of the cloud. Although there is some velocity gradient within the clouds, there was not enough to prevent an identical procedure from being followed for all the scans of a single cloud.

The position-switched scans did not need to be folded, but the same baseline fitting procedures and error analyses were used. Lower order polynomial fits were used because the baselines were flatter. These data were used as a check on the frequency-switched scans and to search for broad velocity components in the detected clouds.

2.3. Error Analysis

The primary source of error in $W_{\rm CO}$ is the baseline fitting procedure. We estimated the error in our fits by comparing the values of $W_{\rm CO}$ obtained with two different fitting functions: a polynomial of the n-th order versus one of order n+1. The $W_{\rm CO}$ values derived from these two fits were correlated and fitted by least squares to a linear relation. The root-mean-square (RMS) deviation of the various points from the linear least squares fit provided the error estimate, $\delta_{\rm BL}$, from baseline fitting for an single spectrum.

To quantify the noise in the observations, the antenna temperatures in velocity channels free of emission were examined. When these values were plotted the histogram was Gaussian. We then sorted these values and extracted the temperature values corresponding to the 15.87 and 84.13 percentiles in the list. Half the difference between these values was taken to be the one σ noise estimate per channel. This error, δ_T, was propagated through the derived quantities, $W_{\rm CO}$, line centroids, and widths.

In our error analysis we propagate the temperature noise per channel, δ_T, through to the quantities derived above. In the case of $W_{\rm CO}$, the baseline fitting error ($\delta_{\rm BL}$) is included by direct summation (not root-sum-square) with the noise error $\delta_{W_{\rm CO}} = \sqrt{N}\Delta v \delta_T + \delta_{\rm BL}$, where N is the number of velocity channels over which all summations were done.

3. Analysis and Results

3.1. N49

The CO emission of the cloud near the N49 mapped by SEST is rather weak and various different parameters were used in an effort to get the best baselines. The function that provided the best fits was a third-order Legendre polynomial which rejected no points and fit the regions from +263 to +280 km s^{-1} and again from +292 to +306 km s^{-1}. These regions were chosen so as not to include the line or the effects present from the folding procedure. $W_{\rm CO}$ was calculated for the velocity region of +281 to +291 km s^{-1}, as were the line center and width. A summary of the fit parameters and error analysis is given in Table 1.

To derive values for $W_{\rm CO}$, velocity, and line width for the ensemble cloud, we produced a composite spectrum by averaging the baseline-subtracted scans with individual $W_{\rm CO}$ values that were greater than $3\delta_{W_{\rm CO}}$ in order to include actual signal and avoid unnecessary noise. We plot this in Figure 1a. As described above, the optimum baseline fit was chosen for how well it subtracted the baseline in the line region. However, there remains a small residual baseline outside the line region due to the observational conditions. Table 2 lists the information derived from the averaged spectrum, showing the number of scan positions averaged, the velocity-integrated CO brightness temperature, the velocity centroid, and the root-mean-square velocity width of the line.

The mean $W_{\rm CO}$ of the "zero" scans was 0.09 ± 0.32 K km s^{-1}. This error is comparable to the $\delta_{W_{\rm CO}}$ derived independently using the techniques outlined above. Figure 2 shows the individual spectra in their correct relative positions on the sky.

Two position-switched spectra were taken at the location of the peak CO emission. The derived $W_{\rm CO}$ values, line centroids, and widths were consistent with those from the frequency-switched data. No evidence for a broader component to the line was apparent.

3.2. N132D

The same reduction technique was used for N132D. The function that gave the best baseline fit to the N132D data was a fifth-order Legendre polynomial with no rejection, and fit over the regions from +243 to +256 km s^{-1} and +272 to +286 km s^{-1}. $W_{\rm CO}$ and velocity information were calculated in the region from +257 to +271 km s^{-1}. The velocity window for the line emission was wider here than for N49 because of a significant velocity gradient ($\sim$5 km s^{-1}) across the N132D cloud. The mean $W_{\rm CO}$ of the "zero" scans was -0.070 ± 1.27.

The error analysis for N132D was broken down into two parts, which are listed separately in Table 1. Upon examination of the data, it became obvious that there was much greater noise in the scans taken on October 17 and 19, 1990, which was likely the result of poorer weather conditions. The noise and fit statistics for these days were considered separately from the rest of the data. The total error in $W_{\rm CO}$ (as the sum of the baseline and noise errors) was used in determining which scans were to be averaged to the total cloud spectra. Therefore, by considering the data in two separate sets, only true signal was added because the noisier data had a higher $3\delta_{W_{\rm CO}}$ threshold.

Once again, to derive values of $W_{\rm CO}$, velocity, and line width for the whole cloud, baseline-subtracted spectra with signal greater than $3\delta_{W_{\rm CO}}$ were averaged. Table 2 lists information derived from this spectrum and the spectrum itself is shown in Figure 1b. Figure 3 plots the individual spectra throughout the cloud.

We took some position-switched data at five positions located near the southern X-ray emitting rim of N132D in order to search for a broad component to the line which might indicate interaction between the cloud and N132D. These data were reduced as described above, but with linear baselines. The same velocity ranges as for the frequency-switched data were used for the baseline fits and to calculate the line values. The mean difference in $W_{\rm CO}$ when compared with the frequency-switched scans at the same positions was 0.6 K km $\rm s^{-1}$, within $\delta_{W_{\rm CO}}$. Because the baselines are flatter than the frequency-switched data, it was possible to search for broad velocity components to the main line, as well as other weaker lines over the entire velocity region from +225 to +335 km $\rm s^{-1}$. We began by summing all the position-switched scans to form a high signal-to-noise spectrum. This spectrum was fitted initially with a single Gaussian to quantify the main peak. To check for a broad CO emission line, we then added a broad Gaussian (with a fixed FWHM of 35 km $\rm s^{-1}$) centered on the line region to the main line. The reduction in χ^2 when this broad line was included was not statistically significant. There were also weak lines at +243 and +285 km $\rm s^{-1}$ that also turned out not to be statistically significant. In conclusion, our data provide no evidence for either a broad component to the main line nor for additional lines beyond that seen in the frequency-switched data.

3.3. N23

The frequency-switched scans taken near N23 were reduced with fifth-order Legendre polynomials with no rejection of discrepant points. The baseline was fit from +243 to +274 km s^{-1} and from +286 to +306 km s^{-1}. The position-switched data were reduced with a second order Legendre polynomial baseline subtraction and fit from +225 to +274 km s^{-1} and from +286 to +335 km s^{-1}. Figure 4 shows the spectra taken around the remnant in their positions on the sky.

Although the scan pattern around N23 may appear haphazard, there is an explanation for the apparently odd placement. The position-switched scans (Figure 4), which were carried out first, were arranged in a pattern similar to those for N132D and N49 – centered on the remnant and extending toward the edge where the X-ray emission appears strongest. When no CO emission was found there and, since the observing time was running short, the mapping strategy was changed in an attempt merely to locate the CO emission, which according to the Cohen et al. (1988) map, should have extended generally toward the northwest. Two areas were mapped: a $9\overset{'}{.}3$ long north-south strip of scans and a $2'$ square pattern to the northeast. These spectra were integrated for only 120 s and were taken in frequency-switched mode. None of these scans show significant CO emission, as indicated in Table 3.

3.4. X-ray Images

For comparison with our maps of CO emission, we obtained high resolution X-ray images from the *ROSAT* and *Einstein* archives. N49 was observed by the *ROSAT* high resolution imager (RHRI) for a total live-time corrected exposure of 41972.4 s in several intervals from March 1992 to March 1993 (ROR numbers 400066 and 500172). N132D was observed by the RHRI in February 1991 for 26830.8 s (ROR number 500002). Since the RHRI observations of N23 are not yet publicly available, we used the *Einstein* HRI data instead. The EHRI observed N23 in May 1980 for 15433.3 s.

All images were deconvolved with a small number of iterations of the Lucy-Richardson algorithm using the implementation in IRAF. The resulting X-ray maps are shown in Figures 5, 6, and 7 for N49, N132D, and N23, with the SEST scan positions and contours of $W_{\rm CO}$ emission overlaid. Our X-ray maps of N49 and N132D agree well with those published by Mathewson et al. (1983); however our N23 map shows much less structure than the previously published one, although the overall appearance is similar, since our effective smoothing of the X-ray image is greater than the $2''$ Gaussian sigma used before.

4. Discussion

4.1. N49

The peak X-ray and optical emission from N49 lies along the eastern limb and coincides extremely well with the position of the mapped CO emission (Fig. 5). In addition to the agreement in projected position, the agreement in velocity, or line-of-sight position, is also quite good. N49 shows a narrow emission line in its optical spectrum that arises from the photoionization of unshocked gas at rest with respect to the local environment and preceding the supernova blast wave (Shull 1983, Vancura et al. 1992a). The LSR velocity of this material is $+286\pm1$ km s^{-1} which is in excellent agreement with our integrated cloud velocity of $+286.0\pm0.1$ km s^{-1}.

The prevailing picture of the N49 environment is one of relatively high density with a gradient in the ambient density increasing from NW to SE. Vancura et al. (1992a) estimate the mean preshock density of the intercloud medium surrounding N49 to be 0.9 cm^{-3} based on the observed X-ray emission. They find that the optical emission must arise from much denser regions with a range of preshock densities covering 20 to 940 cm^{-3}. The lack of spectral variations with brightness can be well explained in terms of sheets of optical emission formed as the supernova blast wave encounters a large dense cloud of gas. The molecular cloud that we have discovered provides a natural explanation for this general picture.

N49 lies at the northern edge of a complex infrared emitting region. The closest cataloged IRAS source (from the Leiden–IRAS Magellanic Clouds Infrared Source Catalogues, Schwering & Israel 1990), LI-LMC 1022, lies just north of the CO cloud at a position of 05:25:59.5, −66:07:03 (B1950). Graham et al. (1987) have argued that collisionally-heated dust in the SNR could be the explanation for the IRAS source. We consider it unlikely that this is the entire explanation, since the flux of LI-LMC 1022 (19.5 Jy at 60 μm) corresponds to a luminosity about an order of magnitude larger than the far infrared luminosity of similar sized Galactic remnants where comparative morphology and other considerations make it clear that we are observing heated dust in the SNR (Saken, Fesen, & Shull 1992). In addition, the four times higher gas-to-dust ratio of the LMC (Koornneef 1984) would suggest lower comparative IR fluxes.

It is more likely that the molecular cloud is the origin of the IR emission. Israel et al. (1993) detect CO emission from a large fraction (87%) of a sample of LMC IRAS sources over a wide range of infrared luminosity. Far infrared emission can arise from the heating of dust in a molecular cloud by embedded stars, the general interstellar radiation field, stellar radiation from nearby star clusters, or other sources. Caldwell & Kutner (1996) have studied a number of molecular clouds in the LMC using the ratio of far infrared luminosity

$L_{\rm FIR}$ to the cloud virial mass $M_{\rm V}$ as a measure of star formation activity, assuming that the infrared luminosity arises from embedded young stars. For LI-LMC 1022 we estimate $L_{\rm FIR} \sim 13 \times 10^4\, L_\odot$, while the cloud mass is $M_{\rm V} \sim 5.5 \times 10^4\, M_\odot$ (see below). The derived ratio $\sim$2 $L_\odot/M_\odot$ is very near the average of the LMC clouds studied by Caldwell & Kutner.

The remnant N49 is itself a strong source of optical, UV, and X-radiation of which Lyα and the O VI λ1035 doublet are the principal sources of flux. Our estimate of N49's intrinsic Lyα luminosity, 2.1×10^{38} ergs s^{-1}, is based on a two-photon continuum flux of 2.3×10^{-10} ergs cm^{-2} s^{-1} (Vancura et al. 1992a) and a value of 3 for the ratio of Lyα to two-photon continuum, as expected from models of planar shocks over a broad range in velocity (Hartigan, Raymond, & Hartmann 1987). We estimate the O VI λ1035 luminosity by scaling C IV λ1550 (2.8×10^{37} ergs s^{-1}) by a factor 4 (Vancura et al. 1992b). Together with the X-ray luminosity of 1.9×10^{37} ergs s^{-1}, this yields a total luminosity of hard photons of 3.4×10^{38} ergs s^{-1}. If the molecular cloud intercepts half of these photons and all that luminosity is subsequently re-radiated in the infrared band, then we would expect $L_{\rm FIR} \sim 4 \times 10^4\, L_\odot$, which is potentially a sizeable fraction, about one-third, of that actually seen.

Since there are no other obvious signs of active star formation (cataloged OB associations or H II regions) in the vicinity of N49, heating by the interstellar radiation field may be negligible and an embedded source origin for the remainder of the far IR emission may need to be considered. However, since this region of the LMC is rather complex and the angular resolution of IRAS is modest ($\sim$1$'$), a definitive explanation for the origin of this emission awaits a more comprehensive study of the N49 environment using higher angular resolution IR data.

4.2. N132D

Figure 6 shows the spatial relationship between N132D and the bright CO cloud discovered near it. To complete the association between them, we turn to the photoionization precursor in the quiescent gas upstream of the expanding supernova blast wave that N132D (like N49) displays. Morse, Winkler, & Kirshner (1995) studied this component to the optical emission and found it to display apparently normal LMC abundances and to be spectrally unresolved at a resolution of 30 km s^{-1}. Its LSR velocity of $+268 \pm 7$ km s^{-1} is in excellent agreement with our velocity of $+264.0 \pm 0.1$ km s^{-1} for the cloud. As with N49, this agreement of velocities along with the proximity in projected position implies a definite physical association.

Based on a study of its X-ray morphology, Hughes (1987) proposed that N132D was expanding into a region with a density gradient increasing from northeast to southwest. To explain the X-ray emission, mean preshock densities of 2–3 cm^{-3} were required in the southern (denser) region. Recently Morse et al. (1996) studied the optical photoionization precursor in this area in more detail and derived a preshock density of roughly 3 cm^{-3} from the surface brightness of [O III] λ5007. The presence of a dense molecular cloud toward the south of the remnant provides a general framework for understanding these results. N132D's incomplete morphology (i.e., the lack of emission or "break-out" to the northeast), the fact that the pre-shock ambient density is considerably lower than the densities usually associated with the cores of molecular clouds, and the spatial separation between the bright CO core and the remnant itself, strongly suggest that N132D lies near the northern boundary of its associated molecular cloud. Numerical hydrodynamic simulations of the explosion of a SN near the edge of a molecular cloud (Tenorio-Tagle, Bodenheimer, & Yorke 1985) do bear some similarity to the observed features of N132D. Given the wealth of specific information known about N132D, further numerical work in this area could yield important information on the structure of molecular clouds and their interface with the general ISM.

Morse et al. (1995) first pointed out an apparent association between the CO emission (as published by Hughes et al. 1991) and an H II region about 2′ south of N132D. Figure 8 shows an optical Hα image of both the SNR and H II region overlaid with contours of CO emission from our current analysis. The position and shape of the H II region agree remarkably well with the cloud core. There is also an IRAS source nearby at 5:25:32.3, −69:43:28 (B1950) (LI-LMC 1008, Schwering & Israel 1990) with a flux at 60 μm of 24.8 Jy. The inferred far infrared luminosity $L_{\rm FIR} \sim 16 \times 10^4\, L_\odot$ compared to the virial mass of the cloud (see below) $M_{\rm V} \sim 3.5 \times 10^5\, M_\odot$ yields a ratio $\sim$0.5 $L_\odot/M_\odot$ which is consistent with other LMC clouds (Caldwell & Kutner 1996) and indicates a substantial amount of heating of the cloud. Like N49, N132D has a substantial UV and X-ray flux. Integrating N132D's effective ionizing spectrum (Morse et al. 1996), we estimate the remnant's intrinsic luminosity (including Lyα and harder photons) to be 1.8×10^{38} ergs s^{-1}. Again assuming that half these photons are absorbed and re-radiated by the molecular cloud gives us an estimate of the far infrared luminosity of $\sim 2 \times 10^4\, L_\odot$, which is evidently only about 10% of the observed $L_{\rm FIR}$. Another source of cloud heating is the ionizing flux from the same star (or set of stars) that is exciting the H II region.

There is a velocity shear of about 5 km s^{-1} across the cloud with the peak of the emission increasing from $\sim$263 km s^{-1} in the east to $\sim$268 km s^{-1} in the west (see Fig. 3). In addition to this velocity shear, there are asymmetric wings on the line profiles that extend to higher velocities in the eastern part of the cloud and to lower velocities in the west. These results are qualitatively consistent with simple rotation of the cloud (Dubinski, Narayan, & Phillips 1995). However, we favor a somewhat different interpretation. We believe that there are (predominantly) two clouds at radial velocities of $\sim$263 km s^{-1}

and ~268 km s^{-1}, with intrinsic velocity widths $\sigma \sim 1.8$ km s^{-1}, containing bright dense cores centered near the CO peaks in the east and west of our maps. These cores are each surrounded by lower density material covering larger regions of the sky. The emission we observe at any particular position in the map is a blend of these two components. For example, consider the set of spectra at declination −69:42:22 (corresponding to the fourth row of scan points south of position 0,0 in figure 3). At right ascension 5:25:27 (immediately below position 0,0) and 5:25:23 (one scan position to the west of 0,0) we see emission that is considerably broader and weaker than scans further to the east or west. In these positions, which lie between the brighter cores, we suggest that we are seeing nearly equal contributions from the lower density "halos" of the two separate clouds. Further to the east or west the spectra are dominated by a single component, but the weaker emission from the other cloud remains as an asymmetric wing on the line profile. In any event, our data reveal that this region is quite complex both morphologically and dynamically.

4.3. N23

In general N23 is not as well studied as the previous two remnants. Its X-ray morphology (Fig. 7) is similar to that of N49, showing a brightening toward the east. In this same direction the optical image (Mathewson et al. 1983) also shows a brightened limb and, in addition, there appears to be a cluster of bright stars beyond the supernova shock front. The nearest cataloged IRAS source is some 200″ south of N23. Two other IRAS sources lie 4′ and 5′ west and southwest.

As mentioned above, the remnant sits near the southern boundary of a modest CO cloud (# 9 from Cohen et al.). However as our results on N49 and N132D clearly show, these lower angular resolution data provide only a coarse guide to the existence of molecular gas on sub-arcminute spatial scales. We were unable to map a large region near N23 to a sensitive level (due to limited observation time) and so our null result on the association of a molecular cloud with this remnant must be considered tentative. We point out that our upper limit to CO emission over the region surveyed northeast of the remnant is consistent with the velocity-integrated CO emission from the cloud actually detected near N49. This region would be an interesting one to follow-up with additional SEST observations.

5. Cloud Masses

The mass of a spherical, self-gravitating molecular cloud of radius R in virial equilibrium can be estimated as $M_{\rm V} = 5R\sigma^2/{\rm G}$, where σ is the line width (RMS) of the ensemble cloud spectrum. We determine the effective radii of the clouds from our maps as $R = (A/\pi)^{1/2}$, where the cloud area A is given by $A = N_S\, L^2$. N_S is the number of scans with significant signal averaged in the ensemble spectrum (see Table 1) and L is the spacing between our scans (20$''$ or 4.85 pc at the LMC). The effective cloud radii are 7.2 pc (N49) and 22.9 pc (N132D). For the N49 cloud we derive a virial mass of $M_{\rm V} = 5.5 \times 10^4\, M_\odot$ and for the N132D cloud we find $M_{\rm V} = 3.5 \times 10^5\, M_\odot$.

It is also possible to estimate molecular cloud masses using the empirical relationship between velocity-integrated CO intensity and H_2 column density. A recent redetermination of the ratio between these quantities for the $J = 1 \rightarrow 0$ transition of CO in the Galaxy yields a value $X_G = N_{\rm H_2}/W_{\rm CO(1-0)} = 1.56 \times 10^{20}$ cm^{-2} K^{-1} km^{-1} s (Hunter et al. 1996). For our data on clouds in the LMC, we must correct this factor for (1) the observational fact that LMC molecular clouds are intrinsically less luminous in CO than Galactic clouds of similar mass (due in part to the lower metallicity and the higher gas-to-dust ratio of the LMC), and (2) the intensity ratio between the $J = 2 \rightarrow 1$ and the $J = 1 \rightarrow 0$ transitions of CO. We use the scaling given by Cohen et al. (1988), $X_{\rm LMC} = 6X_{\rm G}$ to account for the first item. Sakamoto et al. (1995), based on a study of molecular clouds in the first quadrant of the

Galaxy, find a value of 0.66 for the mean ratio $W_{\rm CO(2-1)}/W_{\rm CO(1-0)}$, with a variation from 0.5 to 0.8 as a function of Galactocentric distance. This value is in substantial agreement with other recent measures of this ratio, such as that of Chiar et al. (1994), who find a value of 0.85 ± 0.63 from a study of molecular clouds in the Scutum arm of the Galaxy. For clouds in the Chiar et al. study with $M_{\rm V}$ in the range (4.77 – 6.74) $\times 10^4\, M_\odot$ based on the $J = 2 \rightarrow 1$ transition, we find a ratio of 0.58 ± 0.25, which should be the appropriate value to use for the N49 cloud. For clouds with $M_{\rm V}$ in the range (3.50 – 3.91) $\times 10^5\, M_\odot$ and therefore similar to the cloud near N132D, the ratio is slightly higher, 0.82 ± 0.21. Combining these factors, we come up with a relationship of $N_{\rm H_2}/W_{\rm CO(2-1)} = 1.61(1.14) \times 10^{21}$ cm^{-2} K^{-1} km^{-1} s for the N49 (N132D) cloud. The masses we derive (including a correction for He assuming [He]/[H] = 0.085) are $M_{\rm CO} = 9.8 \times 10^3\, M_\odot$ (N49 cloud) and $M_{\rm CO} = 4.0 \times 10^5\, M_\odot$ (N132D cloud).

The giant molecular cloud near N132D shows excellent agreement (within ~15%) between its CO-derived mass and the virial mass. It also represents a significant fraction, roughly 40%, of the total CO mass of the cloud complex near N132D from the lower resolution Cohen et al. (1988) complete survey of the LMC (cloud # 22 in their Table 1). This complex has an estimated mass of $9.5 \times 10^5\, M_\odot$ after including the revised X_G factor from above. The smaller molecular cloud we found near N49 is far from being a major constituent of the corresponding cloud (# 23) in the LMC survey, encompassing less than 0.5% of the total mass. In addition, the SEST cloud appears not to be in virial equilibrium based on the considerable difference between its CO mass and virial mass, the latter being nearly six times larger than the former. The use of this observation as evidence, albeit weak, for a direct interaction between the cloud and N49's blast wave must be tempered by strong caveats about the large uncertainties in these mass estimates. A convincing case for interaction between these SNRs and their associated clouds will require new considerably deeper observations and the discovery of broad molecular emission lines (30–40 km s^{-1})

from the interaction region.

6. Summary

We used the SEST to map the vicinity of three LMC SNRs, N49, N132D, and N23, in the $J = 2 \rightarrow 1$ transition of CO emission and found that:

(1) The SNRs N49 and N132D show spatial relationships with molecular clouds that coincide with increased X-ray and optical emission from the remnants. There is also good agreement between the mean velocity of the ensemble CO emission, $+286.0 \pm 0.1$ km s^{-1} (N49) and $+264.0 \pm 0.1$ km s^{-1} (N132D), and the optically determined velocities of the remnants, $+286 \pm 1$ km s^{-1} (N49, Shull 1983) and $+268 \pm 7$ km s^{-1} (N132D, Morse et al. 1995). The agreement of the SNR and cloud velocities along with the two-dimensional proximity indicate that the two systems are indeed physically associated.

(2) CO and virial equilibrium masses were derived for the two newly discovered molecular clouds. The different mass estimates agree quite well for the N132D cloud and indicate a mass of $\sim 4 \times 10^5\, M_\odot$ which is within the range expected for a giant molecular cloud. Our two mass estimates for the cloud near N49 are internally inconsistent, which may indicate that the cloud is not virialized. The CO mass for this cloud is $9.8 \times 10^3\, M_\odot$ while the virial mass is $5.5 \times 10^4\, M_\odot$. In neither case does the SEST cloud account for the entire emission observed at lower spatial resolution by Cohen et al. (1988) in their complete LMC CO survey. The N49 SEST cloud is indeed a negligible fraction (<0.5%), although the N132D SEST cloud corresponds to about 40% of the total cloud mass observed at lower resolution.

(3) We detected no CO emission from the vicinity of the SNR N23. Since the area mapped was limited, this null result should not be overinterpreted. The X-ray and optical

morphology of N23 and its proximity to CO emission in the Cohen et al. (1988) survey continue to support the presence of dense molecular gas near N23 and further observations with the SEST are warranted.

(4) The association of N49 and N132D with dense molecular clouds supports the picture in which their progenitors were short-lived, hence massive, stars that exploded as core collapse (i.e., Type II or Type Ib) supernovae. This is consistent with other known characteristics of the remnants, such as the presence of high-velocity, oxygen-rich stellar material in N132D, which is the traditional signature of a massive star progenitor. The work we present here has also made clear that the good angular resolution of the SEST provides the essential key for being able to make SNR/molecular cloud associations in the LMC. Discovery of CO emission in the near vicinities of other LMC SNRs with the SEST would allow us to determine the SN type of a larger fraction of the remnant sample in the Cloud and should be pursued.

The Swedish-ESO Submillimeter Telescope, SEST, is operated jointly by ESO and the Swedish National Facility for Radio Astronomy, Onsala Space Observatory at Chalmers University of Technology. This research has made use of data obtained through the High Energy Astrophysics Science Archive Research Center Online Service, provided by the NASA-Goddard Space Flight Center. We thank Jon Morse for providing the Hα image of N132D and the nearby H II region and we acknowledge very useful discussions with Mark Birkinshaw, Tom Dame, and John Raymond. We would also like to thank Kristin Kearns, Kim Dow, and everyone associated with the Smithsonian Astrophysical Observatory Summer Intern Program, which was funded through the National Science Foundation. L.B. acknowledges support by FONDECYT Grant 1950627, República de Chile. Additional financial support for this research was provided by NASA (*ROSAT* Grant NAG5-2156) and

the Smithsonian Institution.

REFERENCES

Caldwell, D. A., & Kutner, M. L. 1996, ApJ, 471, in press

Chiar, J. E., Kutner, M. L., Verter, F., & Leous, J. 1994, ApJ, 431, 658

Cohen, R. S., Dame, T. M., Garay, G., Montani, J., Rubio, M., & Thaddeus, P. 1988, ApJ, 331, L95

Dubinski, J., Narayan, R., & Phillips, T. G. 1995 ApJ, 448, 226

Graham, J. R., Evans, A., Albinson, J. S., Bode, M. F., & Meikle, W. P. S. 1987, ApJ, 319, 126

Henize, K. G. 1956, ApJS, 2, 315

Hartigan, P., Raymond, J. C., & Hartmann, L. 1987, ApJ, 316, 323

Hughes, J. P. 1987, ApJ, 314, 103

Hughes, J. P., Bronfman, L., & Nyman, L. 1991, in Supernovae, ed. S. E. Woosley (New York: Springer-Verlag), p. 679

Hunter, S. D., et al. 1996, ApJ, submitted

Koornneef, J. 1984, in IAU Symp. 108, Structure and Evolution of the Magellanic Clouds, eds. S. van den Bergh & K. S. de Boer (Dordrecht: Reidel), 333

Israel, F. P., et al. 1993, A&A, 276, 25

Mathewson, D. S., Ford, V. L., Dopita, M. A., Tuohy, I. R., Long, K. S., & Helfand, D. J. 1983, ApJS, 51, 345

Mathewson, D. S., Ford, V. L., Dopita, M. A., Tuohy, I. R., Mills, B. Y., & Turtle, A. J. 1984, ApJS, 55, 189

Mathewson, D. S., Ford, V. L., Tuohy, I.R., Mills, B.Y., & Turtle, A.J. 1985, ApJS, 58, 197

Morse, J. A., Winkler, P. F., & Kirshner, R. P. 1995, AJ, 109, 2104

Morse, J. A., Blair, W. P., Dopita, M. A., Hughes, J. P., Kirshner, R P., Long, K. S., Raymond, J. C., Sutherland, R. S., Winkler, P. F. 1996, AJ, 112, 509

Sakamoto, S., Hasegawa, T., Hayashi, M., Handa, T., & Oka, T. 1995, ApJS, 100, 125

Saken, J. M., Fesen, R. A., & Shull, J. M. 1992, ApJS, 81, 715

Schwering, P. B. W., & Israel, F. P. 1990, Atlas and Catalogue of Infrared Sources in the Magellanic Clouds (Dordrecht: Kluwer Academic Publishers)

Shull, P. 1983, ApJ, 275, 611

Tenorio-Tagle, G., Bodenheimer, P., & Yorke, H. W. 1985, A&A, 145, 70

Vancura, O., Blair, W. P., Long, K. S., & Raymond, J. C. 1992a, ApJ, 394, 158

Vancura, O., et al. 1992b, ApJ, 401, 220.

This manuscript was prepared with the AAS LaTeX macros v4.0.

Table 1. Error analysis of CO line emission

Associated SNR	Baseline Fit Region (km s^{-1})	Line Region (km s^{-1})	δ_T (K)	$\sqrt{N}\Delta v \delta_T$ (K km s^{-1})	δ_{BL} (K km s^{-1})
N49	263 – 280,292 – 306	281 – 291	0.13	0.093	0.22
N132D (total)	243 – 256,272 – 286	257 – 271	0.32	0.28	0.37
N132D (high noise)	243 – 256,272 – 286	257 – 271	0.58	0.52	0.52
N132D (low noise)	243 – 256,272 – 286	257 – 271	0.22	0.20	0.18
N23 (pos switched)	225 – 274,286 – 335	275 – 285	0.23	0.17	0.30
N23 (freq switched)	243 – 274,286 – 306	275 – 285	0.70	0.53	1.5

Table 2. CO line emission for molecular clouds near N49 and N132D

Associated SNR	Number of Averaged Spectra	$< W_{\rm CO} >$ (K km s^{-1})	v (km s^{-1})	σ (km s^{-1})
N49	7	1.72±0.12	+286.0±0.1	2.0±0.1
N132D	70	9.95±0.08	+264.0±0.1	2.8±0.1

Table 3. CO line emission near N23 (Scan positions explained in text)

Scan Position	Number of Averaged Scans	$< W_{\rm CO} >$ (K km s^{-1})
East of N23	9	0.01 ± 0.16
Square NE of N23	16	1.58 ± 0.52
Strip North of N23	15	0.25 ± 0.53

Fig. 1.— Ensemble spectra of the molecular clouds near N49 and N132D. Only scans with signal stronger than $3\delta_{W_{\rm CO}}$ are averaged in these spectra. The zero baseline level is shown. The values listed in Table 1 are calculated from these spectra.

Fig. 2.— Spectra of CO $J = 2\rightarrow1$ emission from the molecular cloud near N49. The spectra were observed on a grid spaced $20''$ apart. The center of N49 is marked as position (0,0). The reference lines show the zero baseline level, the line center (+286.0 km s^{-1}) and FWHM (4.65 km s^{-1}) of the ensemble cloud spectra (shown in Figure 1). (North is to the top, east is to the left)

Fig. 3.— Spectra of CO $J = 2\rightarrow1$ emission from the molecular cloud near N132D. The spectra were observed on a grid spaced $20''$ apart. The center of N132D is marked as position (0,0). The reference lines show the zero baseline level, the line center (+264.0 km s^{-1}) and FWHM (6.64 km s^{-1}) of the ensemble cloud spectra (shown in Figure 1). (North is at the left of the page and east is toward the bottom.)

Fig. 4.— Spectra of position-switched CO $J = 2\rightarrow1$ emission near N23. The center of the remnant is marked with (0,0). The spectra were observed on a grid spaced $20''$ apart. Boxed comments show the locations of the southernmost positions of short, frequency-switched scans. (North is at top, east is to the left)

Fig. 5.— *ROSAT* X-ray image of N49 overlaid with velocity integrated CO emission contours. The X-ray contours are at 0.35, 0.87, 1.4, 1.9, 2.4, 3.0, and 3.5 counts s^{-1} arcmin^{-2}. The CO contours are 1.0, 1.3, 1.7, 2.0, 2.3, and 2.7 K km s^{-1}. The grid pattern for the CO observations is shown. Coordinates are in epoch B1950.

Fig. 6.— *ROSAT* X-ray image of N132D overlaid with velocity integrated emission contours. The X-ray contours are at 0.54, 1.1, 1.6, 2.1, 2.7, 3.2, and 3.8 counts s^{-1} arcmin^{-2}. The CO contours are 5.0, 8.3, 11.7, 15.0, 18.3, 21.7, 25.0, 28.3, and 31.7 K km s^{-1}. The grid pattern

for the CO observations is shown. Coordinates are in epoch B1950.

Fig. 7.— *Einstein* X-ray image of N23. The X-ray contours are at 0.023, 0.070, 0.12, 0.16, 0.21, 0.26, and 0.30 counts s^{-1} $arcmin^{-2}$. The grid pattern for the CO observations is shown. Coordinates are in epoch B1950. (Squares are 840 second position-switched scans and triangles are short 120 second frequency-switched scans.)

Fig. 8.— Narrow-band Hα optical image of N132D and a nearby H II region from the Rutgers/CTIO imaging Fabry-Perot spectrometer (Morse et al. 1995) overlaid with contours of molecular emission. Note the strong spatial correlation between the molecular cloud and the H II region. North is at top, east is to the left.

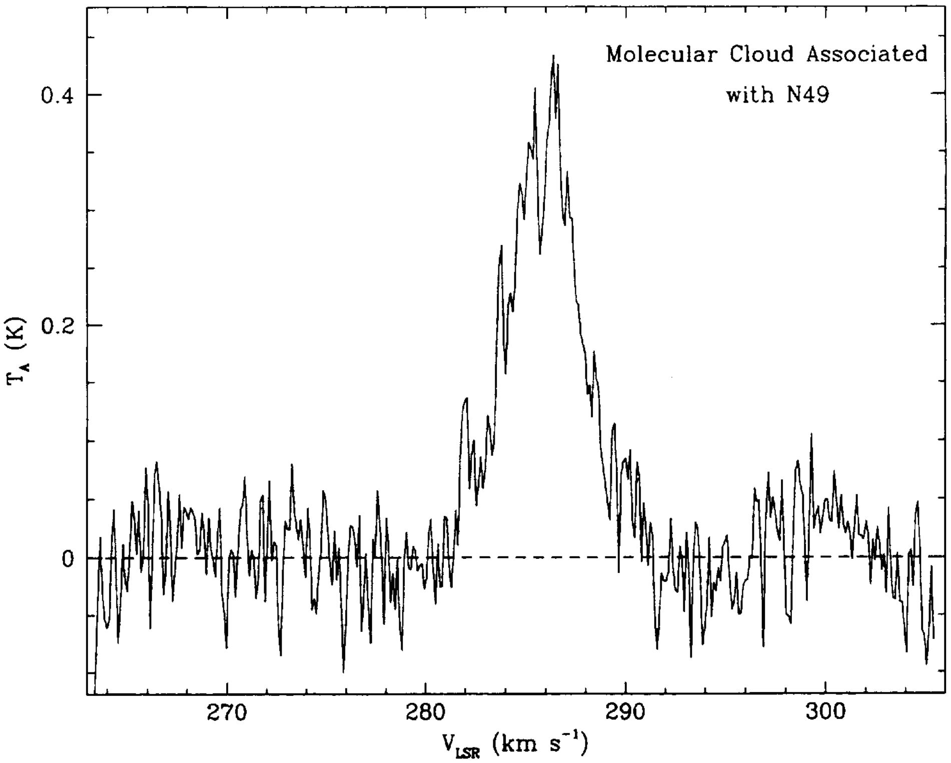
Molecular Cloud Associated
with N49
0.4
0.2
0
T_A (K)
270
280
290
300
V_{LSR} (km s^{-1})

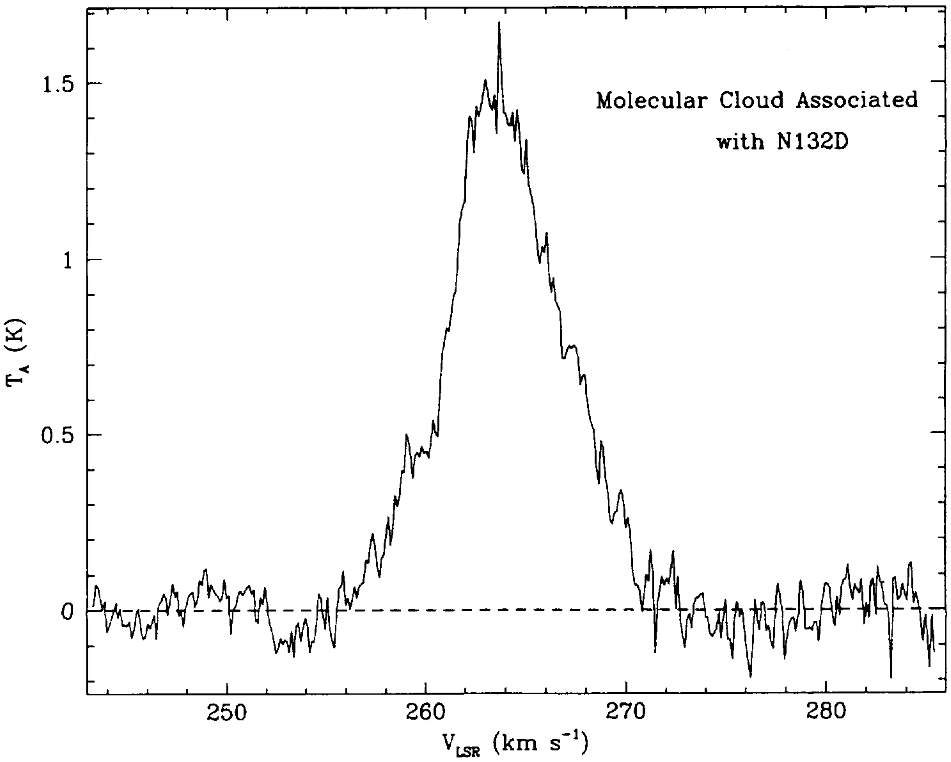
Molecular Cloud Associated
with N132D
1.5
1
0.5
0
T_A (K)
250
260
270
280
V_{LSR} (km s^{-1})

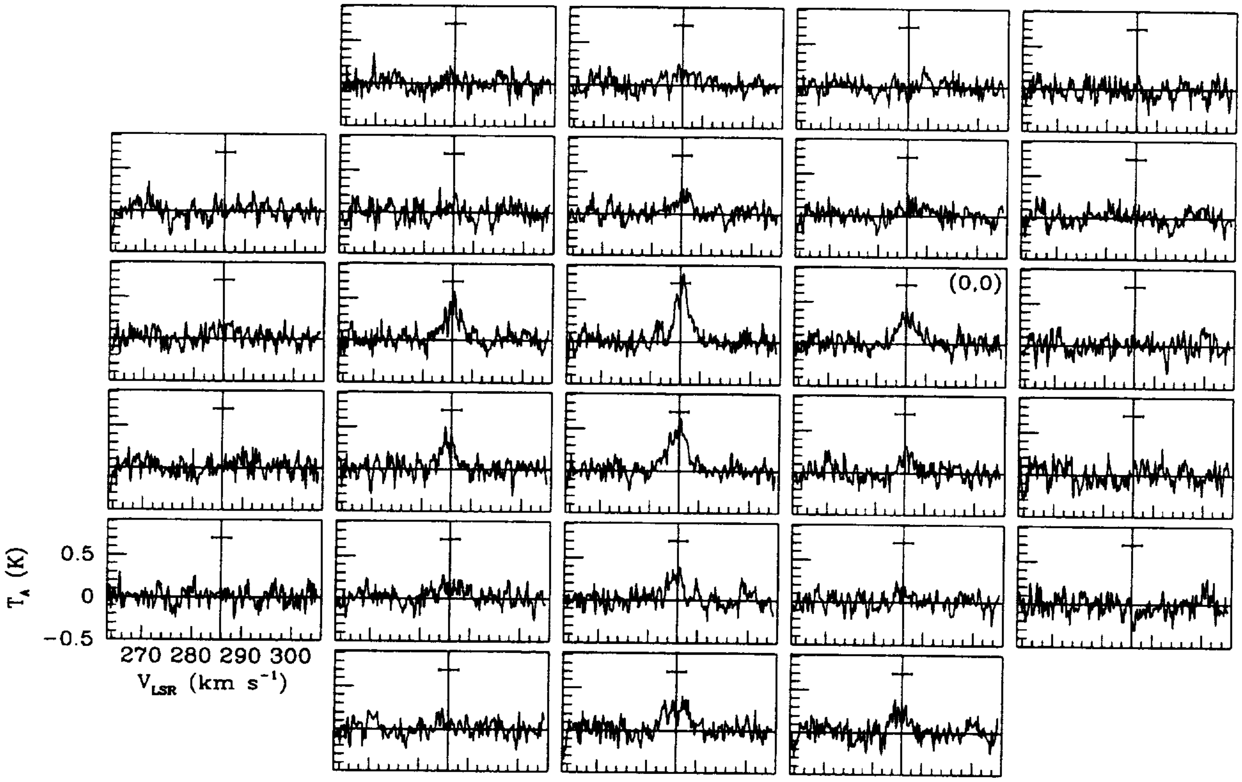
(0,0)
0.5
0
−0.5
T_A (K)
270 280 290 300
V_{LSR} (km s^{-1})

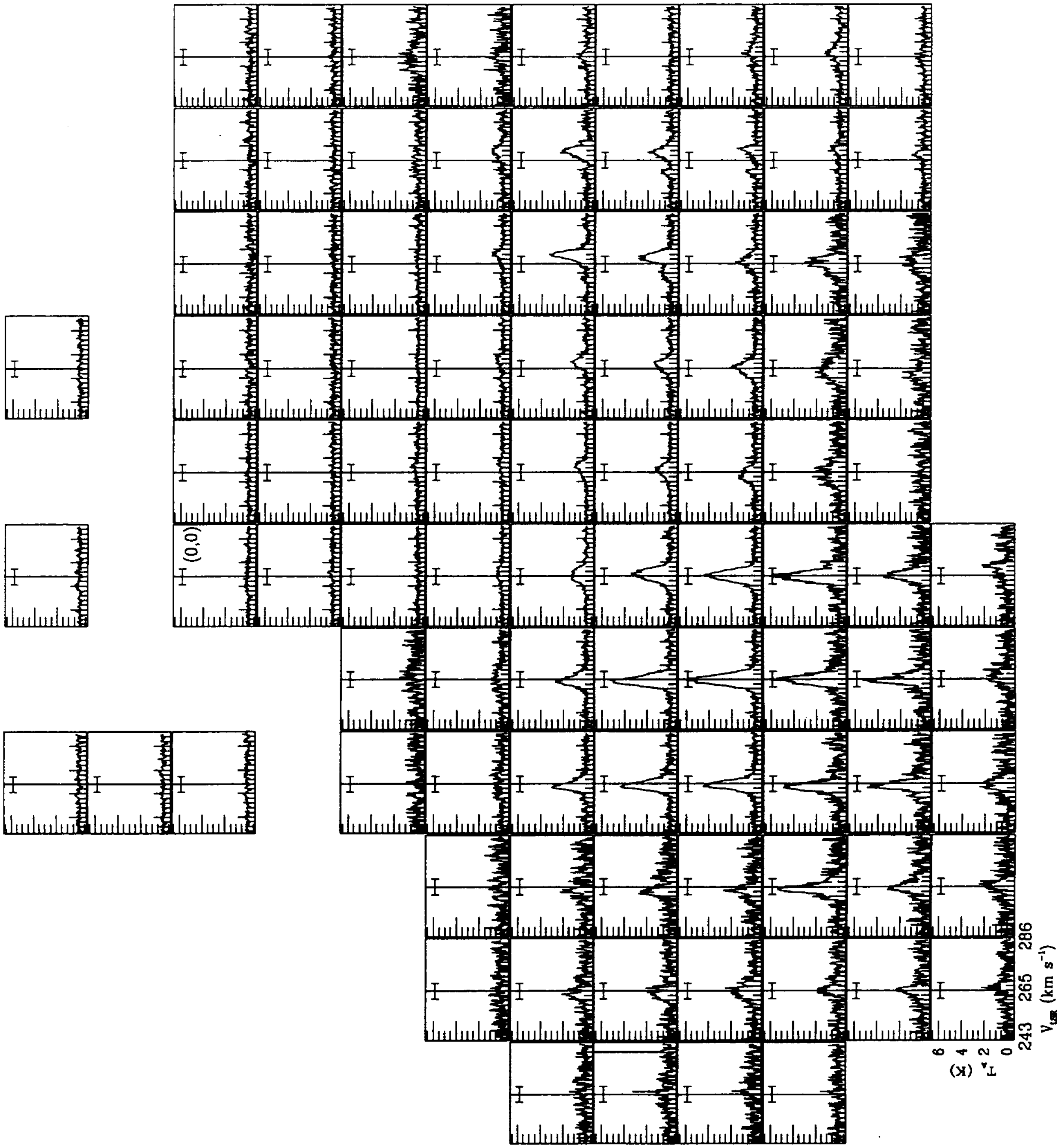
(0,0)
T_A^* (K)
6 4 2 0
243 265 286
V_{LSR} (km s^{-1})

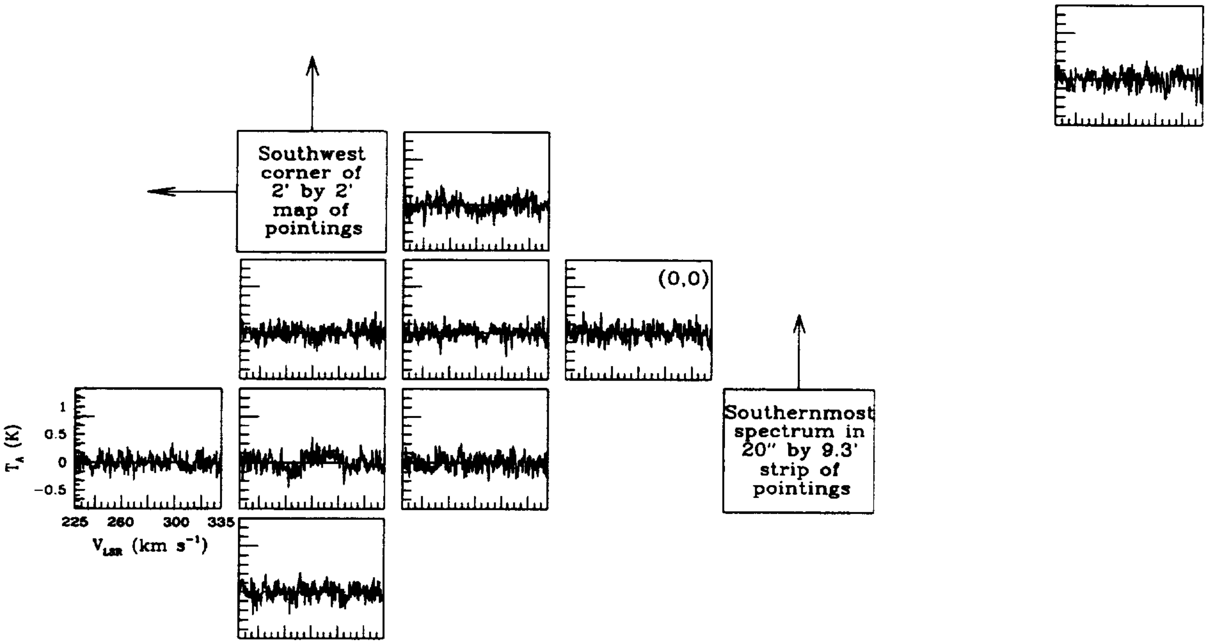
Southwest corner of 2' by 2' map of pointings
(0,0)
Southernmost spectrum in 20" by 9.3' strip of pointings
T_A (K)
1
0.5
0
−0.5
225
260
300
335
V_{LSR} (km s^{-1})

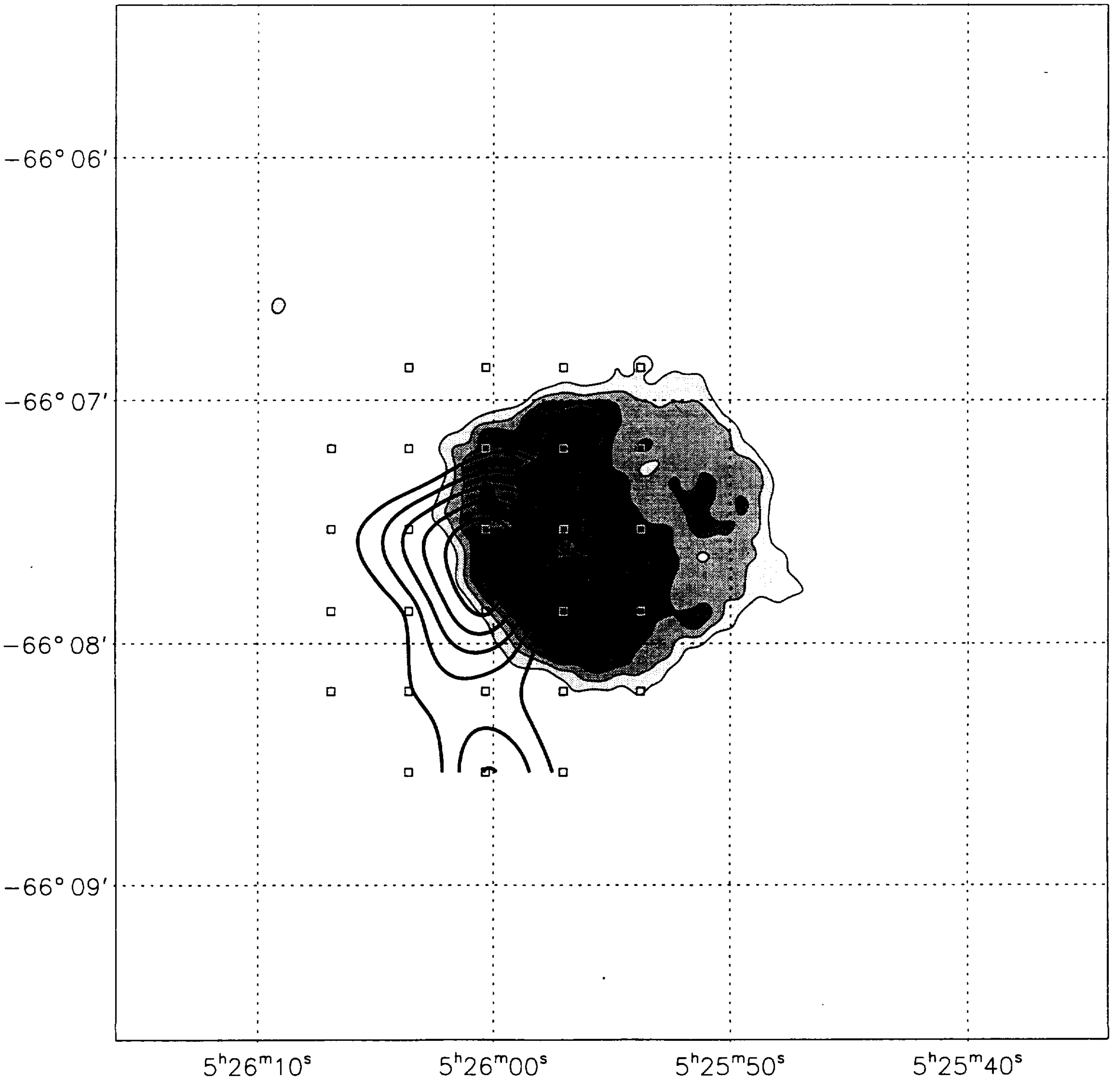
−66° 06′
−66° 07′
−66° 08′
−66° 09′
5h26m10s
5h26m00s
5h25m50s
5h25m40s

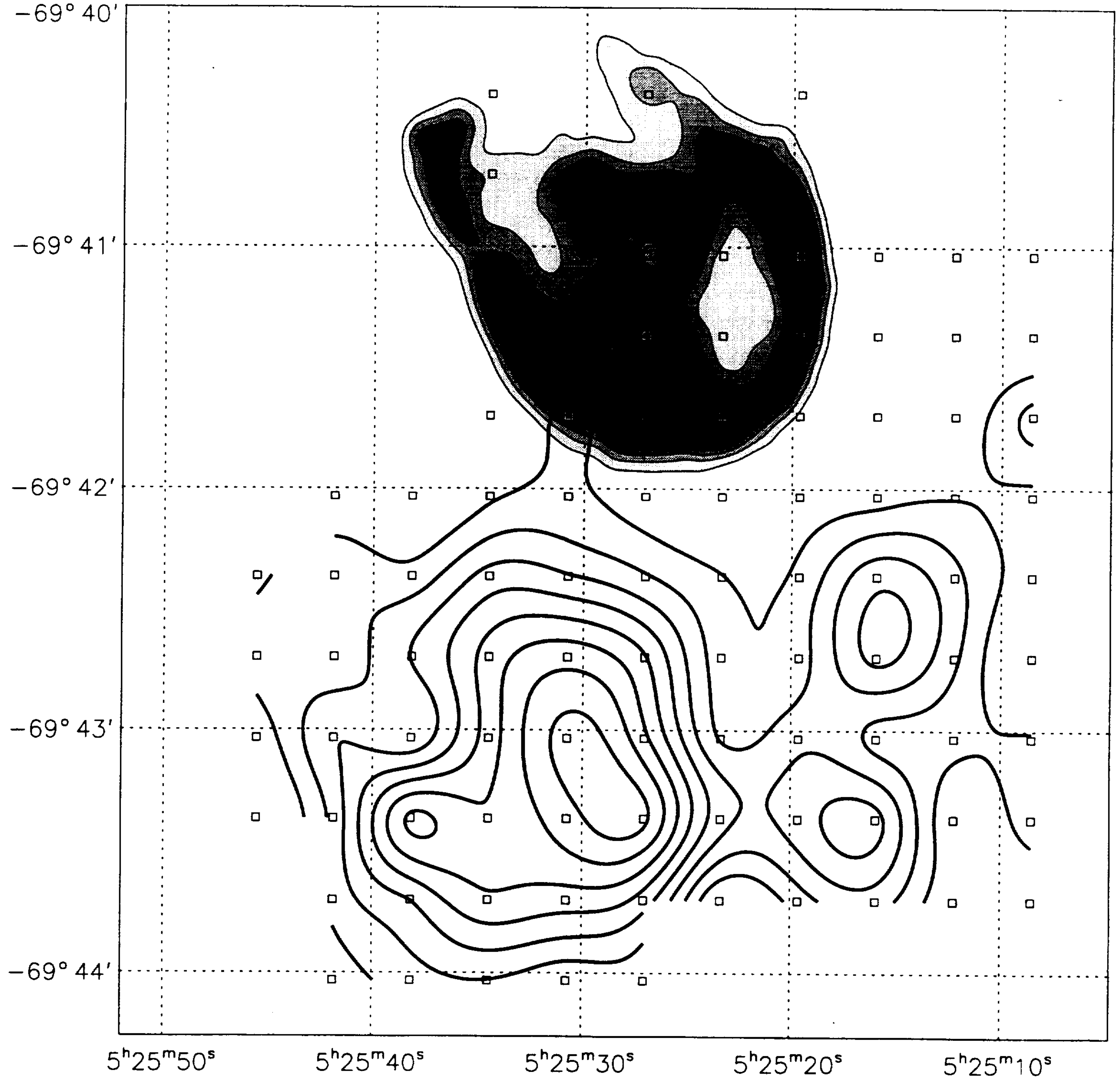
−69° 40′
−69° 41′
−69° 42′
−69° 43′
−69° 44′
5h25m50s
5h25m40s
5h25m30s
5h25m20s
5h25m10s

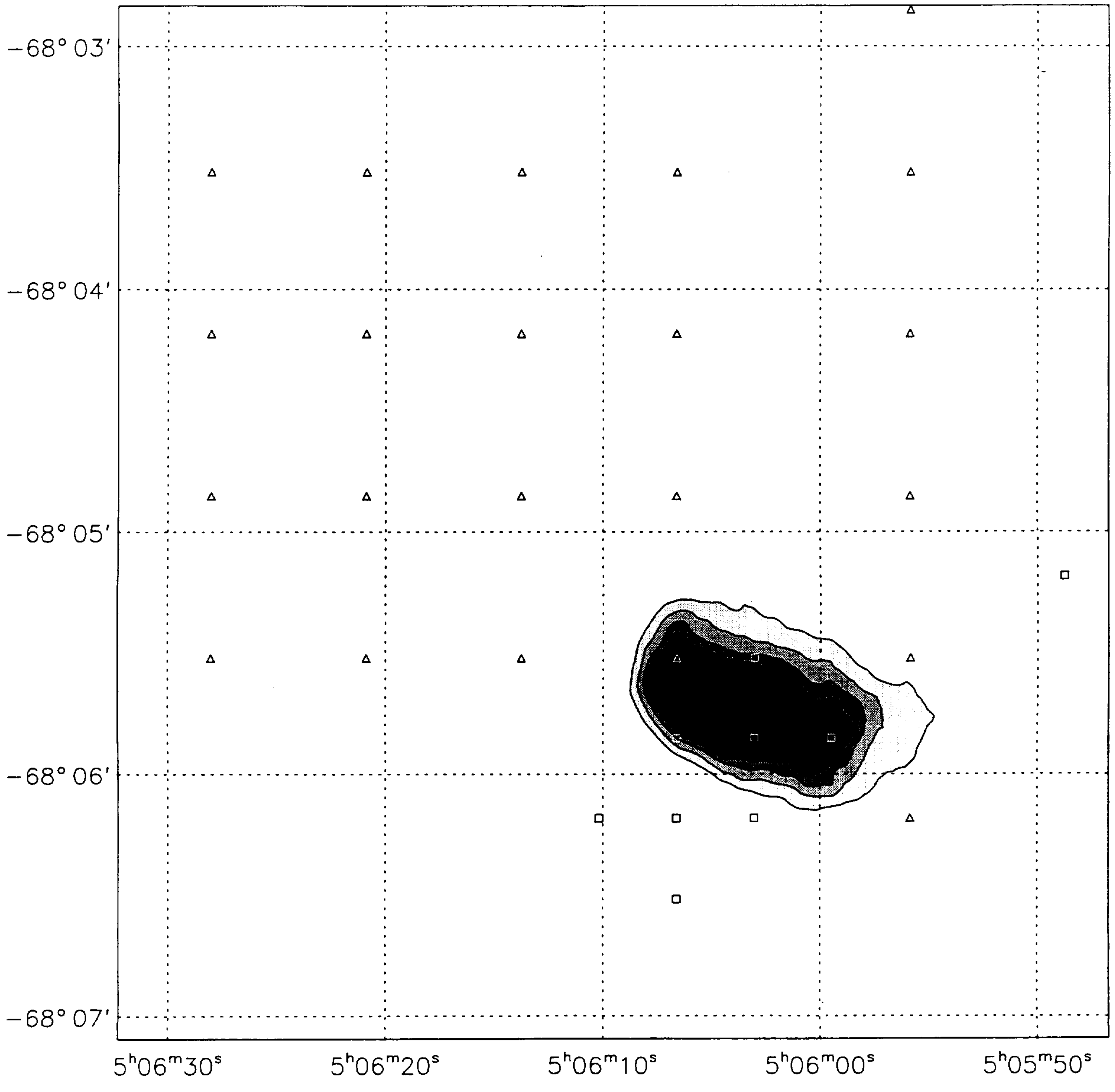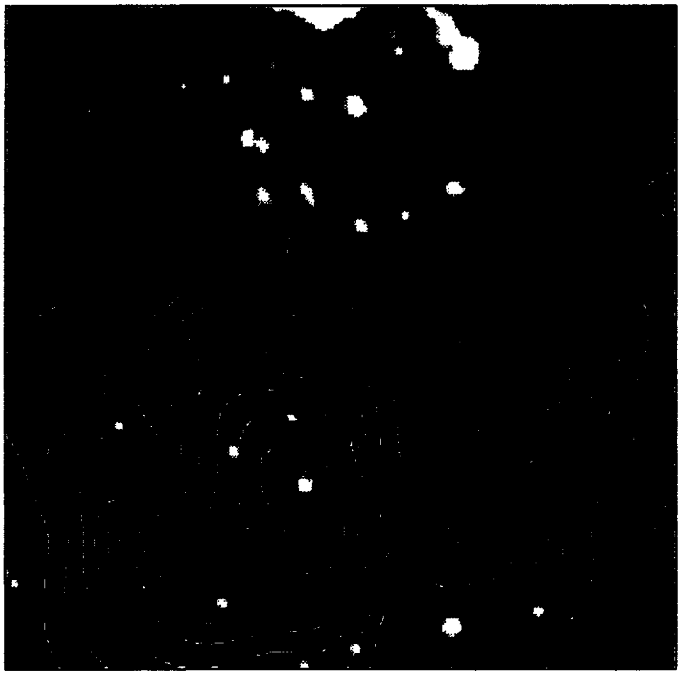
−68° 03′
−68° 04′
−68° 05′
−68° 06′
−68° 07′
5h06m30s
5h06m20s
5h06m10s
5h06m00s
5h05m50s